6-28-2013

Microspheres for Liver Radiomicrospheres Therapy and Planning

Alejandro Amor-Coarasa
Florida International University, acoarasa@fiu.edu

FLORIDA INTERNATIONAL UNIVERSITY

Miami, Florida

MICROSPHERES FOR LIVER RADIOMICROSPHERES THERAPY AND PLANNING

A dissertation submitted in partial fulfillment of the

requirements for the degree of

DOCTOR OF PHILOSOPHY

in

BIOMEDICAL ENGINEERING

by

Alejandro Amor Coarasa

2013

To: Dean Amir Mirmiran
College of Engineering and Computing

This dissertation, written by Alejandro Amor Coarasa, and entitled Microspheres for Liver Radiomicrospheres Therapy and Planning, having been approved in respect to style and intellectual content, is referred to you for judgment.

We have read this dissertation and recommend that it be approved.

_____
Seza A. Gulec

_____
Yen-Chih Huang

_____
Wei-Chiang Lin

_____
Joongho Moon

_____
Anthony J. McGoron, Major Professor

Date of Defense: June 28, 2013

The dissertation of Alejandro Amor Coarasa is approved.

_____
Dean Amir Mirmiran
College of Engineering and Computing

_____
Dean Lakshmi N. Reddi
University Graduate School

Florida International University, 2013

DEDICATION

To my grandfather, my guide in life, who taught me early that a kick in the a** is also a push forward and that I should never give up.

To Prof. José Griffith Martínez, the first Cuban Radiochemist, my friend and mentor, who passed away alone and forgotten on December 8, 2008.

To Prof. Simón Rodríguez Calvo, the best teacher I ever had.

ACKNOWLEDGMENTS

I want to express my infinite gratitude to my advisor Dr. Anthony McGoron. His door was always opened and no matter how hard the words were, he would lay then down like lead bricks on my chest and that's the kind of honesty I really appreciate. To Dr. Seza Gulec, mentor, friend and older brother, our reasoning alignment was sometimes disturbing and creepy. We could just look at each other without needing words to communicate. Both (Dr. McGoron and Dr. Gulec) embraced my abilities and trusted my knowledge when I first came to this country, they will be therefore somehow responsible for all my future achievements and for that I am grateful. To Dr. James Byrne, a walking encyclopedia, he was always willing to help. I really enjoyed all of our conversations no matter what the topic was. To Manuel Sztejnberg for all the help provided.

I am eternally grateful To Andrew Milera and Deny Carvajal, my friends, science loving volunteers, that sometimes worked 24 hours straight without complaint. Without them the bulk of this dissertation would not have been possible. Also want to recognize the help received from the entire lab group: Romila, Alicia, Supriya, Tinjun, Vinay, Abi and others. My dissertation committee members: Dr. Yen-Chih Huang for providing one of the polymers and valuable advice; Dr. Wei-Chiang Lin for his help in all the needed paperwork and dealing with the graduate school; and Dr. Joong-Ho Moon for his chemistry advise and willingness to help. To the people in the Dean's office, Amy, Bertha, Laura etc.

Last but not least, I want to thank my family. To my father and mother, for showing me a path of knowledge embracement, supporting me all the time. Thanks to my friends for all the help and support. Thanks also to my grandmother for all the praying and the good thoughts. And last to Miriel, my girlfriend angel, who was there handling my changing mood and not complaining, who supported my decisions, suffered my setbacks and enjoyed my achievements along the way.

ABSTRACT OF THE DISSERTATION

MICROSPHERES FOR LIVER RADIOMICROSPHERE THERAPY AND PLANNING

by

Alejandro Amor Coarasa

Florida International University, 2013

Miami, Florida

Professor Anthony J. McGoron, Major Professor

Liver cancer accounts for nearly 10% of all cancers in the US. Intrahepatic Arterial Radiomicrosphere Therapy (RMT), also known as Selective Internal Radiation Treatment (SIRT), is one of the evolving treatment modalities. Successful patient clinical outcomes require suitable treatment planning followed by delivery of the microspheres for therapy. The production and *in vitro* evaluation of various polymers (PGCD, CHS and CHSg) microspheres for a RMT and RMT planning are described. Microparticles with a 30±10 μm size distribution were prepared by emulsion method. The *in vitro* half-life of the particles was determined in PBS buffer and porcine plasma and their potential application (treatment or treatment planning) established. Further, the fast degrading microspheres (≤ 48 hours *in vitro* half-life) were labeled with ^{68}Ga and/or ^{99m}Tc as they are suitable for the imaging component of treatment planning, which is the primary emphasis of this dissertation. Labeling kinetics demonstrated that ^{68}Ga-PGCD, ^{68}Ga-CHSg and ^{68}Ga-NOTA-CHSg can be labeled with more than 95% yield in 15 minutes; ^{99m}Tc-PGCD and ^{99m}Tc-CHSg can also be labeled with high yield within 15-30 minutes. *In vitro* stability after four hours was more than 90% in saline and PBS buffer for all of them. Experiments in reconstituted hemoglobin lysate were also performed. Two successful imaging (RMT planning) agents were found: ^{99m}Tc-CHSg and ^{68}Ga-NOTA-CHSg. For the ^{99m}Tc-PGCD a successful perfusion image was obtained after 10 minutes, however the *in vivo* degradation was very fast (<30 min half-life),

releasing the ^{99m}Tc from the lungs. Slow degrading CHS microparticles (> 21 days half-life) were modified with p-SCN-b-DOTA and labeled with ^{90}Y for production of ^{90}Y-DOTA-CHS. Radiochemical purity was evaluated *in vitro* and *in vivo* showing more than 90% stability after 72 and 24 hours respectively. All agents were compared to their respective gold standards (^{99m}Tc-MAA for ^{68}Ga-NOTA-CHSg and ^{99m}Tc-CHSg; ^{90}Y-SirTEX for ^{90}Y-DOTA-CHS) showing superior *in vivo* stability. RMT and RMT planning agents (Therapy, PET and SPECT imaging) were designed and successfully evaluated *in vitro* and *in vivo*.

TABLE OF CONTENTS

LIST OF TABLES

LIST OF FIGURES

ABBREVIATIONS AND ACRONYMS

CHS	Chitosan
CHSg	Chitosan Glycol
CT	Computes Tomography
DC	Decay Corrected
DC-ID/g	Decay Corrected Injected Dose per Gram.
DOTA	1,4,7,10-tetraazacyclododecane-1,4,7,10-tetraacetic acid
HAM	Human Albumin Microspheres
ID	Injected Dose
IV	Intravenous
MAA	Macroaggregated Albumin
MCNP	Monte Carlo radiation transport code
MCNPX	Monte Carlo N-Particle eXtended
nMR	Nuclear Magnetic Resonance
NOTA	1,4,7-triazacyclononane-1,4,7-triacetic acid
PET	Positron Emission Tomography
PGCD	poly(glycerol-citric-dodecanediooate)
p-SCN-Bn-DOTA	2-(4-isothiocyanatobenzyl)-1,4,7,10-tetraazacyclododecane-1,4,7,10-tetraacetic acid
p-SCN-Bn-NOTA	S-2-(4-Isothiocyanatobenzyl)-1,4,7-triazacyclononane-1,4,7-triacetic acid
RMBLR	The red marrow to blood activity concentration ratio
RMT	Radiomicrosphere Therapy
ROBY	Rat Whole Body Phantom
SIRT	Selective Internal Radiation Treatment
SPECT	Single Photon Emission Computed Tomography

CHAPTER 1 INTRODUCTION

Radiomicrosphere Therapy (RMT), via hepatic arterial administration is a treatment for patients with primary and metastatic liver cancer (figure 1). Because the primary blood supply to liver tumors is from the hepatic artery while the majority of the blood supply to the normal liver is from the portal vein, this procedure offers selectivity to tumor.

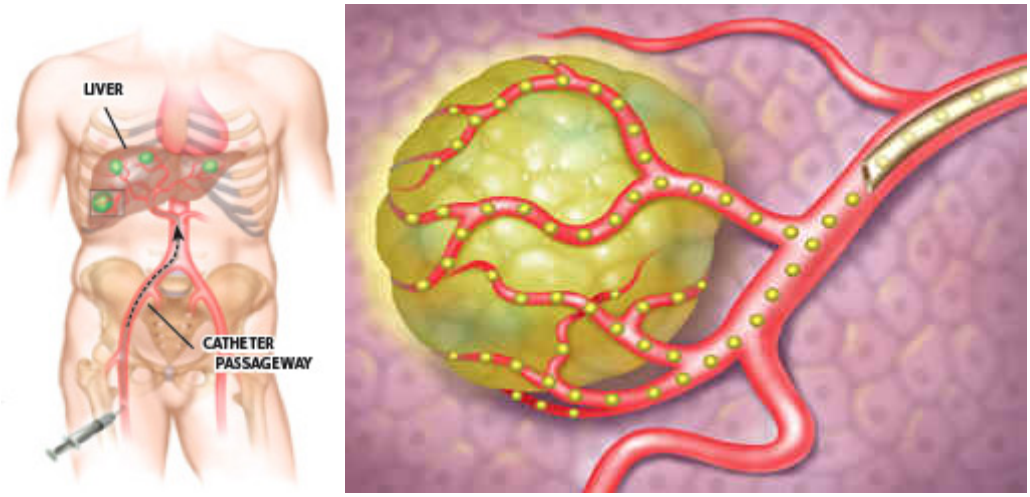

Fig 1. Liver and Tumor Vasculature (1)

The micro-vascular density of liver tumors is 3-200 times greater than the surrounding liver parenchyma, further improving the selectivity of the therapy to the tumor (2). In this treatment, 30 μm diameter spheres labeled with the radioactive isotope ^{90}Y (yttrium-90, a high-energy beta particle–emitting radioisotope) become lodged in the arterioles within the tumor and destroy the tumor while leaving the normal liver tissue mostly unharmed. A randomized trial in 2001 with 74 patients showed that combining SirSpheres (one of the available products in the market) with chemotherapy had a 44 % response versus a 17.6 % with chemotherapy alone (3).

The ^{90}Y disintegration within glass microspheres occurs without any chemical release because the radioisotope is completely trapped inside the microsphere and is part of the crystalline structure.

In other words, there is no surface degradation of the particles. Resin microspheres are basically ionic exchange matrices that bind the yttrium by means of strong non-specific ionic interactions. The earliest device of this kind (resin microspheres) was shown to release the isotope once in contact with blood (4) and also showed some other complications (5; 6). Although there is no report of leaching of ^{90}Y for the commercial SirSpheres product, such behavior is a possibility, even if not significant, because of the ionic nature of the radioisotope attachment to the particles. SirSpheres are prescribed to be injected using pure water instead of saline solution to avoid any ionic exchange before injection. The main advantage of the resin spheres is that the radiation dose and concentration of spheres can be manipulated in situ to provide a patient specific treatment. In contrast the glass spheres need to be allowed to decay in order to achieve the proper dose.

The possibility of injury to gastrointestinal tract and lungs are complications that can be evaluated (predicted), to a certain extent, using a hepatic arterial flow imaging study with ^{99m}Tc labeled macroaggregated albumin (^{99m}Tc-MAA) prior to treatment (6). For treatment planning ^{99m}Tc-MAA is infused into the proper hepatic artery and a perfusion scintigraphy is performed. However, the significant differences in size, shape, and other properties between the MAA and ^{90}Y microspheres (Fig 2) complicates the treatment planning because the MAA particles cannot be expected to distribute exactly like the ^{90}Y microspheres.

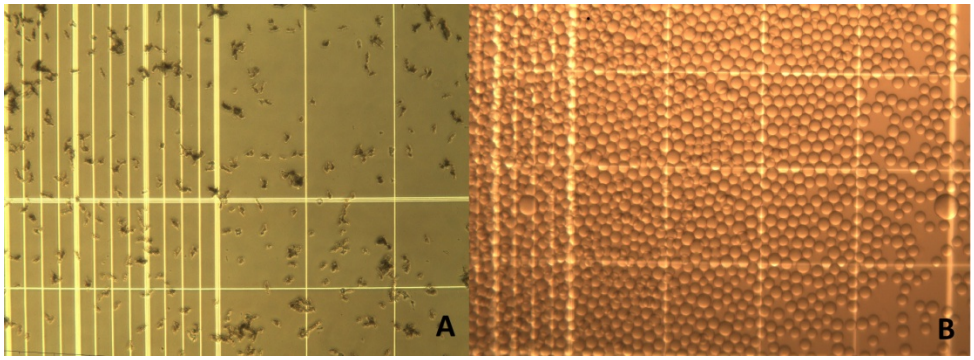

Fig 2. Comparison of A: MAA microparticles and B: Resin microspheres

The present dissertation addresses the development and use of a new biodegradable sphere for accurate RMT planning/treatment. Several polymers: Chitosan, Chitosan Glycol and a new synthetic biodegradable elastomer Poly(glycerol-citric-dodecanedioate)) are evaluated employing different emulsion techniques to produce approximately 30 μm size biodegradable microspheres that match the size and shape of the ^{90}Y microspheres commercial products. The obtained particles were submitted to *in vitro* degradation studies and characterized with respect to size, shape, and size distribution.

Different radiolabeling techniques were evaluated for labeling yields, radiochemical purity and stability of the final product. The *in vivo* evaluation of the particles was performed in Sprague Dawley rats. The animals were imaged using full body autoradiography/X-Ray techniques and later euthanized at different times. Several organ samples were collected for measuring of radioactive content in a Cobra 5000 NaI(Tl) well detector [Perkin Elmer, USA]. Numerical dosimetry calculations were done using MCNPx to evaluate the radiation field and dose distributions and to assure radioprotection standards were met.

1.1 Objective and Specific Aims and hypotheses

The overall objective is **to design and evaluate a complete RMT package with fast (12 to 48 hours, planning) and slow (>21 days, therapy) degradation half-life 30 ± 10 μm biodegradable microspheres to be labeled with ^{68}Ga or ^{99m}Tc for RMT planning and with ^{90}Y for RMT (respectively) with high yield and >90% radiochemical purity**.

This objective was accomplished by addressing the following specific aims:

1.1.1 Specific Aim #1

Develop and implement appropriate emulsion and purification methods for the creation of 30±10 μm polymer particles.

The outcome of this aim provided the necessary raw materials for the subsequent experiments.

1.1.2 Specific Aim #2

Perform radiolabeling of the particles with more than 90% ^{68}Ga, ^{99m}Tc or ^{90}Y labeling yield and *in vitro* radiochemical purity for the studied periods.

The outcome of this aim was to demonstrate that the created particles were capable of trapping and retaining the radioisotopes. This aim includes the surface modification of the particle with specific chelating agents to improve *in vitro* and ultimately *in vivo* stability.

1.1.3 Specific Aim #3

Perform *in vitro* stability studies of the particles in saline, PBS buffer and animal plasma to determine their degradation half-lives.

The outcome of this aim was to assess the possibility of using different particles as a RMT planning (as a prospective replacement for MAA) with a degradation half-life of 12 to 48 hours and treatment agent as a potential replacement for resin or glass microspheres with a degradation half-life of more than 21 days.

1.1.4 Specific Aim #4

Conduct *in vivo* lung perfusion studies in Sprague Dawley rats to evaluate the stability and bio-distribution of the particles and the radioactive labels.

The outcome of this aim was to assess the feasibility of translating our microsphere design to a clinical setting for RMT.

The following hypotheses will be tested in the specific aims of research.

#1 Particles measuring 30±10 μm diameter can be created from biocompatible polymers using emulsion and purification methods.

#2 The particles can be radiolabeled with **^{68}Ga or ^{99m}Tc** for RMT planning and ^{90}Y for RMT with ≥ 90% *in vitro* radiochemical purity.

#3 The radiolabeled particles can have 12-48 hours *in vitro* half-life for RMT planning and >21 days *in vitro* half-life for RMT.

#4 The radiolabeled particles can have > 90% *in vivo* stability for proper lung perfusion imaging studies.

CHAPTER 2 BACKGROUND

2.1 Nuclear Medical Imaging

There are five basic modalities of nuclear medical imaging: Planar Scintigraphy, SPECT, PET, nMR and X-Ray (CT). X-Ray emission in medical imaging is almost entirely due to electronic excitation, however it is considered "nuclear imaging" because of the high energy of the emitted quantum. These five basic modalities can be separated into two subcategories: Functional Medical Imaging (Planar Scintigraphy, SPECT and PET) and Anatomical Medical Imaging (CT and nMR). Though these subcategories are not set in stone since contrast CT and functional nMR are also performed. The current review will concentrate on the functional imaging subcategory and their combination with the nMR and CT considered for their importance attenuation correction and anatomical registration purposes.

2.1.1 Planar Scintigraphy. The Anger Camera.

Since George de Hevesy (considered the father of nuclear medicine) devised the term radiotracer in the 1920s a new age started. The main advantage of radiotracers was that since they could be injected in very small amounts, the system could easily be studied without being disturbed. The first nuclear imaging camera, called Scintigraphy Camera, was designed in 1957 by Hal Anger (also called Anger Camera), still widely used today (7). It consist of a single NaI(Tl) (sodium iodide, thallium activated) crystal, coupled to several photomultipliers for detection and amplification. The thickness of the crystal is between 6-25 mm and it is optimized at 10 mm for detection of 120-200 keV gamma energy. Thinner crystals provide better spatial resolution but decreased sensitivity (8). A collimator is also used in front of the scintillation crystal to allow only perpendicular (or near perpendicular) photons to interact with the crystal (Fig 3).

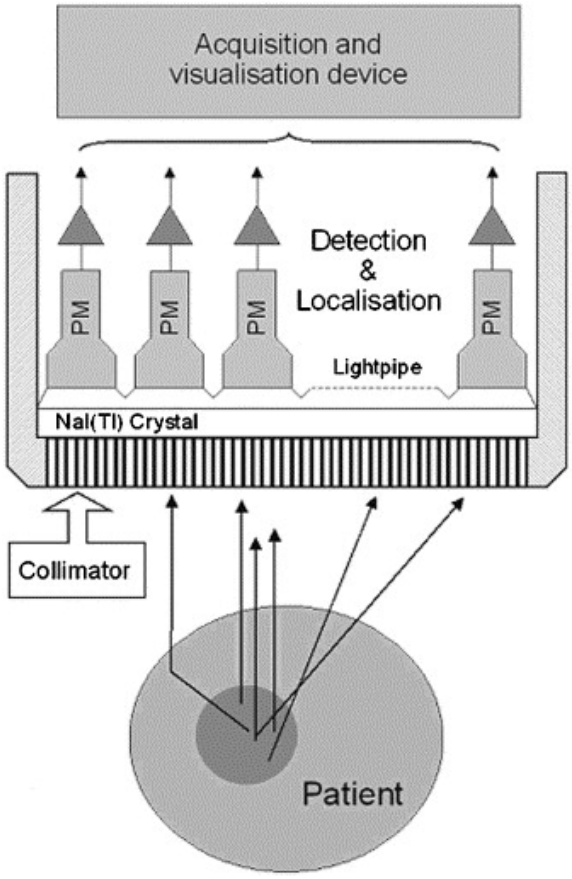

Fig 3 Basic components of the Anger Camera (7).

The interaction of the gamma quantum with the crystal produces excitation with subsequent emission of light. The light interacts with a photocathode emitting electrons, later amplified in the photomultipliers. Since only perpendicular gamma was allowed to enter the crystal, the location of the amplification is aligned with the location of emission in the patient. With all the independent intensities and coordinates, a planar image is formed.

2.1.2 Single Photon Emission Tomography

Single photon emission tomography is just an application of the anger camera to obtain tri-dimensional (3D) images of the radioisotope distribution. Most Clinical SPECT systems are

based on a dual planar camera system that rotates on the patient axis to obtain different projections for image reconstruction.

Fig 4 Some commercially available SPECT/CT systems: A: Philips Medical Systems BrightView XCT, B: GE Healthcare Infinia-Hawkeye and C: Siemens Healthcare Systems Symbia (9).

Attenuation effects are more severe in body imaging than in brain imaging since the photon carries a shorter path in the latter. Additionally, attenuation is not uniform throughout the patient, so attenuation correction becomes a major limitation of SPECT, hence quantification of the tracer is very difficult. Several approaches have been taken to correct attenuation with some level of success. A ^{153}Gd source is sometimes used to generate transmission scans while obtaining the image projections (10), combined CT scans (Fig 4) are also used for correction (11). All these methods remain under evaluation. Nevertheless SPECT and SPECT/CT images have excellent medical diagnostic value (e.g. Fig 5).

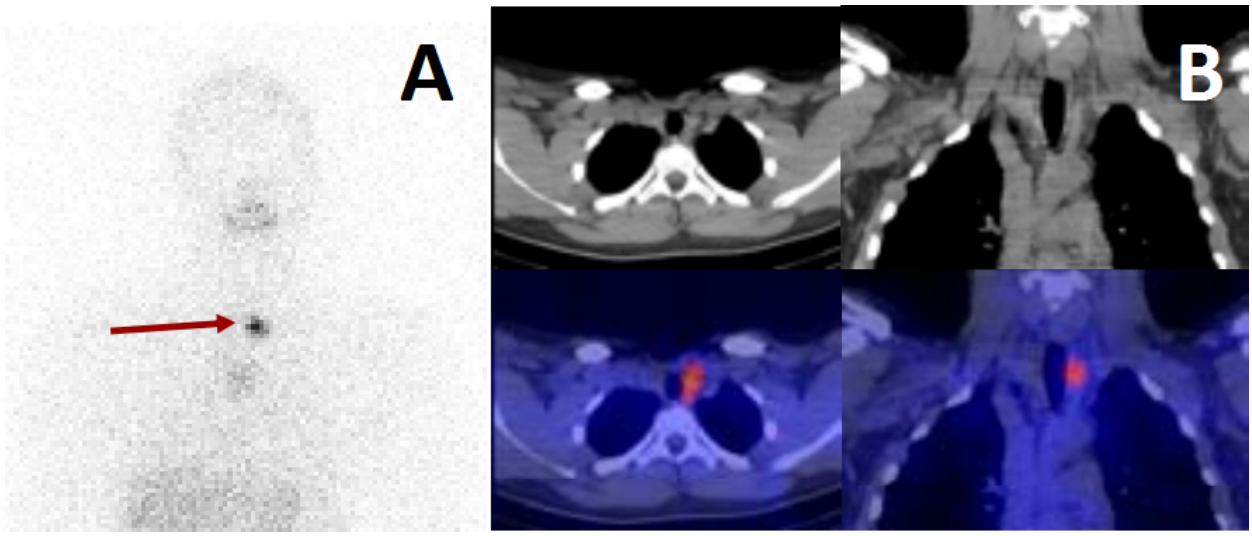

Fig 5 ^{131}I scan of thyroid cancer (red arrow) A: Planar Scintigraphy and B: SPECT/CT (12)

2.1.3 Positron Emission Tomography

Positron emission tomography is a medical imaging technique that is not based on positron emission detection (as its name indicated) but rather on the detection of the result of the positron annihilation (Fig 6).

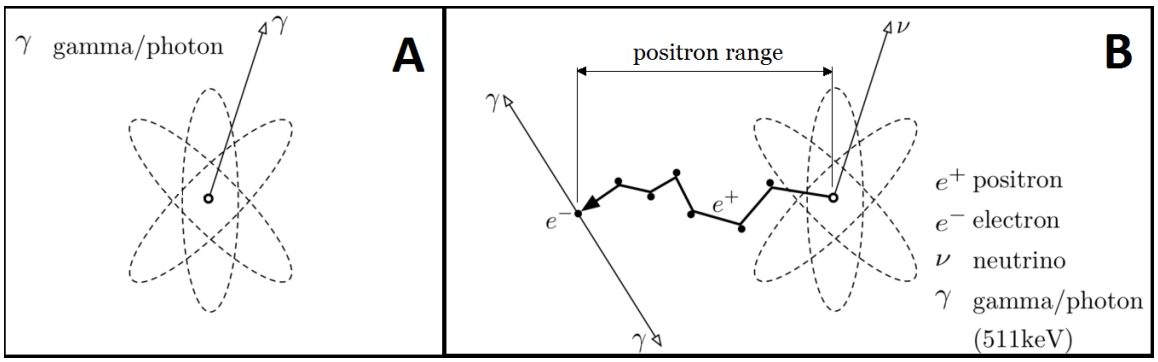

Fig 6 Radioactive disintegration for A: single photon emission and B: positron emission.

As can be seen in Fig 6, the positron travels some distance before annihilation, and this is directly proportional to the maximum energy of the beta disintegration. The linear distance traveled is referred to as the positron range (Fig 6 B). The annihilation produces two perpendicular photons

(180±0.25º) that are identified by opposing detectors (arranged circularly) in coincidence mode (only two detection events happening within 1 nanosecond are registered). The line of detection of the photons is registered and intercepted with other detected paths to conform the image (Fig 7).

Compared to those used in SPECT, PET detectors need to be thicker. Annihilation emission has an energy of 511 keV (compare to the regular 100-200 keV in SPECT) hence the detector needs greater stopping power. Crystals normally used in PET are made of Bismuth Germanium Oxide (BGO, also Bismuth Germanate, $Bi_4Ge_3O_{12}$) and Cerium-doped lutetium oxyorthosilicate (LSO). These have a relatively good light output and a short time constant (80% more efficient than NaI(Tl) for the 511 keV energy). The electronics of PET cameras are rather complicated and further detail can be found in several publications (13; 14).

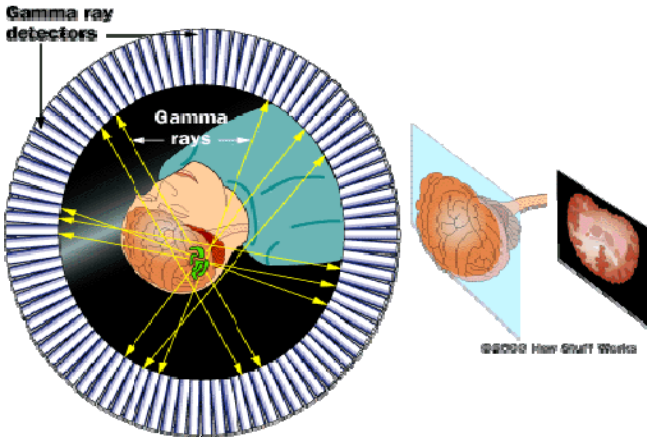

Fig 7 Positron Emission Tomography image and registration (15)

Resolution of PET cameras has increased significantly over time. Starting at 10 mm spatial resolution in the 1980's to the current 4 mm (1.2 mm in micro-PET) (16). The theoretical spatial resolution of PET is limited by the positron range while spatial resolution is limited primarily by

the collimator design. Thus, the election of proper radionuclides (based on its physical characteristics) to be used in the development of future drugs becomes important (Table 1).

Table 1 Physical Properties of Positron Emitting Radionuclides Most Commonly Used. Isotopes with particular importance in PET are bolded. (16)

Radionuclide	**T ½**	**% β+ Emission**	**Max β E (MeV)**	**Max Range Water (mm)**	**Ave Range Water (mm)**	**Produced**
^{11}C	20.4 min	99	0.96	3.9	0.4	Cyclotron
^{13}N	9.96 min	100	1.2	5.1	0.6	Cyclotron
^{15}O	2.05 min	100	1.7	8.0	0.9	Cyclotron
^{18}F	**1.83 h**	**97**	**0.64**	**2.3**	**0.2**	**Cyclotron**
^{62}Cu	9.74 min	98	2.9	15	1.6	^{62}Zn/^{62}Cu
^{64}Cu	12.7 h	19	0.58	2.0	0.2	Cyclotron
^{66}Ga	9.49 h	56	3.8	20	3.3	Cyclotron
^{68}Ga	**1.14 h**	**88**	**1.9**	**9.0**	**1.2**	**^{68}Ge/^{68}Ga**
^{76}Br	16.1 h	54	3.7	19	3.2	Cyclotron
^{82}Rb	1.3 min	95	3.4	18	2.6	^{82}Sr/^{82}Rb
^{86}Y	14.7 h	32	1.4	6.0	0.7	Cyclotron
^{124}I	4.18 d	22	1.5	7.0	0.8	Cyclotron

2.2 Radioisotope Production.

There are two basic nuclear installations to produce radioisotopes: nuclear reactors (to include neutron sources) and particle accelerators. With different designs and working principles, both nuclear installations are capable of producing radioisotopes for nuclear medicine applications.

2.2.1 Nuclear Reactor Produced Radioisotopes.

Nuclear reactors were most commonly used in the past 50 years of nuclear medicine history. Whether the radionuclides are produced by fission of heavier nuclides or by neutron irradiation they both yield radioisotopes with excess neutrons, which indistinctively decay by electron emission (β^-, excluding some rare exceptions). This production was aligned with the needs of nuclear medicine since β^- emitting nuclides are still used for therapy and the gamma emitting daughters for SPECT imaging (e. g. $^{99}Mo/^{99m}Tc$) (Fig 8).

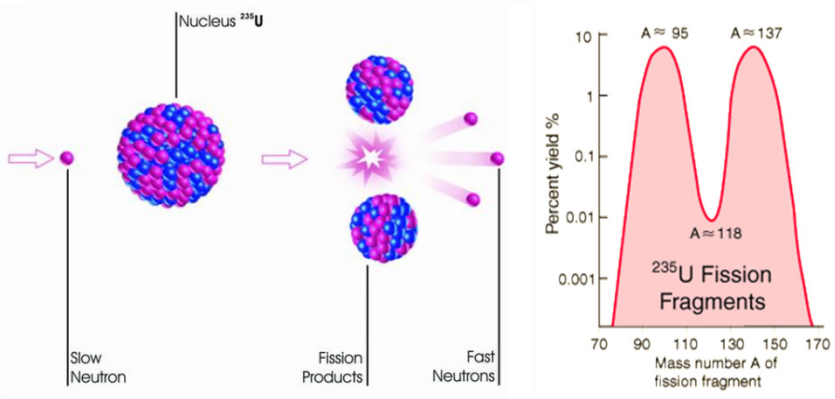

Fig 8 Fission of ^{235}U (17) with neutron generation and yield of fragments (18).

Fission is not a desired production method, since a full distribution of both long and short lived isotopes is obtained. Radiochemical separation of the products is a lengthy process not yielding enough purity for medical applications. Neutron irradiation of defined, pure targets is a better approach to production, however high neutron flux is needed to yield sufficient radioisotope amounts. Neutron activation of cold targets is explained by the following equation:

$$A = N\sigma\emptyset\left(1 - e^{-\lambda t_{irradiation}}\right) \quad (2.2.1.1)$$

Where N is the number of target atoms present in the initial material; Φ is the neutron flux; λ is the decay constant of the product and σ is the cross section. The cross section is given in barns (1

barn=10^{-24} cm^2), which intuitively represents the cross sectional area of the nuclei in question. However it is much more complex, including the efficiency of neutron capture, reaction yield, and incident neutron energy among others. Regardless of the complexity of the cross section concept, a bigger value of Φ aids the radionuclide production. Some isotopic productions benefit from thermal (low energy) neutrons and others from higher energy (Table 2).

Table 2 Neutron Energy Ranges needed to produce several medical isotopes (19).

Neutron Energy	Isotope Production
Thermal Epithermal (0.01 eV – 10 keV)	^{75}Se, ^{89}Sr, ^{90}Y, ^{103}Pd, ^{125}I, ^{131}I, ^{127}Xe, ^{131}Cs, ^{153}Gd, ^{153}Sm, ^{165}Dy, ^{166}Ho, ^{177}Lu, ^{186}Re, ^{188}W, ^{192}Ir, ^{198}Au, ^{223}Ra, ^{225}Ac
Fast (10 keV - 1.0 MeV)	^{99}Mo, ^{117m}Sn
High Energy (1.0 MeV – 10 MeV)	^{32}P, ^{33}P, ^{57}Co, ^{62}Cu, ^{64}Cu, ^{67}Cu, ^{89}Sr
14 MeV	^{99}Mo, ^{225}Ac

The recent shortages in the production of radioisotopes have evidenced a crude reality: Reactors are getting old, production yields are decreasing and no new facilities are being built (20). Alternatives are being used, research reactors are included in production, new low enriched uranium neutron sources are being used and finally new production reactions (especially of ^{99}Mo) are being studies in particle accelerators (21).

2.2.2 Cyclotron Produced Radioisotopes

With the advent of the PET camera, positron emitters to be used in medical imaging were needed (^{18}F, ^{11}C, ^{13}N, ^{15}O, etc.). These radioisotopes are, in contrast to β^- emitters, neutron deficient isotopes. Thus they cannot be produced in nuclear reactors or with neutron sources. The last statement does not preclude the production of radioisotopes with excess neutrons in cyclotrons, since it only depends on the initial target material used and the energy of the incident proton

beam. In contrast with nuclear reactors that cannot be shut down once built and keep producing high level nuclear waste until the fuel is spent, cyclotron are started and stopped at will (Fig 9).

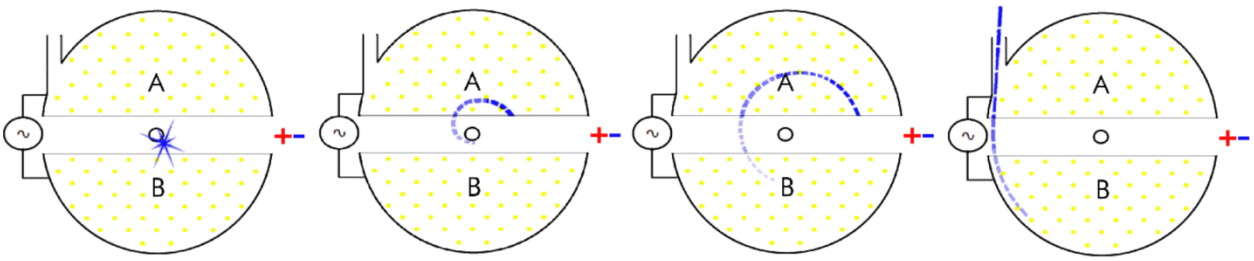

Fig 9 Cyclotron working principle; A and B: Dees; yellow dots: perpendicular magnetic field (22).

With a constant perpendicular magnetic field (yellow dots in Fig 9), a charged particle is generated in the center (normally a proton, an ionized H^+ atom). Dees charge is change sequentially to accelerate the proton and increase its energy. The particle is finally release through a port to irradiate the targets. The maximum kinetic energy obtained is:

$$E_{max} = \frac{q^2 \cdot B^2 \cdot r^2}{2 \cdot m} \qquad (2.2.2.1)$$

Where q is the charge of the particle, B is the incident magnetic field and r is the maximum radius before release (radius of the cyclotron). For every day clinical use (especially for production of ^{18}F) high energy cyclotrons are not needed. Since the energy is proportional to the square of the cyclotron radius, smaller cyclotrons can be built. For these reasons and to reduce initial investment and running costs, small cyclotrons are currently produced and commercialized.

Fig 10 Siemens Eclipse™ series cyclotron produces high quantities of ^{18}F, ^{11}C, ^{13}N, ^{64}Cu and ^{15}O (Width: 95 in. (240 cm), Depth: 73 in. (184 cm), Height: 90 in. (230 cm)) (23)

Higher energies (translated into bigger machines and costs) are needed for the production of other positron emitters and positron emitter parent for the production of radioisotopic generators (Table 3).

Table 3 Positronic radionuclides production vs. incident proton energy

Proton Energy (MeV)	**Radionuclides Produced (usable quantities)**
0-10	^{18}F, ^{15}O
11-16	^{11}C, ^{18}F, ^{13}N, ^{15}O, ^{22}Na, ^{48}V
17-30	^{124}I, ^{123}I, ^{67}Ga, ^{111}In, ^{11}C, ^{18}F, ^{13}N, ^{15}O, ^{22}Na, ^{48}V, ^{201}Tl
30 +	^{124}I, ^{123}I, ^{67}Ga, ^{111}In, ^{11}C, ^{18}F, ^{13}N, ^{15}O, ^{82}Sr, ^{68}Ge, ^{22}Na, ^{48}V

2.2.3 Radioisotopic Generators

A radioisotopic generator is a radiochemical separation system in which quasi stable decay equilibrium is reached between a parent and a daughter nuclide (half-life ($t_{1/2}$) of parent has to be

at least a 10 fold greater that the half-life of the daughter). The system should allow the effective separation of the daughter nuclide from its parent nuclide with high radiochemical and radionuclidical purity. It is goverened by the exponential disintegration and accumulation laws formulated by Rutherford and Soddy in 1902 (24).

2.2.3.1 Nuclear Physics of Radioisotopic Generators

Given the disintegration scheme:

$$X_1 \overset{\lambda_1}{\rightarrow} X_2 \overset{\lambda_2}{\rightarrow} X_{3(stable)}$$

The number of daughter nuclides (N_2) formed by disintegration of the parent nuclide (N_1) is given by the following equation:

$$N_2 = \frac{\lambda_1}{\lambda_2 - \lambda_1} N_1 \left(e^{-\lambda_1 t} - e^{-\lambda_2 t}\right) + N_2 e^{-\lambda_2 t} \qquad (1.1)$$

Substituting $A_i = N_i \lambda_i$ the Activity is expressed as:

$$A_2 = \frac{\lambda_2}{\lambda_2 - \lambda_1} A_1 \left(e^{-\lambda_1 t} - e^{-\lambda_2 t}\right) + A_2 e^{-\lambda_2 t} \qquad (1.2)$$

where $\lambda_i = \frac{\ln 2}{t_{1/2(i)}}$ is the disintegration constant of the particular radioisotope (i).

The first part of the equation represents the activity of the daughter nuclide while being formed by decay of the parent. The second part corresponds to the decay of the daughter nuclides existing at initial time (t=0). After complete extraction (elution) of the daughter nuclide, the second part nullifies, thus the first part describes the daughter nuclide accumulation in the system. To obtain the maximum accumulation time equation (1.2) is derived and equated to cero:

$$t_{\text{maximum } accumulation} = \frac{\ln \frac{\lambda_2}{\lambda_1}}{\lambda_2 - \lambda_1} \quad (1.3)$$

The equation (1.3) is used to calculate the optimum elution time for the system.

As stated before the condition $R_t = \frac{t_{\frac{1}{2}parent}}{t_{\frac{1}{2}daughter}} \geq 10$ is needed for an effective generator. Taking R_t into consideration three different conditions can be defined: $R_t < 10\ no\ equilibrium$,

$10 < R_t < 100$ *transient equilibrium* and $R_t > 100$ *Secular Equilibrium*. In transient equilibrium the process is governed by equation (1.2) and no approximation is possible. Daughter nuclide is initially accumulated and then decays with the half-life of the parent nuclide (Fig 11 A). However in secular equilibrium the parent nuclide can be considered almost stable compared to the decay of the daughter so only apparent accumulation is observed (Fig 11 B).

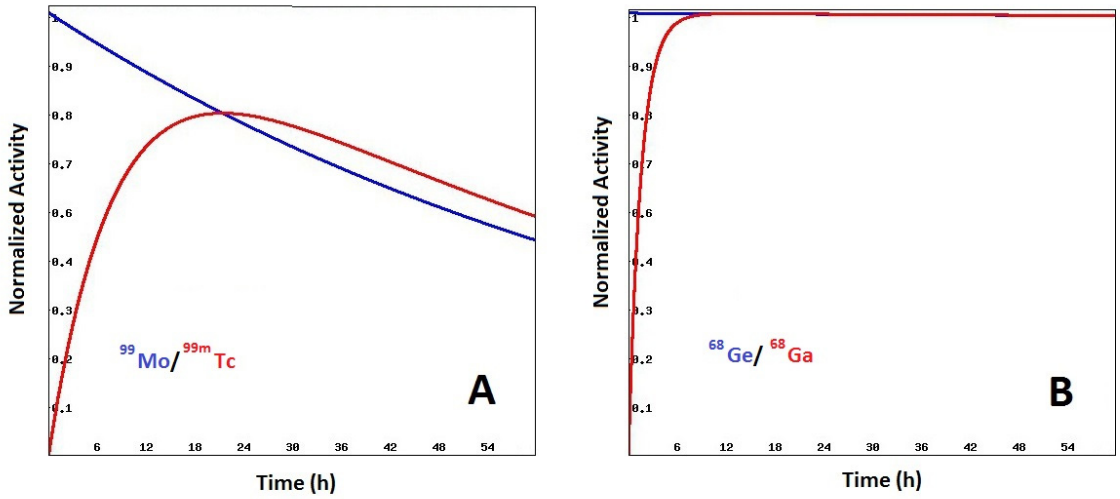

Fig 11 Decay and accumulation representation of A: the ^{99}Mo/^{99m}Tc generator and B: the ^{68}Ge/^{68}Ga generator.

The useful life of a radioisotopic generator is given mainly by the half-life of the parent nuclide. However, other factors like the chemical, radiochemical and radionuclidical purity of the elution, the elution yield and radiolytic damage to the supporting material also affect the effective life of a system. Based only on nuclear properties, some examples of parent/daughter couples for generator production are shown on Table 4.

Table 4 Some Parent/Daughter couples with transient and secular equilibrium

Pair	Parent $t_{½}$	Daughter $t_{½}$
^{28}Mg/^{28}Al	20.9 h	2.24 min
^{42}Ar/^{42}K	32.9 y	12.36 h
^{47}Ca/^{47}Sc	4.54 d	3.35 d
^{90}Sr/^{90}Y	28.8 y	64 h
^{99}Mo/^{99m}Tc	66.02 h	6.02 h
^{113}Sn/^{113m}In	115.1 d	99.5 min
^{115}Cd/^{115m}In	53.5 h	4.5 h
^{125}Sb/^{125m}Te	2.77 y	58 d
^{132}Te/^{132}I	78.2 h	2.3 h
^{137}Cs/^{137m}Ba	30.1 y	2.55 min
^{188}W/^{188}Re	69.4 d	17.0 h
^{44}Ti/^{44}Sc	60.0 y	3.93 h
^{68}Ge/^{68}Ga	278 d	67.7 min

2.2.3.2 Radiochemistry of Radioisotopic Generators

Once a parent/daughter system is identified as idoneous according to its nuclear properties for generator construction, a new set of challenges is faced. There is a need for an effective radionuclidical separation that allows both: potential use of the daughter nuclide in the desired application and conservation of the parent nuclide for further daughter production. Further, the designed system has to be simple, reliable, and easy to use.

Liquid-liquid extraction was one of the first approaches and it is still used to date (e. g. ^{72}Se/^{72}As, (25)). However, simplicity is not one of the virtues of these generators. Long manipulation times

of open radiation sources (resulting in high radiation exposure) are never desired for general use. Chromatographic columns are the best chemical separation systems to produce radioisotopic generators. The parent nuclide has to be trapped with high specificity in the column material while no (or very low) attachment must be shown for the daughter nuclide. Thus, eluting the column with a given solution will yield pure daughter ready for applications. The column material is also preferred to be inorganic, to minimize a radiolytical effect (Fig 12).

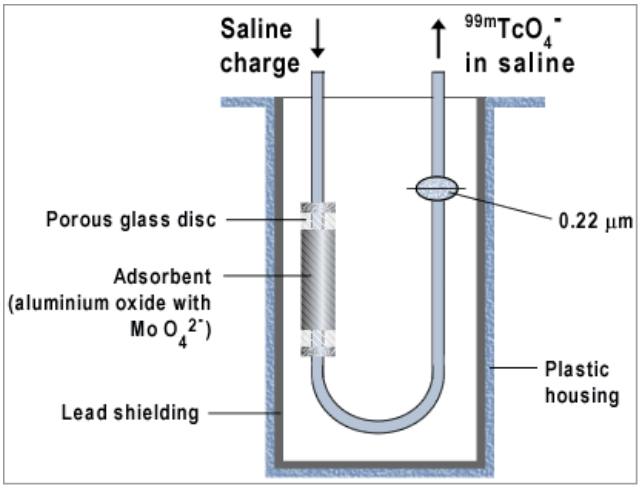

Fig 12 Schematics of the $^{99}Mo/^{99m}Tc$ generator's chromatographic column (26).

However, sometimes it is virtually impossible to achieve ideal conditions. So it's the case of the $^{90}Sr/^{90}Y$ generator, in which ^{90}Sr is absorbed in an organic cation exchanger and the daughter (^{90}Y) is eluted or "milked" from the column using a diluted (0.005 M) EDTA solution. The EDTA chelation of ^{90}Y severely limits the applications of the radioisotope; therefore extended post-elution treatment has to be made in order to obtain pure, ionic ^{90}Y for medical applications (27). Some of the available radioisotopic generators for medical applications are shown on Table 5.

Table 5 Some commercially available radioisotopic generators for medical use

Pair	Separation Technology	Use	Drugs Available	Nuclear Imaging
$^{90}Sr/^{90}Y$	Cation Exchanger	Therapy	TheraSpheres, RMTSpheres.	PET-double scape, pure beta emitter
$^{188}W/^{188}Re$	Alumina	Therapy	HDD/lipiodol, phase II	Planar Scan, SPECT
$^{99}Mo/^{99m}Tc$	Alumina	Diagnostic	Sestamibi, Sulfur Colloids, MAA, others	Planar Scan, SPECT
$^{44}Ti/^{44}Sc$	AG-1x8	Diagnostic	None Approved	PET
$^{68}Ge/^{68}Ga$	TiO_2, SnO_2	Diagnostic	DOTATOC, phase III	PET

2.2.3.3 The $^{68}Ge/^{68}Ga$ generator.

Several inorganic matrices have been used to construct the $^{68}Ge/^{68}Ga$ generator: Al_2O_3 (28), TiO_2 (29), α-Fe_2O_3 (30) and SnO_2 (31). Lately, attempts to use organic resins have been made (32). These generators benefit from the fact that there should be no metallic impurities in the eluate, thus producing better labeling. However concerns about radiolysis and the insertion of other organic contaminants are still present. These organic generators are still under evaluation. Table 6 resumes the technology currently available for production of $^{68}Ge/^{68}Ga$ generators.

Table 6 Available $^{68}Ge/^{68}Ga$ Generator Systems

Generator matrix	^{68}Ga elution yield (%)	Eluent	^{68}Ge content in the eluate	Other Contaminants
Al_2O_3 - Not Commercialized	60-70% initially, decreasing to under 40%.	0.005 % EDTA	More than 0.001% of the generator activity	Contains Al^{3+} in huge amounts
Al_2O_3 - Not Commercialized	50% for more than a year	NaOH solution (pH=12)	0.0001% of the total activity when combined with a second Al_2O_3 column.	Around 20 ppm of Al^{3+}
TiO_2 (Second Generation, IGG-100) - Eckert & Ziegler	60-80% for two years	0.1 N HCl	< 0.00001%	Low amounts of Ti and others
SnO_2 - iThemba Labs	75-80% for two years.	1N HCl	0.0002%	Low amounts of Sn and others
Liq-Liq Not Commercialized	60%, huge losses in ^{68}Ge in reextraction.	8-hydroxyquinoline	0.003%	No metal impurities
SiO_2 ITG GmbH	80 % for 6 month	0.05 M HCl	0.005%	No metal impurities
Organic Matrix - Not Commercialized	70-80% stable for 2 years (with very low ^{68}Ge initial activity).	0.1 N HCl	0.0001%	No metal impurities

From the two commercially available generators, iThemba Labs's SnO_2 and Eckert and Ziegler's TiO_2, the one with the best results (already with FDA's manufacturing authorization (33)) is the later (Fig 13). SnO_2 generators have the additional complication of high HCl content in the eluate, making it harder to buffer for labeling. However, the iThemba Labs generator is nearly 7 thousand dollars cheaper than the TiO_2 (Eckert and Ziegler). The iThemba Labs generator could

benefit from a ^{68}Ga pre-labeling concentration/ purification method which would ease the use of the eluted ^{68}Ga.

Fig 13 Eckert & Ziegler IGG 100 Gallium-68 radioisotopic generator

2.3 Lung Perfusion Agents

Lung perfusion scintigraphy with ^{99m}Tc-MAA is the current medical gold standard for the diagnosis of pulmonary embolism (34). The principle is that intravenously injected labeled microparticles (^{99m}Tc-MAA, > 10 µm) will be trapped in the lung's capillaries (or pre-capillaries with diameter of 7-10 µm (Fig 14) (35)) causing temporary micro-embolisms (36). The number of these embolisms is proportional to the local rate of blood flow (37). After elimination from the lungs (biological half-life of 1-24 h (38; 39)) ^{99m}Tc is excreted to the urine (40). The radioactivity allocation in the lungs is used to detect areas of poor or absent blood perfusion and to localize the embolism.

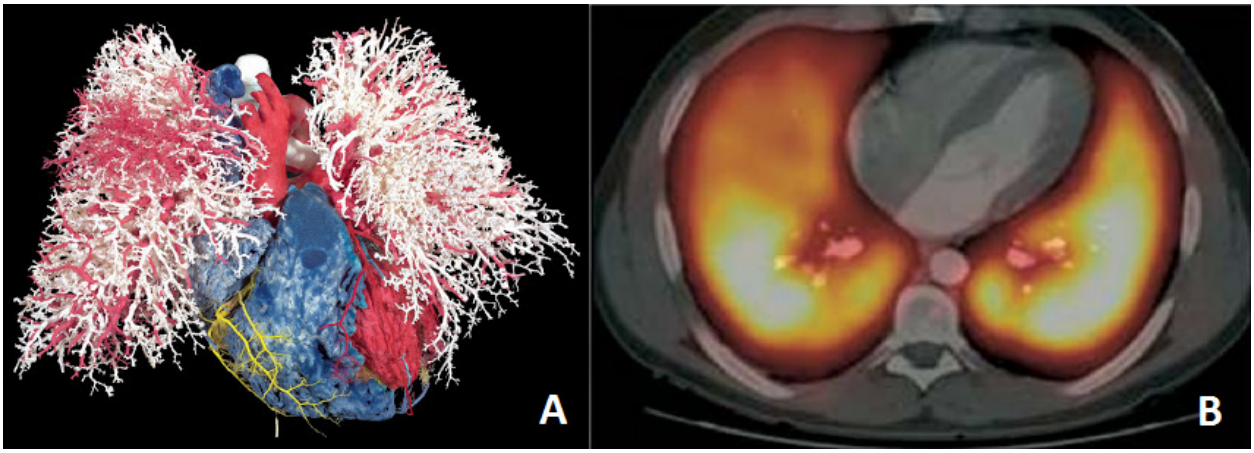

Fig 14 A: Lung corrosion cast showing vasculature (41), and B: Lung perfusion SPECT with ^{99m}Tc-MAA (42)

Although the use of MAA as a perfusion agent is extensive, it has been acknowledged to not be "ideal" (43). The presented size distribution (10-90 µm) did not comply with optimal specifications (20-40 µm) to allocate in precapillary arterioles. Orientation of macroaggregates (seldom spherical) in the blood flow becomes important to determine "effective size", making it difficult to predict the *in vivo* behavior. Aggregate degeneration is another component making the size distribution variable and unreliable (43). The ideal (theoretical) perfusion particle should be spherical (size not to be dependent on particle orientation) with a size distribution of 13.5±1.5 µm, to allow distribution only in capillaries (estimated $2.8 \cdot 10^{11}$ available in lungs) and not precapillary arterioles (estimated $3 \cdot 10^{8}$ available in lungs) (43). However, for practical preparation purposes a size distribution of 30±10 µm is also considered safe since only about 10^{5} particles are injected (43). The highly anastomotic nature of pulmonary circulation assured no disruption in blood flow or pressure during lung perfusion imaging. Human Serum Albumin (HSA) microspheres (also called HAM) were identified early as potentially ideal perfusion agents. The first lyophilized kit was produced in 1970 (44) but needed a boiling water bath for high labeling yield. It also had thiosulfate (reducing agent) and detergent as part of the excipients,

due to the strong aggregation of the HAM. Aggregation and easiness of preparation are probably the main reasons why MAA prevailed over HAM as a lung perfusion agent.

Human albumin (MAA and HSA) has other known side effects ranging from nausea to cardiac arrest (45). Although these adverse reactions are extremely rare since the blood has a high human albumin concentration, there is always a risk for disease transmission (e.g. hepatitis C). Despite differences in MAA from the "ideal perfusion particle" (with respect to size distribution and morphology), there are no reports in the literature of failed studies or inconsistent distribution. Therefore ^{99m}Tc-MAA must be considered a satisfactory lung perfusion agent.

However, more to the point of this dissertation, another important application of ^{99m}Tc-MAA is in the Radiomicrosphere Therapy (RMT) planning (46). Non-spherical macroaggregates (MAA, 10-90 μm) are used to predict the distribution behavior of perfectly spherical spheres (SirTEX and TheraSpheres ≈ 30±5 μm) (Fig 2) used for RMT. Despite the differences in size and morphology, MAA prediction of particle allocation is a valuable tool in RMT planning; however, whether a better planning agent can ultimately produce a better outcome is still an open question.

2.4 Radiomicrosphere Therapy (RMT)

In 2010 new cases of primary liver and intrahepatic bile duct cancer in the US reached 24120, with 18910 deaths, and colorectal cancer new cases reached 142570 with 51370 deaths, which nearly half of the latter becoming metastatic liver cancer (47). Liver cancer (primary or metastatic) accounts for nearly 10% of all cancers in the US alone with incidence being even greater in eastern countries. Treatment modalities involve surgery (48), chemotherapy (49), chemoembolization (50), thermal ablation using radiofrequency or microwave probes (51; 52) and Radiomicrosphere Therapy (RMT) (53; 54). The current RMT, also called Selective Internal Radiomicrosphere Treatment (SIRT) is indicated for patients with unresectable liver cancer,

especially hepatic cell carcinoma and metastatic liver cancer (54). RMT in combination with chemotherapy, also known as chemo-RMT, has been proposed to improve patient outcome (3; 2).

The sphere size (≈30 μm) is slightly larger than the smallest blood vessels (≈10 μm), which assures the deposition of these particles as the arterial branches decrease in size. The narrow size distribution is necessary so that no particles escape and pass into the venous circuit. Further, the micro-vascular density of liver tumors is 3-200 times greater than the surrounding liver parenchyma (Fig 15), making the tumor allocation preferential with respect to normal tissue. The treatment undergoes several stages, as will be described next.

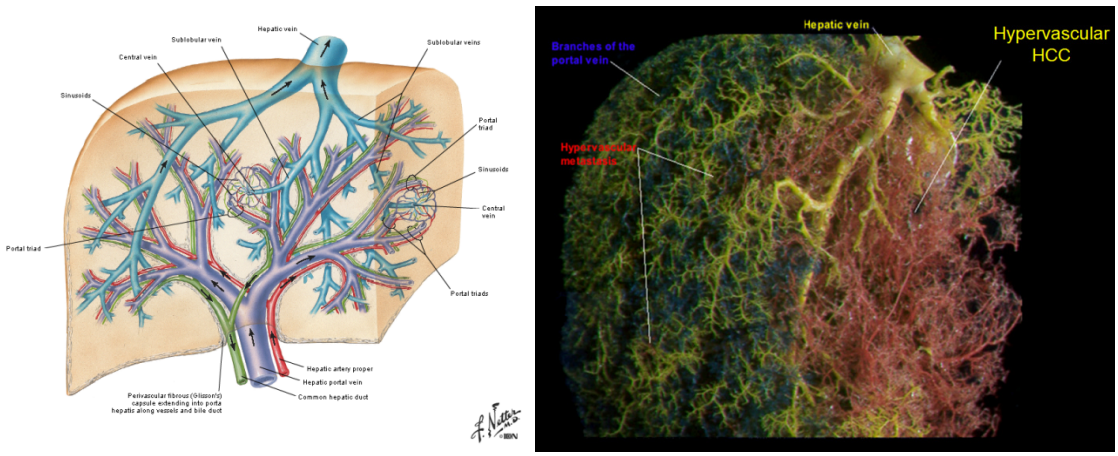

Fig 15. Anatomy of the Liver (55) and corrosion cast of the venous and arterial system (56)

When the patient is admitted several studies are performed including a ^{18}F-fluorodexoxy glucose or (^{18}F)FDG. A PET-CT scan is performed to assess tumor viability and to evaluate lesion (cancer) extent. A biopsy is also recommended to determine the nature of the cancer. If RMT or chemo-RMT is indicated as the proper treatment option, the patient is then prepared for treatment planning. The patient is put under local anesthesia and a catheter is inserted through the patient's groin and guided towards the hepatic artery under fluoroscopic imaging (Fig 16). Dyes are injected (hepatic angiogram) to identify the branches that go to the stomach and other organs.

These branches are properly coil embolized to prevent the particles from moving to these areas (Fig 16). The angiogram also provides valuable information about the main branches feeding the tumor, this information is used for the treatment planning as well (57).

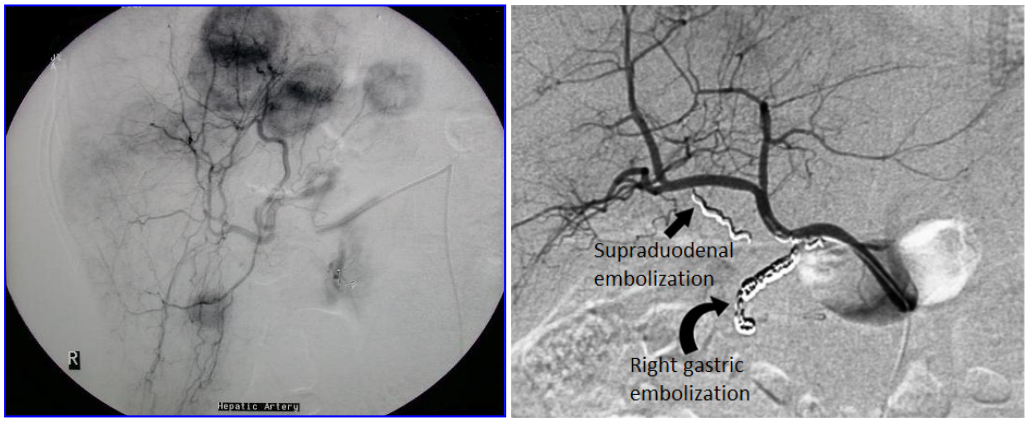

Fig 16. Hepatic Artery Angiography with preferential flow to tumors and coil embolization example (58).

Once all the steps are completed, macroaggregated albumin particles labeled with ^{99m}Tc are injected into the site. A planar scintigraphy to visualized lung, gastrointestinal (GI) and liver allocations is performed after injection (Fig 17). The tumor to liver ratio is also calculated to evaluate the potential effectiveness of the future treatment. The greater the tumor/liver ratio, the greater the potential effect of RMT while reducing the damage to healthy liver. The liver to lung ratio is used to evaluate if some of the therapeutic particles will allocate in the lungs after injection and produce radiation pneumonitis. If 20% or more of the particles go to the lung then the patient is no longer a candidate for RMT or a different approach must be followed (2). If any GI allocation is observed, the conducing vessels need to be coil-embolized before the treatment is administered.

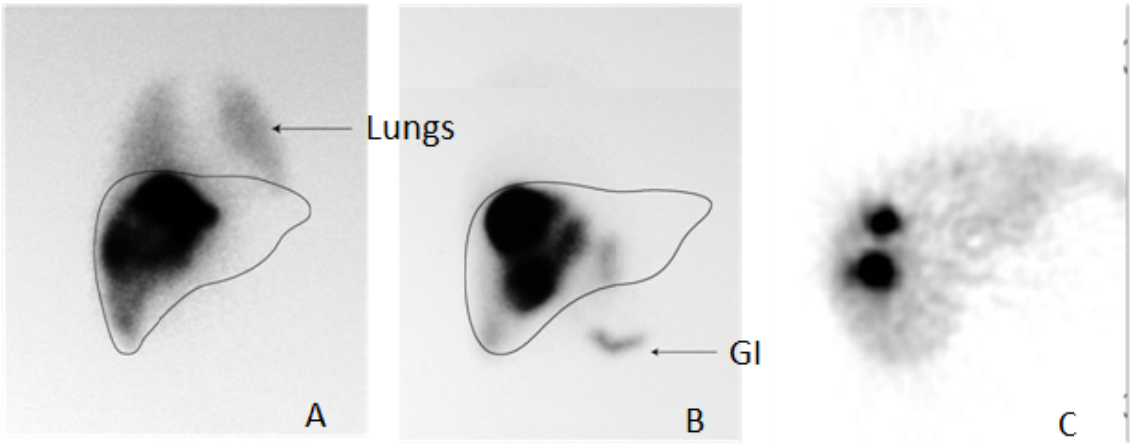

Fig 17. ^{99m}Tc-MAA Planar Scintigraphy. A: Significant lung shunting, B: Gastrointestinal uptake, C: Good uptake and tumor to liver ratio (58).

All the information obtained during the planning stage is used to determine the appropriate amount and location of radioactive spheres to be injected. A skillful surgeon can move the catheter to the right or left arterial branches or even deeper and inject a different amount of spheres directly to a specific tumor feeding arteries saving most of the healthy liver tissue (Fig 18). This assessment must be made on a patient-to-patient basis since clinical stages and anatomy of the tumor are significantly different most of the time (2).

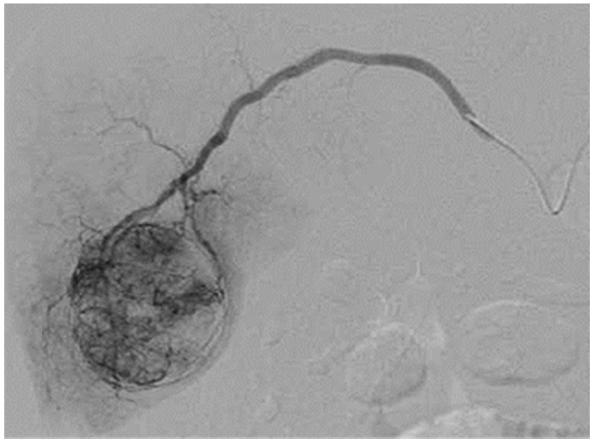

Fig 18. Skillful surgeon injecting deeper into the arterial system resulting in “highly selective” RMT (58)

Once the planning is complete, radiomicrospheres are injected into the different branches as planned and follow up PET and CT scans are performed to assess the effectiveness. Response to this treatment varies and over a third of all patients do not respond at all (59). The advantage of RMT plus chemo vs. chemo alone has been observed. In a double arm controlled phase II clinical trial RMT was selectively administered to half of the liver along with chemotherapy to the entire organ. This highly selective injection protocol allowed for half of the liver to be treated with Chemo-RMT while the other half with chemo alone (figure 7) (59) so that each patient could serve as their own control. The results clearly demonstrated the advantage of adding RMT to chemotherapy.

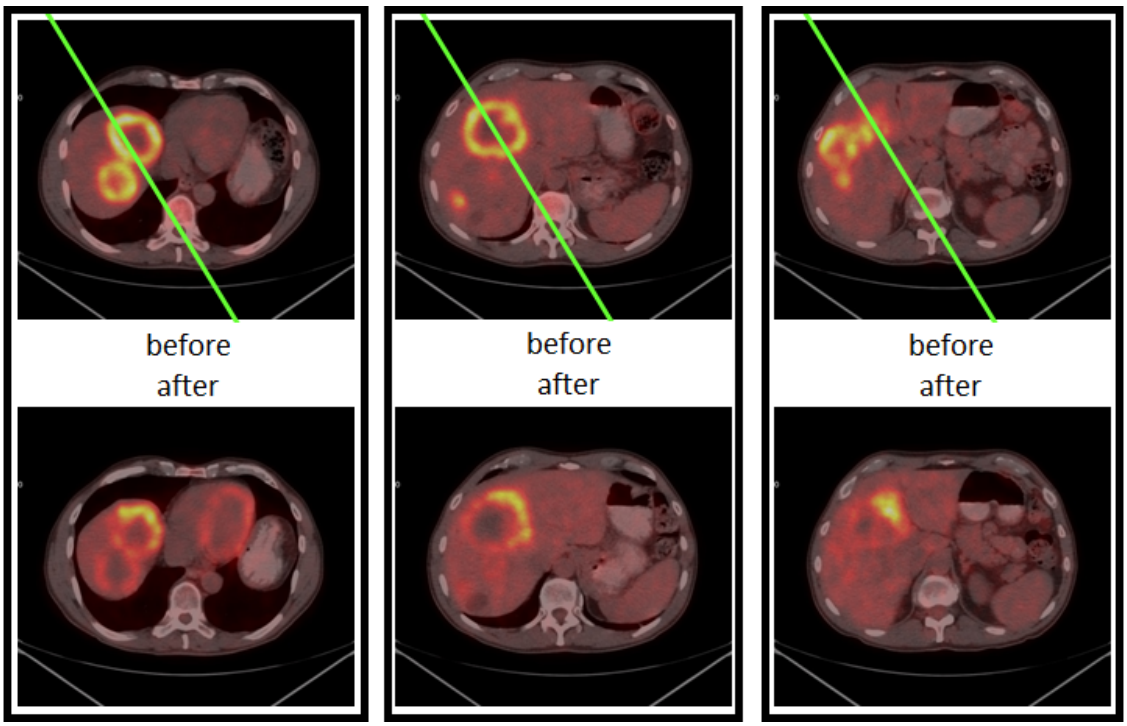

Fig 19. (^{18}F)FDG PET-CT before and after treatment in three patients, lower half of the liver (left of green line) treated with Chemo-RMT, other half (right of line) treated with Chemo only (59) demonstrating improved response of RMT combined with chemotherapy and the potential for "highly" RMT.

2.4.1 Limitations of RMT

The greatest limitation of RMT is the difficulty of dosimetric quantifications during the treatment planning. This is due to the fact that the ^{99m}Tc-MAA scintigraphy (Fig 20) is a single photon emission tomography technique (SPECT) and the difficulty in obtaining proper attenuation correction as compared to positron emission tomography (PET).

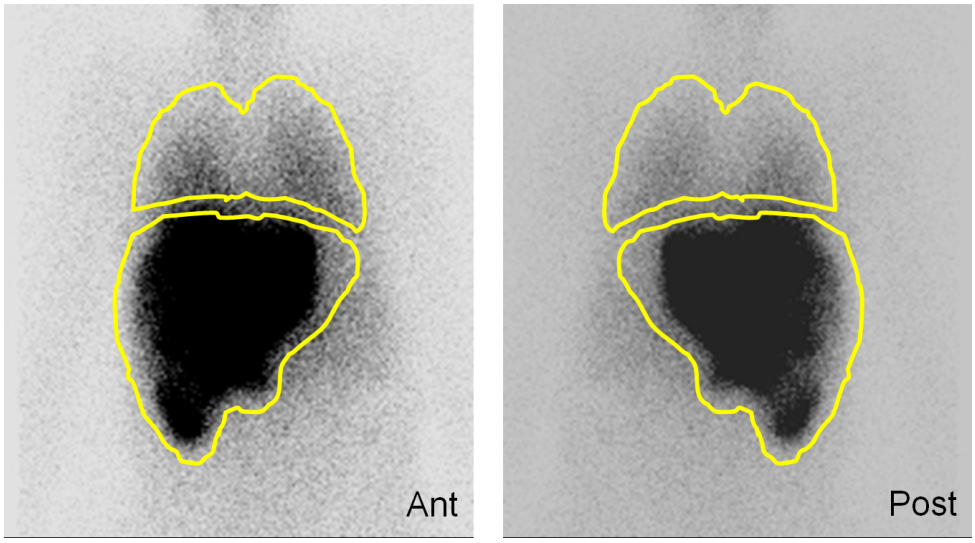

Fig 20. Anterior and Posterior ^{99m}Tc-MAA Planar Scintigraphy (58)

From the ^{99m}Tc-MAA planar image above (Fig 20) it is clearly impossible to determine what is lung and liver and how much overlapping exists. However better visualization is achieved when SPECT/CT is used (Fig 21) but as discussed previously quantification is very difficult.

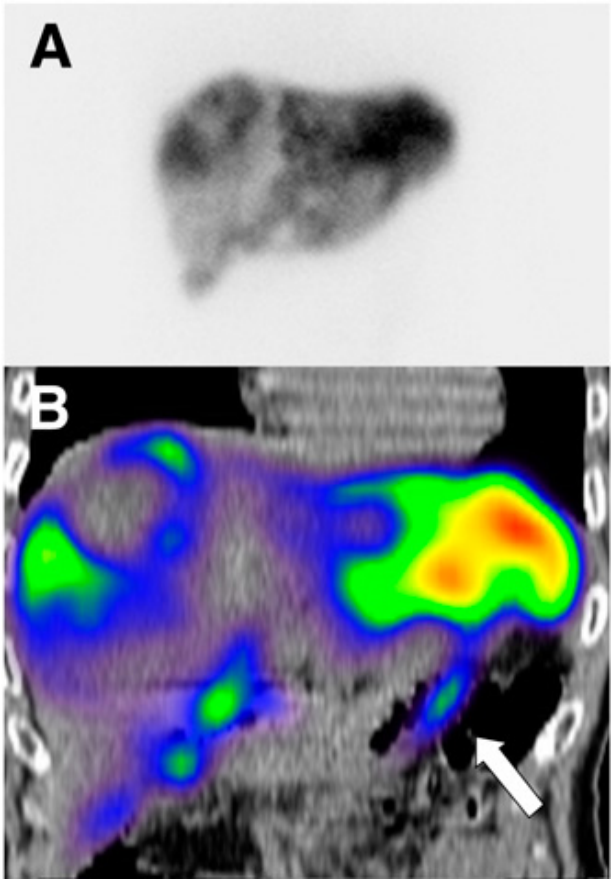

Fig 21 Duodenal accumulation (arrow) in a patient with colorectal cancer, not definable on planar images. A: planar scan, B:SPECT/CT coronal view (60)

The RMT planning will be greatly benefited by the inclusion of a PET isotope, since the technique is generally considered better than SPECT because of the ability for absolute attenuation correction and potentially superior resolution. Important advances were made in early years by labeling MAA with the PET isotope ^{68}Ga (61), obtaining an 80 % labeling yield and purity > 95% for the Pulmolite MAA kit. However the potential of ^{68}Ga-MAA was forgotten until recently, when new lung perfusion studies were made using this drug, partially due to availability of a reliable ^{68}Ge/^{68}Ga generator with minimal breakthrough impurities and high ^{68}Ga yield (62) (Fig 22).

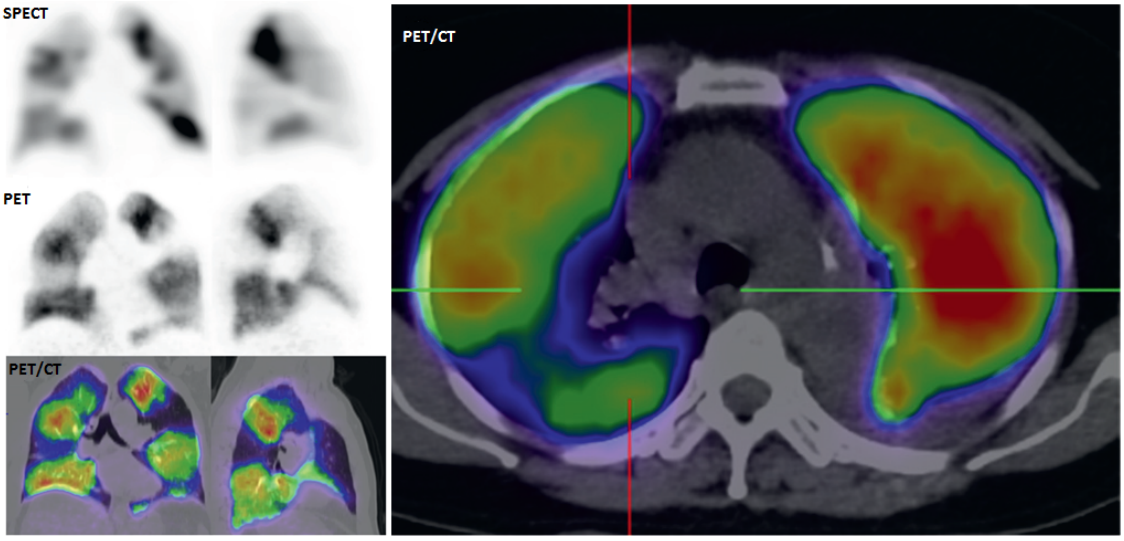

Fig 22 Results for ^{68}Ga-MAA lung perfusion studies showing areas of low perfusion not seen with ^{99m}Tc-MAA SPECT (62).

Similarly to ^{99m}Tc-MAA, ^{68}Ga-MAA use was quickly extrapolated to RMT planning (63). Preliminary results show some advantages of a PET tracer over the common ^{99m}Tc-MAA for SPECT in tumor/liver ratio calculations and lung shunting localization (Fig 23).

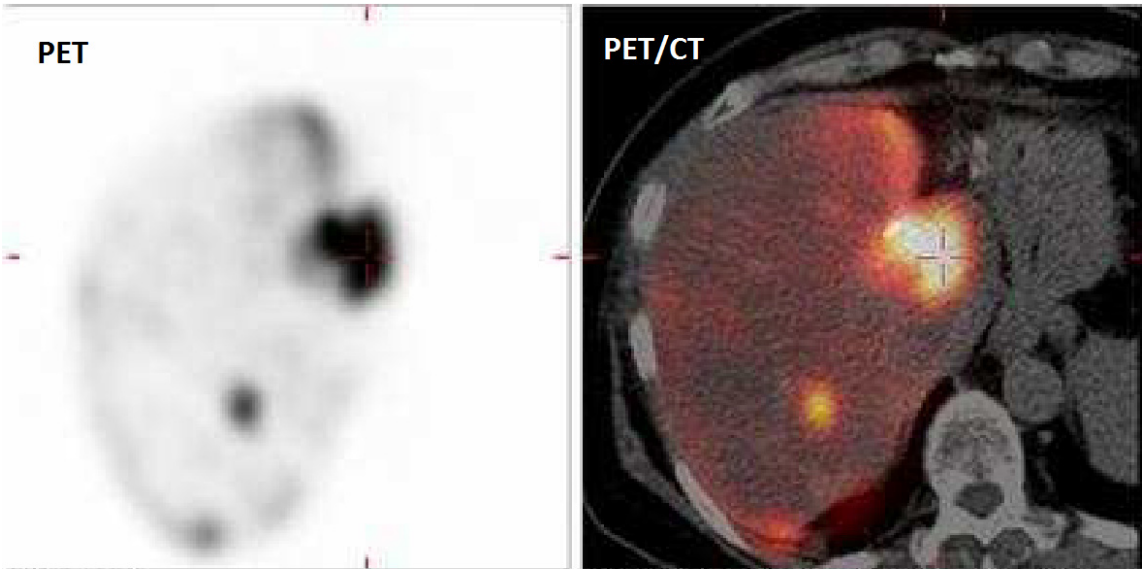

Fig 23 PET/CT image of ^{68}Ga-MAA used for RMT planning **(63)**

The ^{68}Ga-MAA used for both: the lung perfusion and RMT in planning studies; was prepared using the original MAA kit for ^{99m}Tc. This kit needs to be modified (washed) to obtain high ^{68}Ga labeling yields which increase manipulation and therefore the risk of product contamination (61). A ^{68}Ga specific lyophilized kit for labeling is not available in the market. Further, the MAA particles are supposed to act as surrogates for the ^{90}Y labeled spheres and thus serve to predict the volume distribution of the ^{90}Y. Imaging is mainly utilized for determination of lung-shunt fraction, and detection of extra-hepatic gastrointestinal uptake, both of which could be restrictive for safe administration of the treatment. Thus an accurate measurement is dependent on the distribution of the MAA particles and the assumption that its distribution will be identical to that of the ^{90}Y microspheres. However, the size (10 to 90 μm with no particle over 150 μm) and the very irregular shape of the MAA do not at all resemble spheres. Hence the MAA used for imaging and treatment planning is actually a poor surrogate for the ^{90}Y microspheres used for the actual therapy (Fig 2). Therefore, new biodegradable particles are needed for treatment planning.

CHAPTER 3 ^{68}Ga PURIFICATION SYSTEM

3.1 Abstract

Purification of ^{68}Ga obtained from the existing ^{68}Ge/^{68}Ga generators is a must. With great potential for radiopharmaceutical use, the long half-life of the parent nuclide (^{68}Ge, 278 days) demands absolute ^{68}Ga radionuclidical purity. Metal impurities (Ti, Sn, Fe and Zn mainly) also interfere in the radiopharmaceutical labeling process. A combination of chromatographic exchange resins was used and a full system was designed to be used in four simple steps: elution - cleaning - purification - extraction. The solutions concentrations and volumes were optimized. With low cost and less than 10 minutes processing, the final ^{68}Ga solution is easily buffered with Sodium Acetate for labeling. The disposable system can easily be recycled and re-sterilized to reduce cost even more. It is also an alternative for ^{68}Ga research laboratories since it can be used for over 100 elutions for more than 3 months without reconditioning for non-human applications and still provide reliable purification and labeling.

3.2 Introduction

Positron Emission Tomography (PET) is a medical imaging technique with high resolution and sensitivity. It can use the so called “biogenic” radioisotopes (^{11}C, ^{13}N and ^{15}O) produced in a cyclotron; however their short half-life (20.3 min, 9.97 min and 2.03 min, respectively) (64). The most used cyclotron produced radioisotope is ^{18}F (half-life 109.7 min) in its ^{18}FDG form. Another cyclotron produced radioisotope is ^{68}Ga, which can also be obtained from the ^{68}Ge/^{68}Ga generator. ^{68}Ga (half-life 68 min) presents great potential for radiolabeling of several imaging agents, especially peptides for theranostic applications. Whether it is cyclotron or generator produced, the product needs purification before labeling (65; 66). Existing systems employ either

acetone as elution media (65) which poses a patient risk or high HCl volumes that complicate handling (29) (Fig 24).

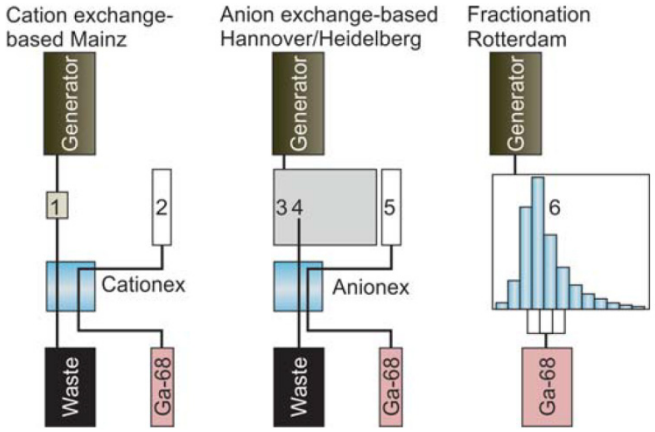

Fig 24 Schematic representation of available systems for ^{68}Ga post-elution processing (29). 1: Direct Elution; 2: Purification with HCl/Acetone mix after Cation absorption; 3: Elution to Conc. HCl; 4: Absorption into anion exchanger; 5: Desorption with water; 6: Fractionated elution.

Fractioning is a safer method than using acetone or high HCl volumes, however only around 60% of the eluted activity (already around 60 % of the activity of the generator) can be used (29). A new, cGMP capable, single use and low cost ^{68}Ga purification system is needed for radiopharmaceutical applications.

3.3 Materials and Methods

A combination of chromatographic exchange resins was used to build the purification system (67). Two luer-fitting column beds were prepared. First, 40±10 mg of AG-50Wx8 cation exchange (Eichrom, USA) column is connected to a three-way stopcock. Next, 15±5 mg of UTEVA® anion exchange (Eichrom, USA) resin in a column is positioned. Finally, another three-way stopcock is located at the end (Fig 25 Purification System setup). The purification of the ^{68}Ge/^{68}Ga eluent takes place in four simple steps: elution (from the generator, 5 ml of 0.1 M

HCl) - cleaning (1 ml of 0.1 M HCl) - purification (1 ml of 5 M HCl) – extraction (1 ml of Millipore Water).

3.4 Results and Discussion

The assembly of the purification system is simple and easy to use (figure 2).

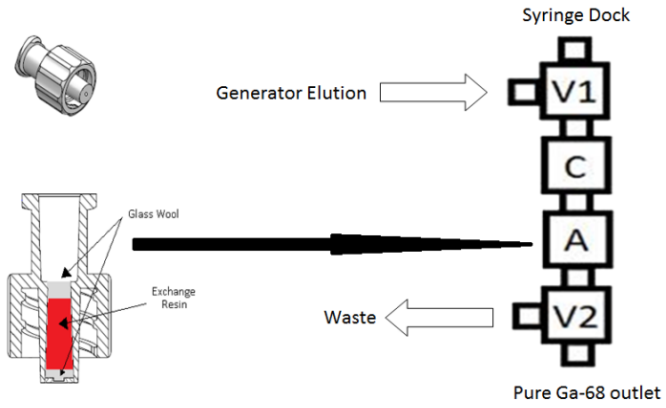

Fig 25 Purification System setup

The optimized and simple four-step purification process is as follows: 1. Elution of the generator using a 0.1 M HCl solution. During this step the gallium is trapped with most of the metal impurities in the cation exchanger. Most of the ^{68}Ge contamination is removed in this step. 2. Cleaning is performed with one extra mL of 0.1 M HCl through the syringe dock to remove the excess solution coming from the generator. One mL of air is then vented to the system. 3. Purification is performed with slow elution using 1 mL of 5 M HCl. The Ga^{3+} forms a $GaCl_4^-$ complex so it is released from the cation exchanger and absorbed onto the anion exchanger. One mL of air is also used to vent the system. All the metal impurities are eliminated in this step (especially Fe, Ti, and Zn). 4. Extraction is done using 1 mL of Millipore water in which the gallium complex is destroyed and released from the anion exchanger into the labeling vial. One mL of air is pushed through the system to remove most of the ^{68}Ga (figure 3). The purification

system retrieves approximately 85% of the eluted gallium activity after 10 minutes of processing. It provides pure, pre-concentrated ^{68}Ga in slightly acidic solution that is easily buffered by adding 0.3 mL of 3 N ultrapure sodium acetate (67). All the ^{68}Ge is eliminated in the process, consequently radio-nuclide impurities are eliminated from the labeling process.

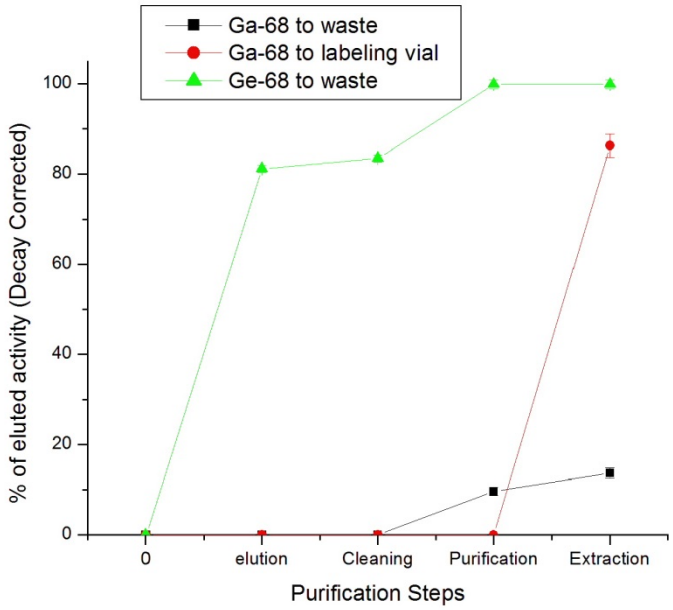

Fig 26 ^{68}Ga recovery and ^{68}Ge elimination during the purification process

The purification system can be reused for 100+ times without altering its performance. However to maintain sterility it is recommended to be used once and disposed of or reconditioned.

3.5 Conclusions

An inexpensive, simple to use and cGMP capable purification and preconcentration method for the ^{68}Ga generator elution was created and optimized. Labeling yields obtained for different products are high (90 - 99.9 % depending on the application) and consistent. Great repeatability was shown in all purifications. The system is used but not limited to the Eckert and Ziegler IGG-

100 ^{68}Ge/^{68}Ga generator. It has also been used for purification of cyclotron produced ^{68}Ge and it is a good candidate for use with the iThemba ^{68}Ge/^{68}Ga generator.

CHAPTER 4 ^{68}Ga-MAA

4.1 Abstract

Rapid developments in the field of medical imaging have opened new avenues for the use of positron emitting labeled microparticles. The radioisotope used in our research was ^{68}Ga, which is easy to obtain from a generator and has good nuclear properties for PET imaging. METHODS: Commercially available macroaggregated albumin (MAA) microparticles were suspended in sterile saline, centrifuged to remove the free albumin and stannous chloride, re-lyophilized, and stored for later labeling with ^{68}Ga. Labeling was performed at different temperatures and times. ^{68}Ga purification settings were also tested and optimized. Labeling yield and purity of re-lyophilized MAA microparticles were compared with those that were not re-lyophilized. RESULTS: MAA particles kept their original size distribution after re-lyophilization. Labeling yield was 98% at 75 ºC when a ^{68}Ga purification system was used, compared to 80% with unpurified ^{68}Ga. Radiochemical purity was over 97% up to 4 hours after the labeling. The re-lyophilized MAA and labeling method eliminates the need for purification and simplifies the labeling process. Animal experiments demonstrated the high *in vivo* stability of the obtained PET agent with more than 95% of the activity remaining in the lungs after 4 hours.

4.2 Introduction

Starting in 1964, several efforts have been made to find an agent for perfusion and embolization (68; 69). A lyophilized kit for the preparation of ^{99m}Tc-MAA was created in 1974 for Single Photon Emission Tomography (SPECT) imaging. With the arrival of Positron Emission Tomography (PET) the formulation of an analogue drug with a positron emitter was needed. Among the available PET isotopes ^{68}Ga is easily obtained from its parent nuclide ^{68}Ge by chromatographic column separation with different inorganic exchangers. The long lived parent

allows the construction of a generator that can last up to two years (70) compare to a ^{99m}Tc/^{99}Mo generator which lasts only for 1-2 weeks. MAA was first successfully labeled with ^{68}Ga in 1989 (61), but never used, probably due to unreliability of the existing ^{68}Ge/^{68}Ga generators and low availability of PET imaging cameras. Revived interest has been shown recently (71), and the first PET lung perfusion studies in humans have been performed (Fig 27) (62).

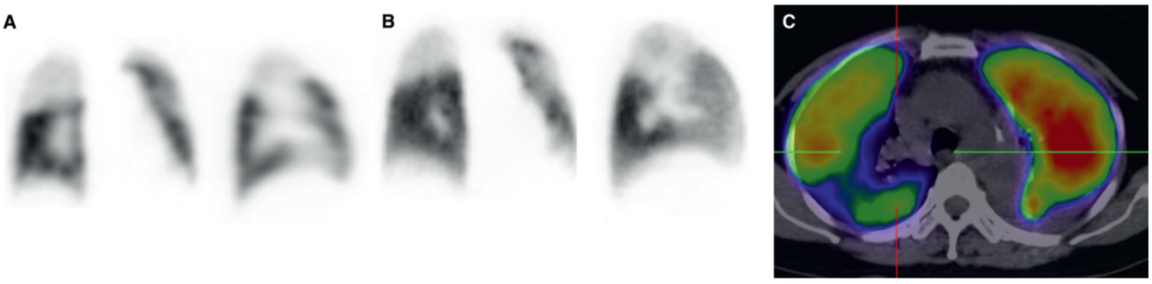

Fig 27 Comparison of A: Coronal and sagittal SPECT perfusion; B: Coronal and sagittal PET perfusion and C: axial PET/CT perfusion WITH ^{68}Ga-MAA

Radiomicrosphere Therapy (RMT), a technique used to treat metastatic liver cancer, could also benefit from a PET perfusion tracer. During the planning stage, a ^{99m}Tc-MAA perfusion scan is performed to assess the allocation in lung and gastrointestinal tract. It is also used to calculate tumor to normal liver allocation ratio (46). The distribution acts as a predictor of the treatment safety and effectiveness. A PET perfusion agent (e.g. ^{68}Ga-MAA) could provide valuable, quantifiable information to calculate precise doses, which could potentially improve the treatment outcome. Initial work with ^{68}Ga-MAA for RMT planning has already been performed (72).

All reported ^{68}Ga labeling of MAA has been done using a commercial MAA kit for ^{99m}Tc. The original kit contains 100 µg of stannous chloride and free albumin; hence the particles need to be washed with saline before ^{68}Ga labeling. The maximum reported labeling yield using this kit is around 80% (71). Elimination of the free ^{68}Ga via centrifugation is therefore necessary. The purification process is also required to eliminate traces of the long half-life ^{68}Ge that are eluted

from the generator. A new ^{68}Ga specific MAA lyophilized kit is needed for labeling. Further, it needs to be combined with a pre-purification system that assures prior elimination of ^{68}Ge traces and provides pure, pre-concentrated ^{68}Ga for labeling.

4.3 Materials and Methods

4.3.1 MAA lyophilized kit preparation

Macroaggregated Albumin (MAA) was obtained from Triad Isotopes® (DraxImage® Kit). The content was reconstituted with 0.9% saline solution, separated into two 15 ml centrifuge tubes, centrifuged (Eppendorf, Germany) and the supernatant discarded ("Washed MAA") (61). The particles were then re-lyophilized overnight and stored for labeling ("Re-Lyophilized MAA"). Size and morphology analysis was performed on the reconstituted MAA using an optical microscope (Micromaster, Fisher-Sci, USA) and a hemacytometer (Reichert, USA) before and after re-lyophilization. The ^{68}Ge/^{68}Ga generator used was the 50 mCi IGG-100 (Eckert & Ziegler, Germany), based on the TiO2 resin technology, eluted with 5 ml of 0.1 M ultrapure HCl (Sigma-Aldrich, USA) solution.

4.3.2 MAA Labeling

Both, washed MAA and re-lyophilized MAA, were labeled (using the original Green's method (61; 71)) with either purified or unpurified ^{68}Ga solution. The unpurified ^{68}Ga solution was obtained directly from the generator (5 ml, pH=1). The purified ^{68}Ga elution (1 mL with pH=0.6) was obtained from the purification system. Both were buffered using 0.3 ml of 3N ultrapure sodium acetate (Sigma-Aldrich, USA). The solution was added to the 15 ml centrifuge tube containing the MAA. Labeling was performed using a thermomixer with a heating block for 15ml centrifuge tubes and stirring at 750 rpm (Eppendorf, Germany). Labeling temperature was 25 (room temperature), 50, 75 and 95 degrees Celsius. Labeling time was set at 15 minutes based on

previous reports of ^{68}Ga-MAA labeling kinetics (61; 71). Particles were separated from the supernatant by centrifugation. The particles and supernatant were measured separately using an Atomlab 100 dose calibrator (Biodex, USA). Final particles were re-suspended in 5mL saline solution with a vortex mixer (Fisher-Sci, USA).

4.3.3 Lung Perfusion Experiments:

Sprague Dawley rats (200-225 grams, 2 per time point) were obtained from Harlan Laboratories (Harlan, USA). Animals were weighed before the procedure and anesthetized using an Ohmeda Isotec 3 isolfurane vaporizer (GE Healthcare, USA). Isolfurane levels were kept ≤3 % at all times. Once completely anesthetized, animals were restrained in the supine position and a torso X-Ray was obtained (Belmont Acuray 071A, USA). Later, 100 µL of the labeled MAA (8,000-10,000 particles) with an activity ranging from 50 to 100 µCi (1.85-3.7 MBq) was injected through the lateral tail vein. Animals were euthanized at 2 or 4 hours. For either time points their lungs, liver, spleen, heart, kidneys, ribs and 0.2 ml of blood and urine were collected, weighed and activity measured using a Cobra 5000 well counter (Packard, USA). Un-collimated autoradiography images (in the unaltered supine position the X-Ray was obtained) were also taken at 1, 2, 3 and 4 hours (Packard Phosphorimager, Perkin Elmer, USA). Free ^{68}Ga was injected as a control. Additionally, imaging and organ collection were performed following ^{99m}Tc-MAA and free ^{99m}Tc injection for comparison purposes. ^{99m}Tc-MAA and $Na^{99m}TcO_4$ were purchased from a local pharmacy (Triad Isotopes®, USA). Pertechnetate was reduced with 100 µg of Stannous Chloride (Sigma-Aldrich, USA) before injection. The obtained X-Rays and the autoradiography images were superimposed to provide anatomical and functional data.

4.4 Results and Discussion

4.4.1 MAA re-lyophilization

The elimination of the excess free albumin is a necessary step prior to successful labeling with ^{68}Ga ("washed MAA") [4, 5]. Re-suspension of the particles was fast using a vortex mixer; manual shaking of the vial was also efficient. Re-lyophilization of the MAA did not change either the particle's size distribution or morphology (figure 1).

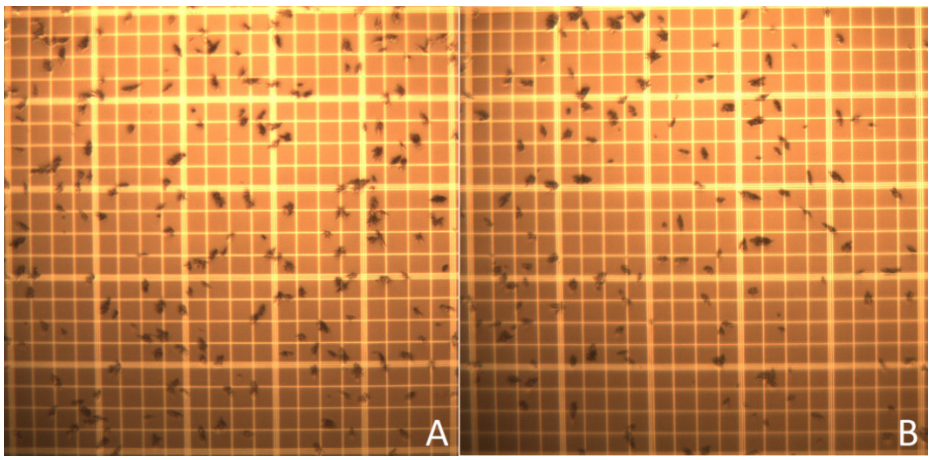

Fig 28 MAA microscope images; A: From original un-modified MAA kit and B: From re-lyophilized MAA.

4.4.2 MAA Labeling

Labeling yield of MAA with unpurified ^{68}Ga was 78.3±3.1 % after 15 minutes at 75 ºC, similar to that reported by other investigators [4]. A labeling yield of 72.1±6.2 % was obtained at 50 ºC (Figure 4). Better labeling yield (96.9±2.1 %) was obtained at 95 ºC, however the particle morphology was considerably changed. Smaller particles were detected and in higher concentration, apparently due to the rupture of bigger macroaggregates. The labeling yield at room temperature was 50±4 %. Radiochemical purity tests were conducted for all the products showing more than 97% *in vitro* stability in all cases after 4 hours.

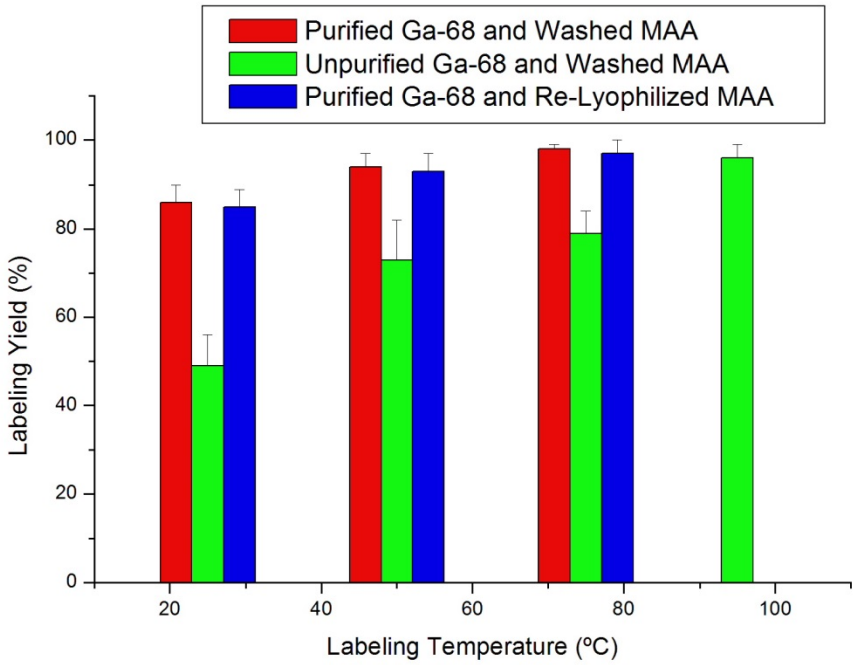

Fig 29 ^{68}Ga-MAA labeling yield results.

The introduction of the ^{68}Ga purification system improved the labeling yield significantly ($p<0.003$). An 84.1±3.1 % labeling yield was obtained at room temperature (25ºC). This yield is higher than the maximum yield obtained at 75 ºC with unpurified ^{68}Ga. However, if room temperature labeling is performed, post-labeling purification is still needed to assure a final radiochemical purity >90 %. In the particular case of MAA, labeling at up to 75ºC has been proven to not damage the particles. Nevertheless, synthesis near room temperature or elimination of the heating step all together is obviously desirable. Good labeling yield of 92.8±2.6 % was obtained at 50 ºC. However, when labeling at this temperature, purification is still recommended since nearly 10 % of free ^{68}Ga will be present in the final product.

The labeling of MAA with purified ^{68}Ga yielded the best results at 75 ºC (figure 4). A labeling yield of 97.6±1.5 % was obtained after 15 minutes of reaction. Particle distribution and morphology remained well within specifications and a >95% radiochemical purity was obtained.

Labeling at this temperature eliminates the need for a final purification of the product, rendering the radiopharmaceutical ready for injection immediately. Experiments with purified ^{68}Ga-MAA at 95 ºC were not performed because of the previously observed particle change at that temperature.

Re-lyophilized MAA labeling with purified ^{68}Ga showed no significant difference from the results obtained with the Washed MAA (but not lyophilized, $p>0.8$). The elimination of the free albumin and the stannous chloride from the original formulation followed by re-lyophilization of the MAA does not compromise either re-suspension or morphology (and size distribution) of the particles. The re-lyophilized MAA (or MAA prepared without $SnCl_2$ and free albumin), in combination with the ^{68}Ga purification system, allows for the preparation of a single-use lyophilized kit for the preparation of ^{68}Ga-MAA. This kit can be used for Positron Emission Tomography in lung perfusion studies, radiomicrosphere therapy (for liver cancer) planning and other applications requiring perfusion imaging.

4.4.3 Lung Perfusion Experiments:

More than 97% of the injected dose per gram of (ID/g) ^{68}Ga-MAA activity was detected in the lungs after tail vein injection (seen in the image taken after 10 minutes, not shown) and until at least 4 hours after injection (Fig 30). Less than 2 % of ID/g activity was measured in any organ other than lungs after 2 and 4 hours. In contrast, most of the injected free ^{68}Ga (> 60 %) remains in the blood after 4 hours (presumably as ^{68}Ga-native transferrin complex). The remaining activity was extracted by the kidneys to the bladder (13 %) or absorbed by the liver (15 %).

The behavior and "*in vivo*" radiochemical purity of ^{99m}Tc-MAA was different than that of ^{68}Ga-MAA. ^{99m}Tc was slowly released from the MAA and extracted by the kidneys into the urine (7.6±1.3 after 2 hours and 12.3±1.2 after 4 hours). Only 86.6±0.7 % of the decay corrected activity was found in the lungs after 2 hours, decreasing to 79.2±1.5 % at 4 hours.

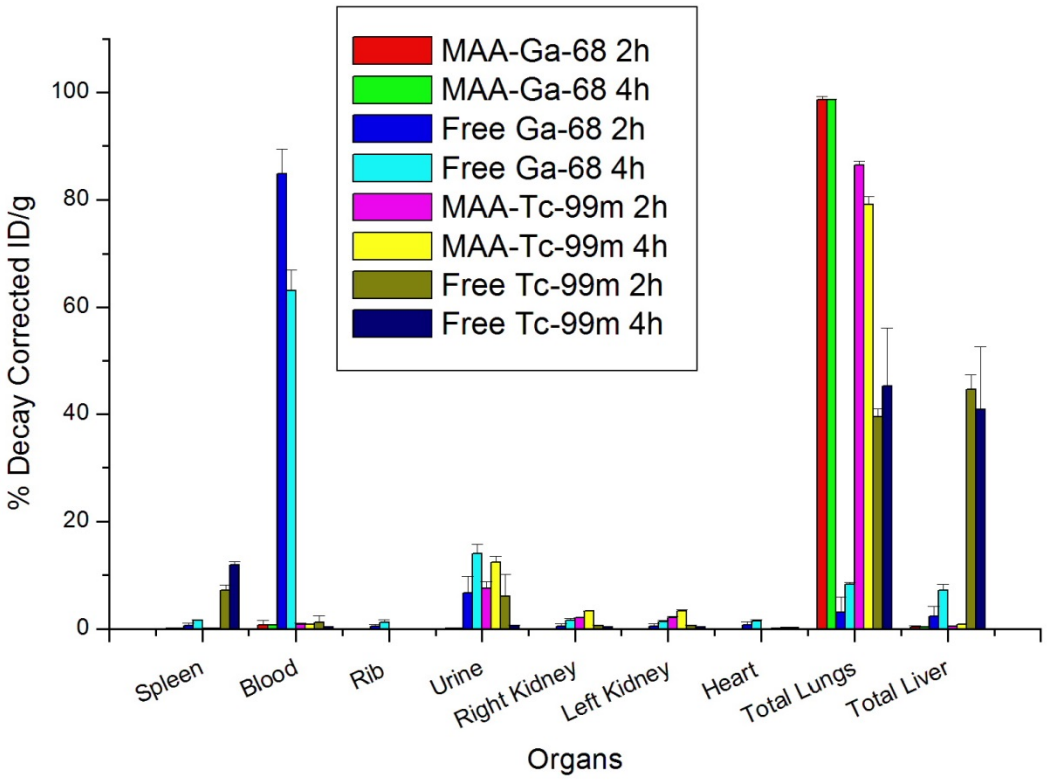

Fig 30 Decay Corrected Organ Biodistribution of ^{68}Ga-MAA, free ^{68}Ga, ^{99m}Tc-MAA and free ^{99m}Tc.

Free ^{99m}Tc (reduced with $SnCl_2$) allocates mainly in the lungs and liver. The % ID/g did not change over the study period. ^{68}Ga-MAA exhibited better *in vivo* stability than ^{99m}Tc-MAA (Fig 30). The autoradiography images clearly showed the preferential allocation of ^{68}Ga-MAA in the lungs over the period studied (Fig 32). The drug-product in-vivo half-life was determined using regions of interest in the autoradiography images. A square cell of 40x40 mm was used to count the activity in the lung region for each time point. For ^{99m}Tc-MAA biological half-live was found to be T½=11.4±1.7 hours. This is consistent with the previously reported value of 11.5±4 hour biological half-life (73). The biological half-life of ^{99m}Tc-MAA is not to be confused with the MAA biological half-life. These are equal only if 100% *in vivo* radiochemical purity of ^{99m}Tc-MAA is assumed. The assumption was reinforced by the fact that injected free ^{99m}Tc behaves

differently than that released from the MAA (Fig 30 and Fig 32). The only feasible explanation is that when free ^{99m}Tc is injected it forms nanocolloids with the $SnCl_2$, being absorbed by the liver and lungs. While ^{99m}Tc released from the MAA is quickly absorbed by the kidneys. Furthermore, it is very unlikely that some form of degraded ^{99m}Tc-Albumin will be absorbed by the kidneys for excretion rather than be degraded in the liver. For over 40 years MAA half-life was considered to be in the 6-12 hour range (68; 73). However if MAA half-life happened to be so short, degradation would have been observed in the ^{68}Ga-MAA experiments. The stronger ^{68}Ga-MAA binding, with superior *in vivo* stability, proves that MAA half-life is much longer than previously assumed (46) and the shorter half-life can be attributed to the poorer stability of ^{99m}Tc-MAA.

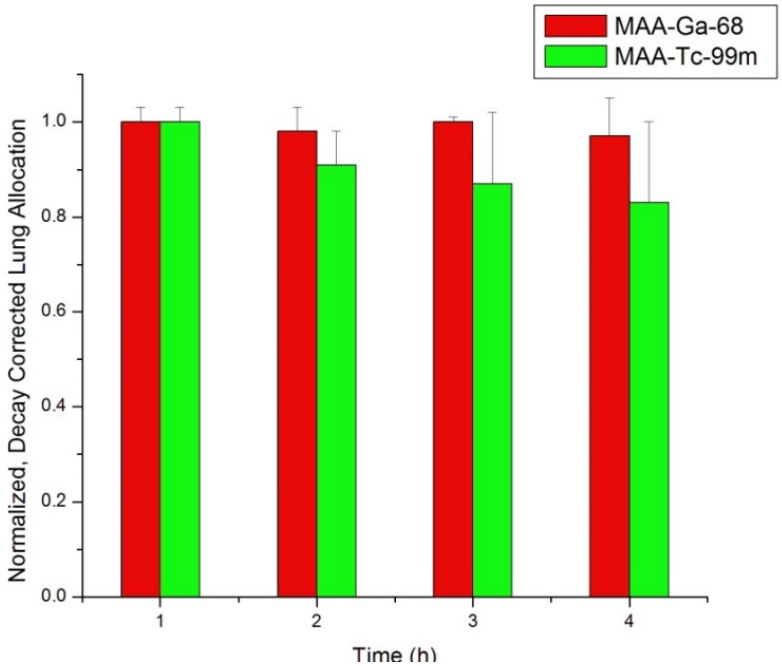

Fig 31 Normalized and radio-decay-corrected lung allocation for ^{68}Ga-MAA and ^{99m}Tc-MAA at 1, 2, 3 and 4 hours (n=2 per time point).

The assumption of a shorter MAA half-life has little or no implication in lung perfusion studies or probe guided surgery. However a greater implication is present when using the radiolabeled MAA in planning for liver cancer RMT. The radio-microsphere technique is based on several

planning steps. One of them is a particle distribution assessment using ^{99m}Tc-MAA, mainly to determine lung and gastrointestinal (GI) allocation after hepatic artery injection. If only liver allocation is found (less than 20% lung allocation and no GI allocation), then the radio-microsphere treatment is administered after 48 hours since the MAA is assumed to have been cleared from the vessels (assuming a MAA half-life of 6-12 hours). Despite the wrong MAA half-life assumption, the treatment is successful. Therefore, it must be concluded that the effectiveness of the treatment does not require the complete decay of the treatment planning microparticles. Because they are injected in small numbers, enough arterioles seem to still be available for the allocation of the therapy particles. However, whether or not the treatment could benefit from the use of faster degrading planning particles (faster than MAA), remains an open question. Nevertheless, a precise determination of MAA half-life is needed, and can probably be measured by combining the strong gallium binding with an isotope with a longer radioactive half-life (e.g. ^{67}Ga-MAA, $t_{½}(^{67}Ga)$= 3.26 days).

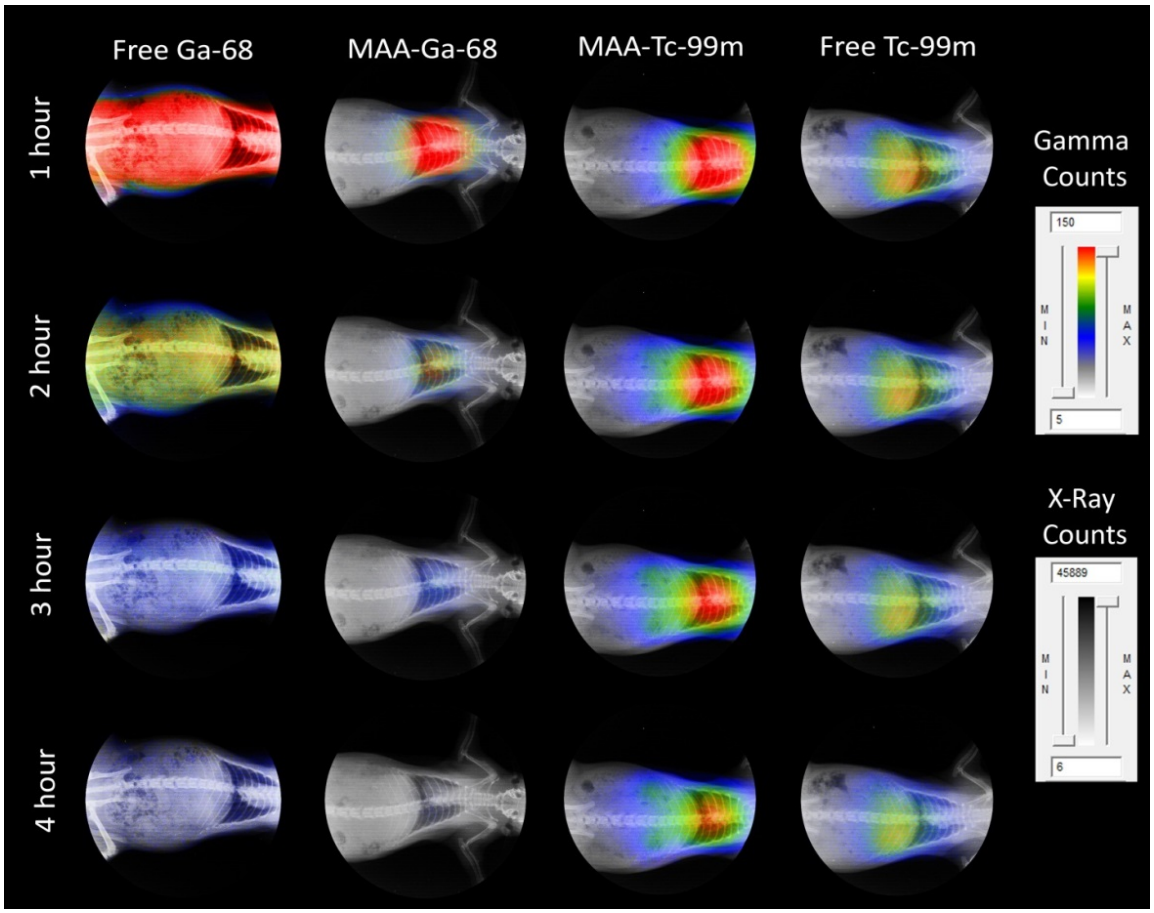

Fig 32 Non decay-corrected, un-collimated full body autoradiography for free ^{68}Ga (T½= 68 min), ^{68}Ga-MAA, ^{99m}Tc-MAA and free ^{99m}Tc (T½= 6.02 h) at 1, 2, 3 and 4 hours. Labeling of ^{68}Ga-MAA was performed with re-lyophilized MAA and purified ^{68}Ga at 75 ºC for 15 minutes. The autoradiograph is superimposed on an X-ray image of the same animal in the unaltered supine position.

The re-lyophilization of washed MAA was a first approach to show the feasibility of a lyophilized kit specifically for ^{68}Ga-MAA. In a production facility the pharmaceutical development would need to be different from that of the ^{99m}Tc-MAA kit. Free albumin and $SnCl_2$ would not need to be added to the final product. The high labeling yield obtained during the preparation of ^{68}Ga-MAA eliminates the need for final centrifugation for purification. What seems to be the apparent elimination of a single step has major implications. In these conditions the purification/labeling scheme can be easily automated using one of the available modular labs

for PET synthesis (e.g. Modular-Lab PharmTracer, Eckert and Ziegler, Germany), or it could easily be accomplished in a nuclear medicine hot-lab in a hospital.

4.5 Conclusions.

A Gallium specific lyophilized kit for ^{68}Ga-MAA production was created. The kit is comprised of a vial containing MAA (re-lyophilized DraxImage® Kit), a ^{68}Ga purification system and working solutions in the following syringes: 5 mL of 0.1 M HCl (elution), 1 mL 0.1 of M HCl (cleaning), 1 mL of 5 M HCl (purification), 1 mL of Millipore Water (extraction) and 0.3 mL of 3 N NaAc solution (buffer). Labeling at 75 ºC for 15 minutes is recommended for labeling yields higher than 95% with no further purification necessary. Room temperature labeling is possible for producing 80% labeling yield, but post-labeling purification is needed. The *in vivo* stability of the obtained ^{68}Ga-MAA drug product is superior to that of ^{99m}Tc-MAA. Use of ^{68}Ga-MAA in RMT planning is potentially possible and likely to benefit from superior imaging/quantification and more accurate dosimetric calculations.

CHAPTER 5 ^{99m}Tc Labeled Microspheres

5.1 Abstract

Chitosan Glycol (CHSg) and poly(glycerol-citric-dodecanediooate) (PGCD) microspheres are labeled with ^{99m}Tc as an alternative for MAA in perfusion SPECT studies. Microspheres are created and characterized. Labeling study and *in vitro* radiochemical stability were performed. Particle degradation in PBS buffer was also performed over 48 hours. A feasible particle size distribution of ≈30±10 μm was obtained for both compositions. High *in vitro* radiochemical purity was found for the labeled particles in the 4 hours study. Particle degradation was 24 hours for PGCD and 48 hours for CHSg in PBS buffer. Labeled microspheres were injected into Sprague Dawley Rats and biodistribution was determined after 2 and 4 hours. Both ^{99m}Tc-PGCD and ^{99m}Tc-CHSg were quickly allocated in the lungs after injection. PGCD microspheres degraded at a fast rate and most of the injected ^{99m}Tc activity was released from the lungs after 1 hour. CHSg microspheres were proven useful for lung perfusion studies with 91 % and 83 % of the injected activity remaining in the lungs after 2 and 4 hours respectively.

5.2 Introduction

Since 1974 the use of ^{99m}Tc-MAA (macroaggregated albumin) has been established as the gold standard for lung perfusion studies (73). The availability of a MAA lyophilized kit (73) and the ^{99}Mo/^{99m}Tc radioisotopic generator (74) facilitated the use of ^{99m}Tc-MAA as a lung perfusion agent. As discussed previously, orientation of macroaggregates (seldom spherical) in the blood flow becomes important to determine “effective size”, making it difficult to predict the *in vivo* behavior. Aggregate degeneration is another component making the size distribution variable and unreliable (43). The ideal (theoretical) perfusion particle should be spherical (size not to be dependent on particle orientation) with a practical size distribution of 30±10 μm. Polymeric

spherical microparticles with narrow size distributions have been previously obtained (75). As stated before, RMT planning will most likely benefit from particles with shape and size distribution similar to that of the therapy microspheres. It will also decrease the risk of disease transmission due to human derived materials (MAA).

Many of the available biocompatible polymers have been labeled with ^{99m}Tc. Some examples are ^{99m}Tc-PLGA (poly(DL-lactide-co-glycolide)) nanoparticles (76), ^{99m}Tc-PLA (poly lactic acid) (77) and ^{99m}Tc-CHS (Chitosan) (78) among others. PLGA and PLA have known long (months) degradation times. CHS has been found to have an *in vitro* half-life greater than 21 days (79). This characteristic is relatively undesired when performing lung perfusion studies or for RMT planning, as the particles need to degrade fast (maximum 48 hour half-life) and restore blood flow.

There are some alternatives of CHS in the market with both high and low solubility in water (80). Solubility of the polymer is directly related to particle degradation half-life. There is a compromise in the ideal particle degradation: it has to be slow enough to allow allocation in the lungs and imaging, but fast enough to clear the vessels and restore blood flow afterwards (half-life 12-48 hours). One of the best candidates is found in Chitosan Glycol (CHSg), with only 2 mg/ml solubility in water, well characterized and commercially available (Sigma-Aldrich, CHSg ≥60%). Degradation can be manipulated using glutaraldehyde as crosslinking agent. Another potential polymer for microparticle preparation is our "in-house" poly(glycerol-citric-dodecanediooate) (PGCD), since it degrades fast by hydrolysis and all the possible degradation products are biocompatible. Also, the speed of degradation can be manipulated by changing the C/D ratio, the greater the ratio, the faster it degrades.

5.3 Materials and Methods

5.3.1 Particle Preparation and Characterization

Chitosan glycol (Sigma-Aldrich, USA) particles were prepared using water in oil (w/o) emulsion technique. One ml of CHSg solution (2% w/v solution in 2% v/v Acetic Acid) was added drop wise to a round bottom flask containing an egg shaped magnetic stirrer, 20 ml of Toluene and 100 µl of Tween® 80 (surfactant). Stirring rate was set at 1150 rpm (Corning-Cole Palmer, USA). The emulsion was stabilized for 15 minutes and 100 µl of glutaraldehyde (25 % in water, FisherSci, USA) was added. Stirring was continued for another 105 minutes. Later, toluene was decanted. Particles were washed three times with 200-proof ethanol (Sigma-Aldrich, USA) and lyophilized (Lyophilizer). PGCD was dissolved in 1 ml dichloromethane and added dropwise to a round bottom flask containing 20 ml of 0.5 Pluronic (F-127, BASF, Germany) solution stir at 850 rpm (Corning-Cole Palmer, USA). The emulsion was stirred for 2 hours until total evaporation of the CH_2Cl_2. Obtained particles were washed 3 times with water and lyophilized (Lab-Conco, USA). Size distribution, concentration and particle morphology were obtained with a hemacytometer (Reichert, USA) using an optical microscope (Micromaster, FisherSci, USA).

5.3.2 ^{99m}Tc-PGCD and ^{99m}Tc-CHSg labeling and stability

$Na^{99m}TcO_4$ was obtained from a local pharmacy (Triad Isotopes, Miami, USA). One mCi was used to label approximately 100,000 particles in a 15 ml centrifuge vial containing the lyophilized particles after addition of 100 µl of 1 mg/ml $SnCl_2$ stock solution (Sigma-Aldrich, USA). Labeling was performed during 30 minutes at 25 ºC and 750 rpm in a Thermomixer (Eppendorf, Germany). Particles were centrifuged, decanted from the supernatant and both measured for labeling yield.

Labeled particles (n=4) were resuspended in reconstituted (1% w/v) bovine hemoglobin lysate (FisherSci, USA). Particles were stirred for 4 hours at 37 ºC in a thermomixer (Eppendorf, Germany). Every hour the particles were centrifuged, decanted and measured together with the supernatant to assess radiochemical purity.

Unlabeled particles were suspended in PBS buffer (pH≈7) and incubated at 37 °Celsius for a period of 48 hours. Samples were taken at 4, 12, 24 and 48 hours, gravity filtered through a 20 µm nylon filter [Spectrumlabs, USA], recovered and counted in a hemacytometer to establish the remaining concentration. Decay profiles are shown in figure 22 demonstrating the potential for CHSg and PGCD for RMT planning (imaging). Therefore, these particles were further evaluated *in vivo* for lung perfusion studies. Thus, preliminary experiments were performed to evaluate *in vivo* degradation of CHSg in mouse (ND4 Swiss Webster, Harlan, USA)

Lyophilized CHSg microparticles were re-suspended in carbonate buffer (pH=9.34). NHS-Fluorescein (Thermo Scientific, USA) was dissolved in Dimethyl Sulfoxide (DMSO, Thermo Scientific, USA) with a concentration of 10 mg/ml. A total 1 mg of NHS-Fluorescein (100 µl of the stock solution) was added to the vial containing the particles and stirred for 2 hours (Fig 33). At the end of the reaction particles were centrifuged, washed three times with water and finally lyophilized (Lyophilized CHSg-Fluorescein).

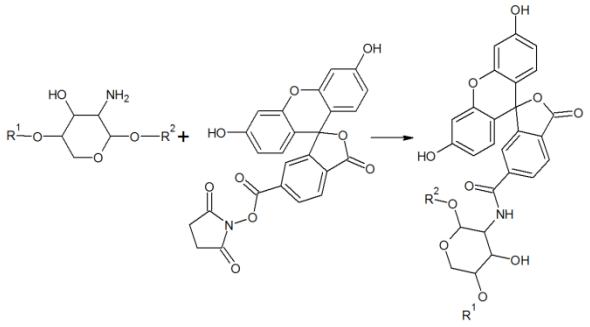

Fig 33 CHSg + NHS-Fluorescein reaction

For these preliminary experiments in mice, particles were re-suspended in saline solution for injection (FisherSci, USA) and ≈5000 particles were injected to each animal in the lateral tail vein. Animals were euthanized at 12 and 24 hours (n=2 per time point). Before extraction of the lungs, the trachea was isolated and a V cut was made. A syringe containing Optimal Cutting Temperature (OCT, Tissue-Tek, USA) liquid was inserted in the trachea and the lungs were filled with 0.5 ml. Lungs were finally extracted and frozen in a plastic mold filled with OCT and dipped in cyclopentane cooled to -80 ºC with dry ice. Specimens were obtained by cryosectioning the frozen samples in a Microtome (Leica, Japan). Sections were analyzed in a florescent microscope (Olympus IX81 with a Q Imaging Retiga 1300 Camera, USA).

5.3.3 Lung Perfusion Experiments

Animals (Sprague Dawley rats 200-225 grams, 2 per time point, Harlan, USA) were weighed before the procedure and anesthetized using an Ohmeda Isotec 3 isolfurane vaporizer (GE Healthcare, USA). Animals were restrained in the supine position (completely anesthetized) and a torso X-Ray was obtained (Belmont Acuray 071A, USA). Later, 100 µL of the labeled ^{99m}Tc-PGCD or ^{99m}Tc-CHSg (8,000-10,000 particles) with an activity ranging from 1.85-3.7 MBq (50 to 100 µCi) was injected through the lateral tail vein. Animals were euthanized at 2 or 4 hours. For both time points lungs, liver, spleen, heart, kidneys, ribs and 0.2 ml of blood and urine were collected, weighed and measured for activity using a Cobra 5000 well counter (Packard, USA). Non-collimated autoradiography images (in the unaltered supine position the X-Ray was obtained) were also taken at 1, 2, 3 and 4 hours (Packard Phosphorimager, Perkin Elmer, USA). In one group ^{68}Ga was injected as a control. Additionally, imaging and organ collection were also performed with ^{99m}Tc-MAA and free ^{99m}Tc for comparison purposes. ^{99m}Tc-MAA was purchased from a local pharmacy (Triad Isotopes®, USA). Pertechnetate (obtained as Sodium Pertechnetate from Triad Isotopes, USA) was reduced with 100 µg of Stannous Chloride (Sigma-Aldrich, USA)

before injection. The obtained X-Rays and the autoradiography images were superimposed to provide anatomical and functional data.

5.4 Results and Discussion

5.4.1 Particle Preparation and Characterization

The emulsion method used created spherical particles with a size distribution of approximately 30±10 µm (figure 2).

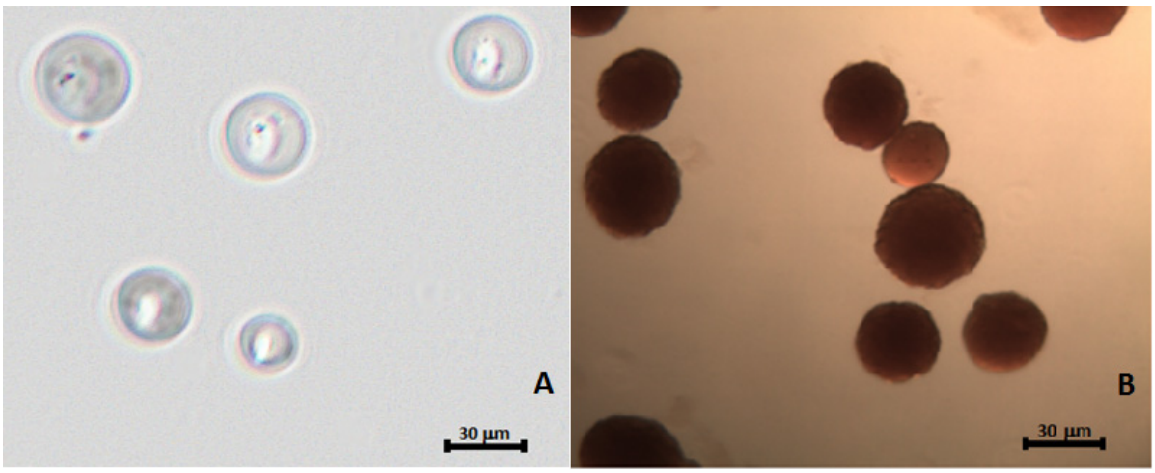

Fig 34 Obtained particles A: PGCD and B: CHSg.

Lyophilization and labeling of the particles did not affect their size and morphology. Chitosan microparticles swelled 20-25% when placed in contact with water, a feature that was taken into consideration when producing these particles (Fig 35). The produced PGCD microparticles needed to be filtered through a 20 µm nylon filter (Spectra/Mesh, Cole Palmer, USA) to assure proper distribution (Fig 35).

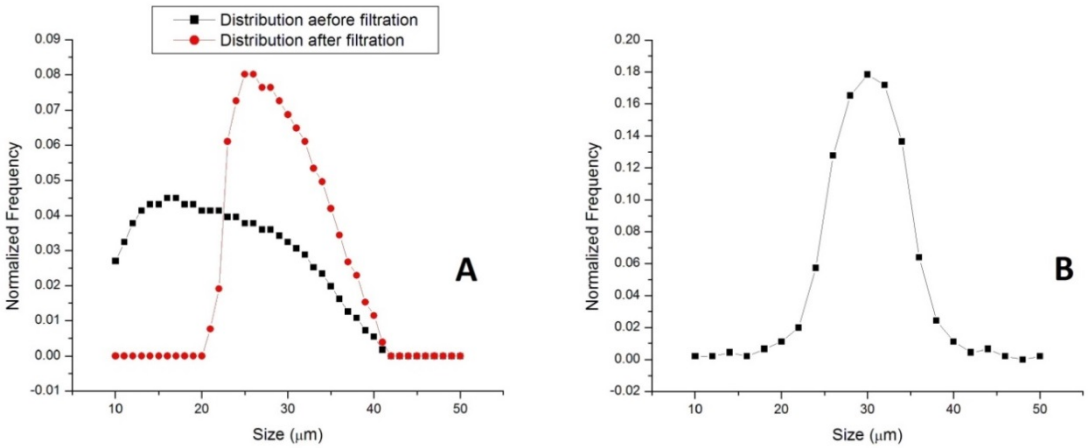

Fig 35 Size distribution for: A: PGCD size distribution before and after filtration and B: CHSg size distribution in saline solution.

5.4.2 ^{99m}Tc-PGCD and ^{99m}Tc-CHSg Labeling and stability

Particles were labeled obtaining 87.5±4.1 % and 94.7±0.2 % labeling for PGCD and CHSg respectively (Fig 36). PGCD microspheres showed better *in vitro* stability with over 97 % radiochemical purity at all times during the 4 hour study. CHSg microparticles quickly decreased the radiochemical purity to 82% remaining fairly constant afterwards (80% after 4 hours) (Fig 36).

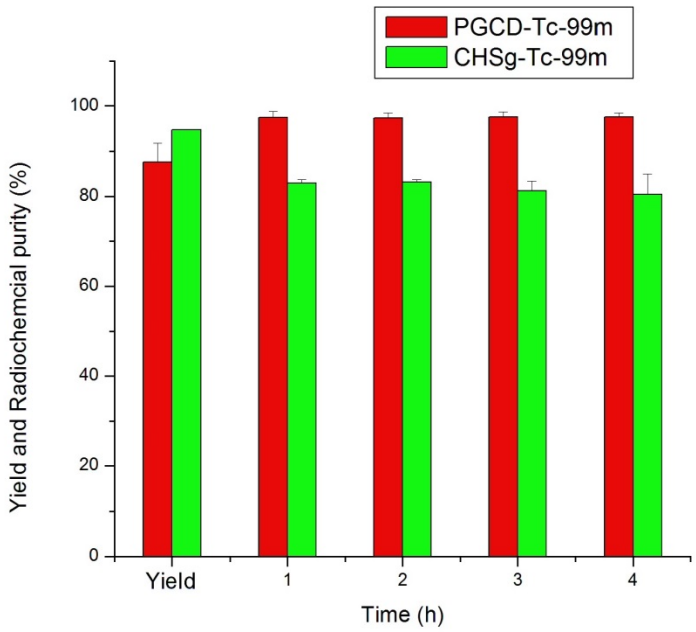

Fig 36 Labeling yield and *in vitro* radiochemical purity of ^{99m}Tc-CHSg and ^{99m}Tc-PGCD.

Even though the *in vitro* radiochemical purity of ^{99m}Tc-CHSg decreased rapidly to 80% after labeling, the particles were tested in animal experiments. Lung perfusion studies are performed with particles allocating in the vessels and the vessel occlusion locally reduces the fluid in contact with the particles increasing the chances of a successful image. Because of the high labeling yield obtained for ^{99m}Tc-CHSg (96.1±0.3 %) the particles did not need post-labeling purification. The 87.5% labeling yield obtained for the PGCD microspheres was high enough for imaging studies but post-labeling purification is required. This was performed by centrifuging the particles (1000 rcf, 30 seconds) and removing the supernatant using a 5" spinal needle. Particles were later resuspended in saline for injection.

Microsphere *in vitro* degradation showed an approximated half-life of 24 hours for PGCD and 48 hours for CHSg (Fig 37). Chitosan (CHS) is shown as a control since its degradation is known to be longer. *In vivo* degradation (for both CHSg and PGCD microparticles) is expected to be faster.

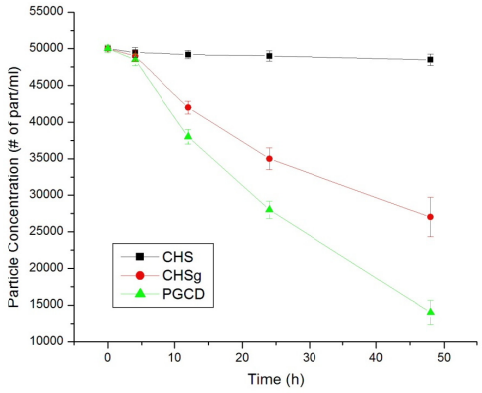

Fig 37 Microparticles degradation profile in PBS at 37 ºC

The percent of NHS fluorescein attached to the particle surface was not determined, since it was added only for particle detection purposes. However, images were obtained to qualitatively assess the attachment (Fig 38).

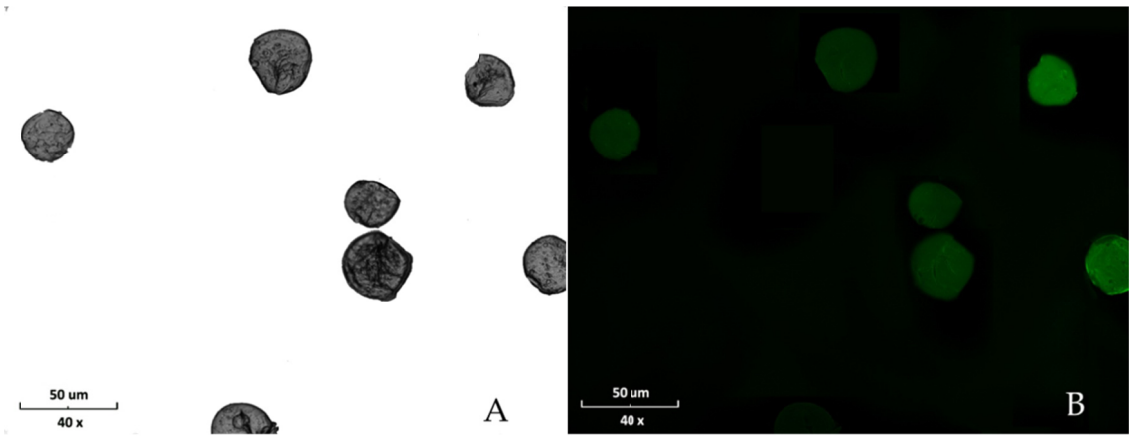

Fig 38 CHSg-Fluorescein Particles. A: Bright Field and B: Fluorescent Image

Particles were observed after 12 hours in the lung sections, however little or no particles were observed in the 24 hour sections (Fig 39). The experiment provided qualitative information of the particles degradation. Since observed degradation was fast, earlier time points and a larger

number of images were necessary to quantify the particles half-life. Extended lung crysectioning experiments were performed and are described in Chapter 6.

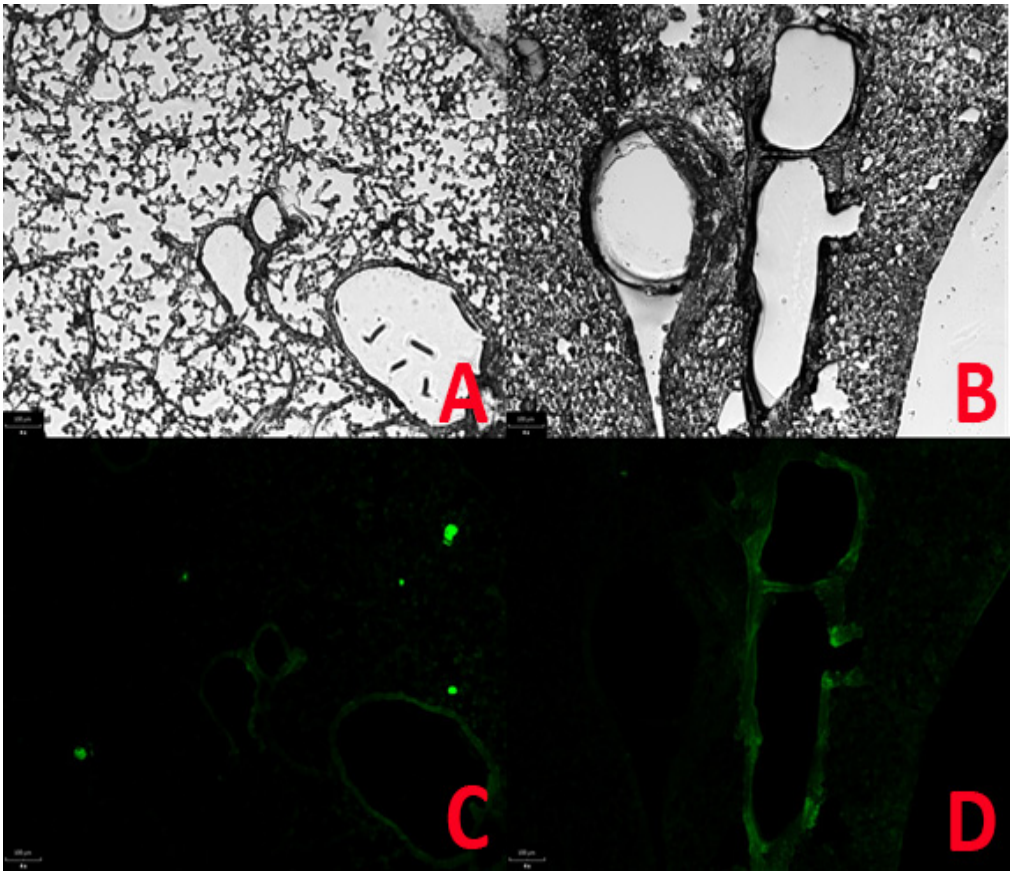

Fig 39 Cryosection Images. A and C: bright field and fluorescence images of a 12 hour sample; B and D: bright field and fluorescence images of a 24 hour sample.

5.4.3 Lung Perfusion Experiments

Following tail vein injection, most of the injected ^{99m}Tc-CHSg activity was allocated in the lungs within the first 30 seconds (checked with Geiger counter, Victoreen ASM-990, Fluke, USA). After 2 hours 91.6±6.5% of the injected activity (decay corrected) was allocated in the lungs (Cobra 5000 well counter, Packard, USA). After 4 hours 83.2±4.1% was still found in the lungs (Fig 40).

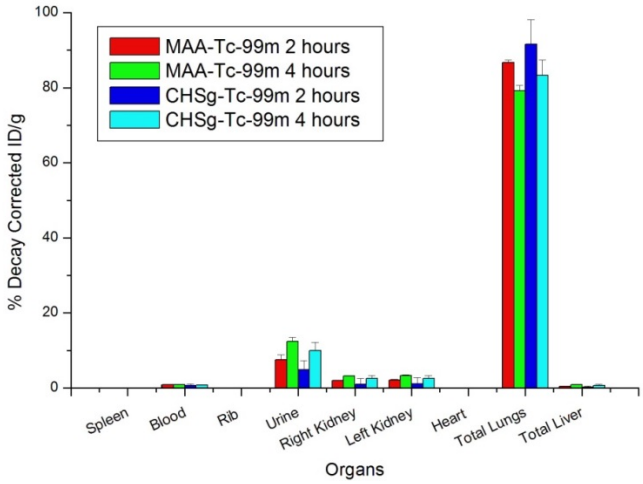

Fig 40 Decay Corrected Biodistribution of ^{99m}Tc-CHSg compared to ^{99m}Tc-MAA

The activity released from the lungs was almost exclusively excreted to the urine accounting for 4.9±2.5% and 10.0±2.1% decay corrected injected dose per gram (DC-ID/g) after 2 hours and 4 hours respectively. Less than 3% DC-ID/g was detected in all the other organs at any given time point (Fig 40). Lung perfusion images were obtained at several time points confirming the preferential lung allocation (Fig 41). Lung perfusion performance of the ^{99m}Tc-CHSg particles is slightly better than that of ^{99m}Tc-MAA.

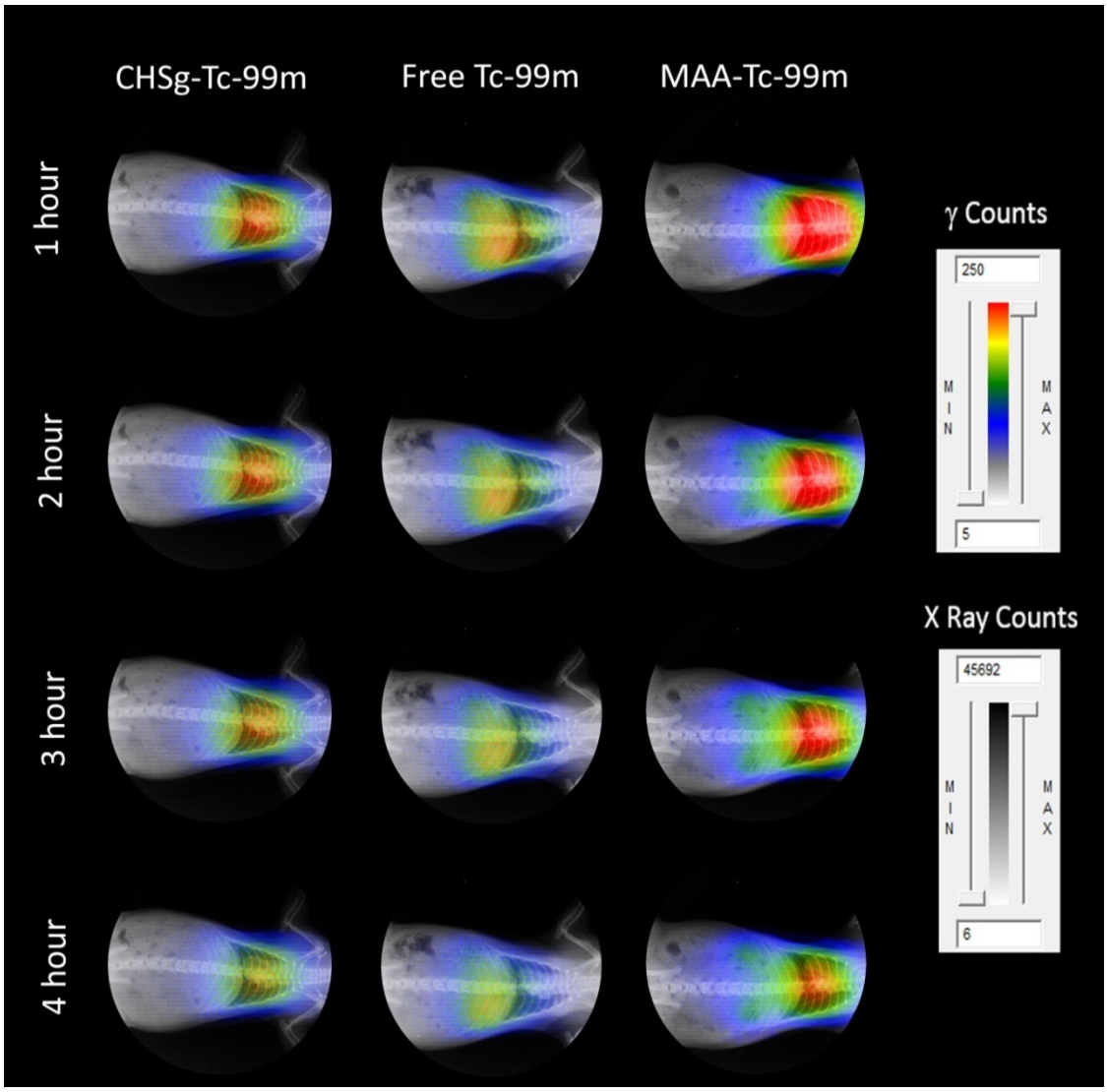

Fig 41 Un-collimated, non-decay-corrected full body X-Ray/Autoradiography of ^{99m}Tc-CHSg, ^{99m}Tc-MAA and free ^{99m}Tc.

Injected ^{99m}Tc-PGCD was also allocated in the lungs within the first 30 seconds (checked with Geiger counter, Victoreen ASM-990, Fluke, USA), and confirmed with a 10 minutes image (Fig 43). However, the 2 and 4 hour biodistribution (Fig 42) shows strong degradation of these particles.

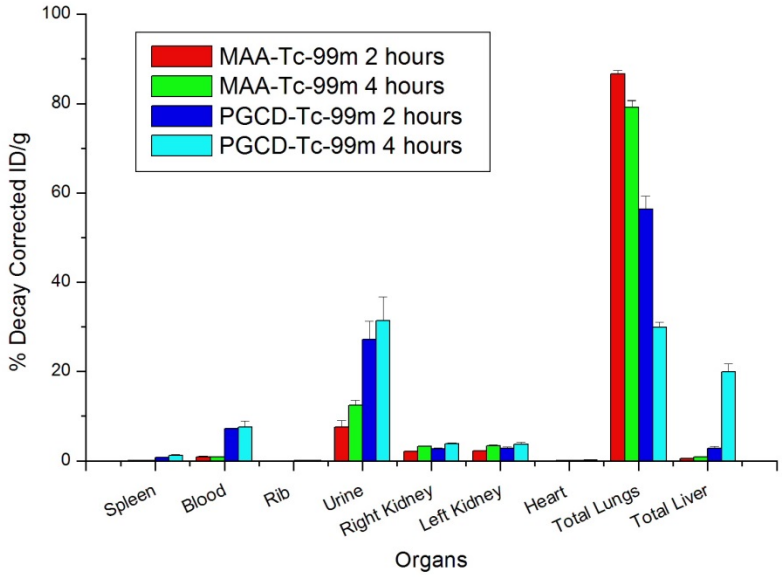

Fig 42 Decay Corrected Biodistribution of ^{99m}Tc-PGCD Biodistribution compared to ^{99m}Tc-MAA

A significant 56.4±2.9% DC-ID/g was found in the lungs after 2 hours, decreasing to 29.9±1.1% DC-ID/g after 4 hours (Fig 42). The behavior of ^{99m}Tc when injected free and as ^{99m}Tc-PGCD is fairly different. The first ^{99m}Tc-PGCD degradation products are eliminated to the bladder (27.1±4.1% DC-ID/g after 2 hours, increasing to 31.4±5.3 % DC-ID/g at 4 hours). Contrary to free ^{99m}Tc (44.6±2.8 % DC-ID/g in liver after 2 hours), only 2.8±0.5 % DC-ID/g is found in the liver after 2 hours. However the liver allocation is increased to 19.8±1.9 DC-ID/g after 4 hours. The blood concentration did not vary during the study (7.3±0.1 and 7.6±1.2 % DC-ID/g after 2 and 4 hours). The *in vivo* biodistribution of ^{99m}Tc-PGCD was similar to that of ^{99m}Tc-MAA but with a much faster degradation and larger liver allocation after 4 hours.

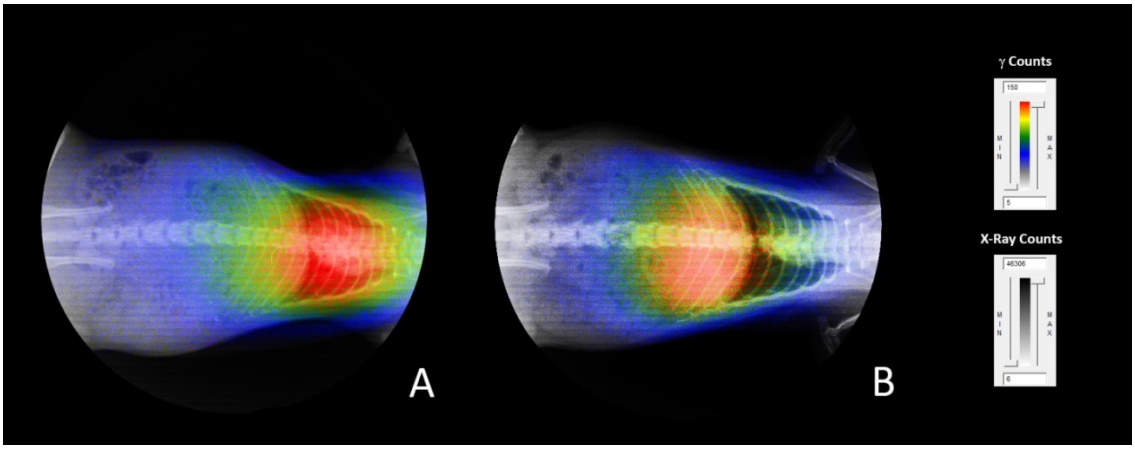

Fig 43 Un-collimated, non-decay-corrected full body X-Ray/Autoradiography of A: ^{99m}Tc-PGCD compared to B: free ^{99m}Tc after 10 minutes.

Even when strong lung allocation is observed in the 10 minutes image, some free ^{99m}Tc is already observed in the blood stream at this time point (Fig 43). Nevertheless, ^{99m}Tc-PGCD remains a potential perfusion agent, however more experiments varying the D:C ratio in the polymer are needed. The greater the D:C ratio, the more hydrophobic the polymer. However, with a greater the D:C ratio the polymer becomes more positively charged decreasing the labeling yield for radiometals. Therefore, in order to have proper degradation half-life and maximize labeling yield, the D:C ratio needs to be optimized.

5.5 Conclusions

Microspheres within the desired 30±10 μm size range were successfully obtained for PGCD and CHSg. Labeling was performed with >90% yield and *in vitro* radiochemical stability after 4 hours. Particle *in vitro* degradation half-life in PBS showed a faster degradation speed for PGCD (half-life ≈ 24 h) compared to that of CHSg (half-life ≈ 48 h). *In vivo* studies with ^{99m}Tc-PGCD labeled microspheres show strong initial allocation in the lungs, however fast degradation of PGCD was observed releasing ^{99m}Tc into the blood stream. Much better results were found for ^{99m}Tc-CHSg labeled microparticles. Two hours post injection 91.6±6.5% of the injected activity

(decay corrected) was allocated to the lungs with 83.2±4.1% after 4 hours. It can be concluded that ^{99m}Tc-CHSg is a feasible microsphere lung perfusion agent that has the potential to be used as surrogate during RMT planning.

CHAPTER 6 ^{68}Ga Labeled Microspheres

6.1 Abstract

Fast biodegradable microspheres (12 h < half-life < 48 h) labeled with a positron emitter are needed for PET lung perfusion and RMT planning. An emulsion method was used to create 30±10 μm size range microspheres with biodegradable polymers (PGCD and CHSg). The surface of CHSg microspheres was modified with NOTA for higher *in vivo* stability. ^{68}Ga labeling of all the microspheres was performed with >90% yield and *in vitro* radiochemical stability after 4 hours. Particle *in vitro* degradation half-life in porcine plasma showed a fast <30 minutes half-life for PGCD and approximately 24 hours for CHSg and CHSg-NOTA. *In vivo* studies with 68Ga-PGCD labeled microspheres show fast release of ^{68}Ga. Similar results were found for the ^{68}Ga-CHSg labeled microparticles demonstrating the need for surface decoration of CHSg micropsheres with p-SCN-Bn-NOTA. For the obtained ^{68}Ga-NOTA-CHSg microspheres, lung allocation was very high with 98.9±0.2 % and 95.6±0.9 % after 2 and 4 hours respectively. Even when remarkable lung allocation was obtained another important result is that the addition of p-SCN-Bn-NOTA acts as a radioprotectant quickly eliminating the released activity from the lungs to the bladder.

6.2 Introduction

The greatest limitation of RMT is the impossibility of quantifying the dosimetry during the treatment planning. This is due to the fact that the ^{99m}Tc-MAA scintigraphy is a single photon emission tomography technique (SPECT) and the difficulty in obtaining proper attenuation correction as compared to positron emission tomography (PET). The RMT planning will be greatly benefited by the inclusion of a positron emitter radioisotope; since absolute attenuation correction and potentially superior resolution is present in PET. Important advances were made in early years by labeling the Pulmolite MAA kit with ^{68}Ga (61), obtaining an 80 % labeling yield

and purity > 95% for. The advantages of spherical microspheres for perfusion studies, with a practical size distribution of 30±10 μm have been discussed extensively in previous chapters (Chapter 1, 2 and 5). There is a need for fast biodegradable (12 h < half-life < 48 h) microspheres that can be labeled with a PET isotope for proper RMT planning.

6.3 Materials and Methods

6.3.1 Particle Preparation and Surface Modification

PGCD (75:25 and 50:50 D:C ratio) was prepared similarly to that used for ^{99m}Tc labeling. Approximately 150 μg were dissolved in 1 ml dichloromethane and added drop wise to a flask containing 20 ml of 0.5 Pluronic (F-127, BASF, Germany) solution while stirring at 850 rpm (Corning-Cole Palmer, USA). The emulsion was stirred for 2 hours until total evaporation of the CH2Cl2. Obtained particles were washed 3 times with water, filtered through a 20 μm filter (Spectra/Mesh, Cole Palmer, USA) and lyophilized (Lab-Conco, USA).

Chitosan glycol (Sigma-Aldrich, USA) was dissolved in a 2% w/v, 2% v/v acetic acid solution. Microspheres were prepared in a w/o emulsion adding dropwise 1 ml of CHSg stock solution to a flask containing 20 ml of Toluene and 100 μl of Tween® 80 (surfactant) while stirring at 1150 rpm. After 15 minutes 100 μl of glutaraldehyde (25 % in water, FisherSci, USA) was added. After 2 hours (total time since CHSg stock solution was added) toluene was decanted, and spheres were washed three times with 200-proof ethanol (Sigma-Aldrich, USA) and lyophilized (Lyophilizer). Size distribution, concentration and particle morphology were obtained with a hemacytometer (Reichert, USA) using an optical microscope (Micromaster, FisherSci, USA).

A stock solution of p-SCN-Bn-NOTA (Macrocyclics, USA) with concentration 1 mg/ml in Na_2HCO_3/NaH_2CO_3 (pH 9.3-9.4, Sigma-Aldrich, USA), was prepared. Microspheres were resuspended in 1 ml of the p-SCN-Bn-NOTA Stock solution. The suspension was stirred at room

temperature for 4, 12, 24 and 48 hours (n=3 per time point) to form the NOTA-CHSg particles (81). The reaction yield was evaluated using a UV/Visible spectrophotometer (Varian/Agilent Technologies, Switzerland) at the 224 nm absorption peak of the p-SCN-Bn-NOTA (Fig 44).

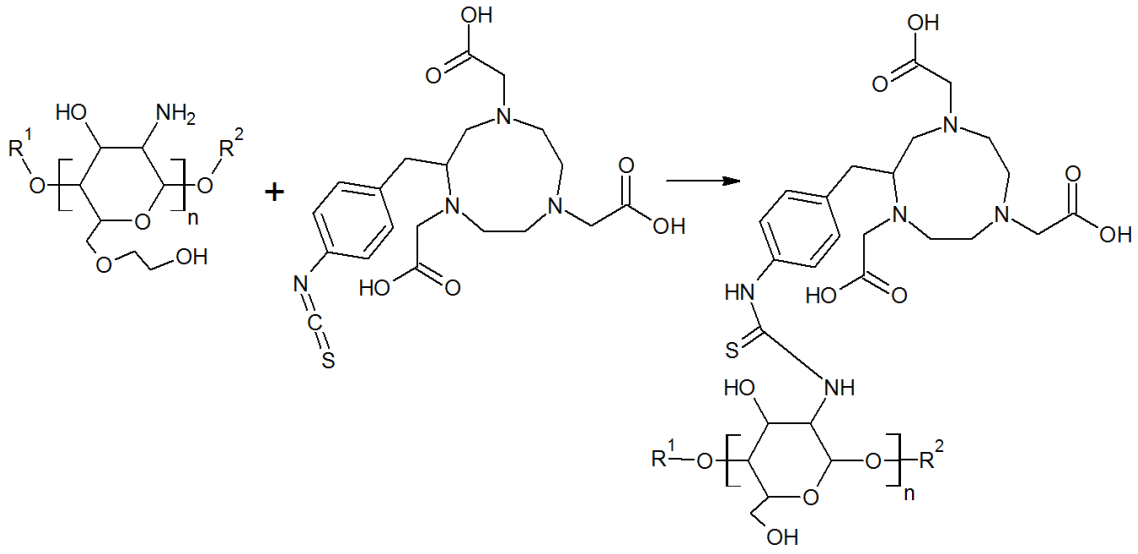

Fig 44 Surface decoration of CHSg microparticles with p-SCN-Bn-NOTA

6.3.2 ^{68}Ga Labeling and CHSg Microspheres Degradation

Labeling of ^{68}Ga-NOTA-CHSg (pH=4), ^{68}Ga-CHSg (pH=5.5) and ^{68}Ga-PGCD (pH=5.5) was performed at room temperature in acetate buffer. A labeling kinetics study was done using four different reaction times: 5, 10, 15 and 60 minutes. *In vitro* radiochemical stability studies were performed in PBS buffer (pH=7) measuring the activity of centrifuged particles (Eppendorf, Germany) and the supernatant in a dose calibrator (Biodex, USA) at 1, 2, 3 and 4 hours after resuspension.

For the *in vitro* degradation studies of the particles porcine blood was obtained from Mataderos Cabrera (Miami, USA), and centrifuged at 3000 rcf for 30 minutes. Plasma was later decanted and used for microsphere degradation experiments. Lyophilized CHSg, NOTA-CHSg and PGCD (both 50:50 and 75:25 D:C ratio) microspheres were resuspended in the plasma. CHSg and

NOTA-CHSg microspheres samples were extracted at 1, 2, 4, 12, 24, 48 and 72 hours. PGCD microspheres were also extracted but at 5, 10, 30 and 60 minutes. All samples (n=3 per time point) were analyzed for size distribution and particle concentration using a hemacytometer (Reichert, USA) and an optical microscope (Micromaster, FisherSci, USA).

For in vivo particle degradation studies, lyophilized CHSg microparticles were re-suspended in carbonate buffer (pH=9.34). NHS-Fluorescein (Thermo Scientific, USA) was dissolved in Dimethyl Sulfoxide (DMSO, Thermo Scientific, USA) with a concentration of 10 mg/ml. A total 1 mg of NHS-Fluorescein (100 µl of the stock solution) was added to the vial containing the particles and stirred for 2 hours (Fig 33). At the end of the reaction particles were centrifuged, washed three times with water and finally lyophilized (Lyophilized CHSg-Fluorescein).

The mouse experiments described above were used to optimize the cryosectioning experiments in rats. Particles were re-suspended in saline solution for injection (FisherSci, USA) and ≈10000 particles were injected to each Sprague Dawley Rat (200-225 grams, Harlan, USA) in the lateral tail vein. Animals were euthanized at 2, 6, 12 and 24 hours (n=2 per time point). Before extraction of the lungs, the trachea was isolated and a V cut was made. A syringe containing Optimal Cutting Temperature (OCT, Tissue-Tek, USA) cryoembedding media was inserted in the trachea and the lungs were filled with 2 ml. Lungs were finally extracted and frozen in a plastic mold filled with OCT and dipped in liquid nitrogen. Specimens were obtained by cryosectioning the frozen samples (14 µm slices) in a Microtome (Leica, Japan). Lung cryo-specimens (4 lung sections per animal) were analyzed with a florescence microscope (Olympus IX81 with a Q Imaging Retiga 1300 Camera, USA). The entire area of each specimen was imaged using a 4x objective. Obtained images were analyzed using in-house software and particles were measured and counted.

6.3.3 Lung Perfusion Experiments

Sprague Dawley rats (2 per time point, Harlan, USA) were purchased and weighed (200-225 grams). Animals were anesthetized using an Ohmeda Isotec 3 isolfurane vaporizer (GE Healthcare, USA). After surgical plane anesthesia was reached, animals were restrained in the supine position. A torso X-Ray was then obtained (Belmont Acuray 071A, USA). Immediately after, 100 µL of the labeled ^{68}Ga-PGCD, ^{68}Ga-CHSg or ^{68}Ga-NOTA-CHSg (8,000-10,000 particles) with a ^{68}Ga activity range going from 1.85 to 3.7 MBq (50 to 100 µCi) were injected through the lateral tail vein. Animals were euthanized at 2 or 4 hours. Lungs, liver, spleen, heart, kidneys, ribs and 0.2 ml of blood and urine were collected for either time point. Organs were weighed and measured for activity using a Cobra 5000 well counter (Packard, USA). Non-collimated autoradiography images (in the unaltered supine position the X-Ray was obtained) were also taken at 10 minutes for initial assessment and 1, 2, 3 and 4 hours (Packard Phosphorimager, Perkin Elmer, USA). In one group free ^{68}Ga was injected as a control. The obtained X-Rays and the autoradiography images were superimposed to provide anatomical and functional data.

6.4 Results and Discussion

6.4.1 Particle Preparation and Surface Modification

Over 95% of the obtained CHSg microspheres are in the 30±10 size range (Fig 35) and did not change after the 12 hour reaction with p-SCN-Bn-NOTA (Fig 45).

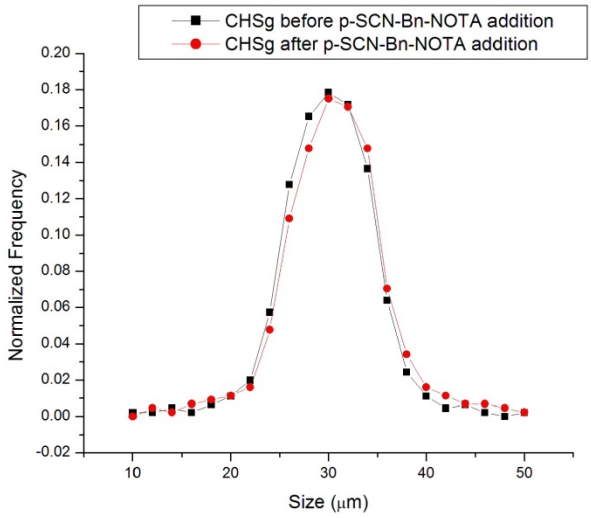

Fig 45 CHSg size distribution before and after p-SCN-Bn-NOTA surface decoration.

However size distribution and size concentration was mildly and severely altered for the 24 and 48 hours p-SCN-Bn-NOTA reactions respectively. Better p-SCN-Bn-NOTA attachment was obtained at these later time points compared to the 12 hours reaction, but it was due to rupture of the CHSg microspheres and exposure of new available free amine groups for the reaction (Fig 44).

Around 260±15 µg of p-SCN-Bn-NOTA (of the total 1 mg added) were covalently attached to the surface of the CHSg microspheres after 12 hours reaction. The net p-SCN-Bn-NOTA amount that bonded to the microspheres surface was increased to 297±25 and 347±40 µg after 24 and 48 hours of reaction. However, as stated before, particle degradation altered the final size distribution.

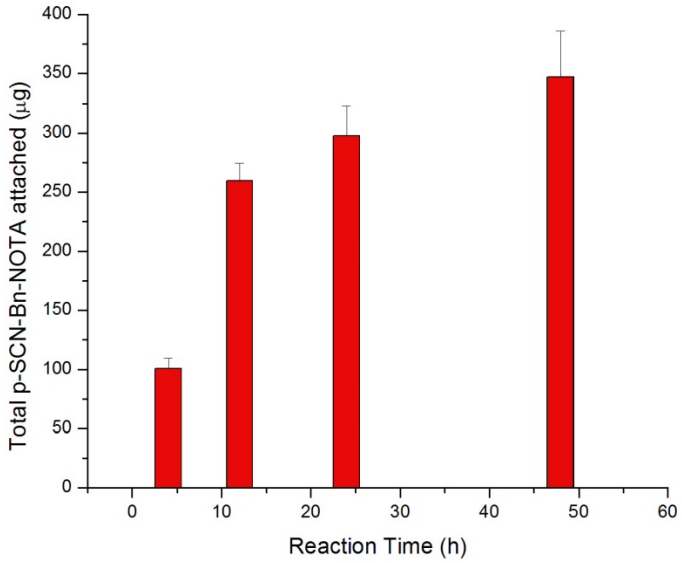

Fig 46 Surface decoration of CHSg with p-SCN-Bn-NOTA with different reaction times

Maximum reaction yield taking into consideration the totality of available NH_2 groups was slightly over 1%. Nevertheless it is a biased calculation since only a fraction of these groups are exposed for the p-SCN-Bn-NOTA reaction. Regardless of the yield, the addition of 260 micrograms of p-SCN-Bn-NOTA to the batch represents a theoretical loading capacity (assuming 95% labeling yield) of 12.8 μCi/particle (1.28 Ci for 100,000 particles). In molecular imaging only 3-5 mCi total are used, 3 order of magnitude less than the total available capacity.

6.4.2 ^{68}Ga Labeling and CHSg Microspheres Degradation

CHSg, PGCD and CHSg-NOTA microparticles were labeled with ^{68}Ga successfully with more than 90% yield at room temperature. Reaction kinetics placed the optimum reaction time at 15 minutes (Fig 47). Specific labeling yields after 15 minutes were 93±3 % for ^{68}Ga-PGCD, 96±3.5 % for ^{68}Ga-CHSg and 97±3 % for ^{68}Ga-NOTA-CHSg.

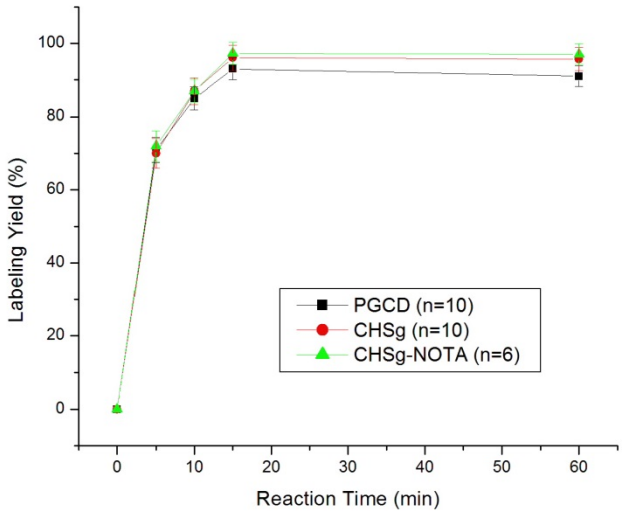

Fig 47 Reaction Kinetics for CHSg, PGCD and CHSg-NOTA with ^{68}Ga

Radiochemical stability was shown to be over 90 % after 4 hours of study at 37 ºC in saline, PBS buffer and 1% reconstituted bovine hemoglobin lysate. The particles conserved their shape and distribution during the labeling process and *in vitro* radiochemical stability studies.

Porcine plasma studies showed faster microsphere degradation than when they were in PBS buffer (see previous chapter) for all studied particles (Fig 48). PGCD degradation half-life was found to be around 24 hours in the PBS. However when placed in contact with plasma degradation is much faster. PGCD (50:50 D:C ratio) microparticles disappear from solution within 5 minutes of contact with plasma. The other PGCD composition (75:25 D:C ratio) showed increased stability in the plasma, though the half-life of these particles was found to be shorter than 30 minutes, disappearing completely after 1 hour. This degradation half-life might be considered too fast for both lung perfusion and RMT planning applications. However, because of the nature of the perfusion studies blood contact might be diminished when injected *in vivo* and half-life might be greater. For these reasons *in vivo* testing of these particles was not discarded.

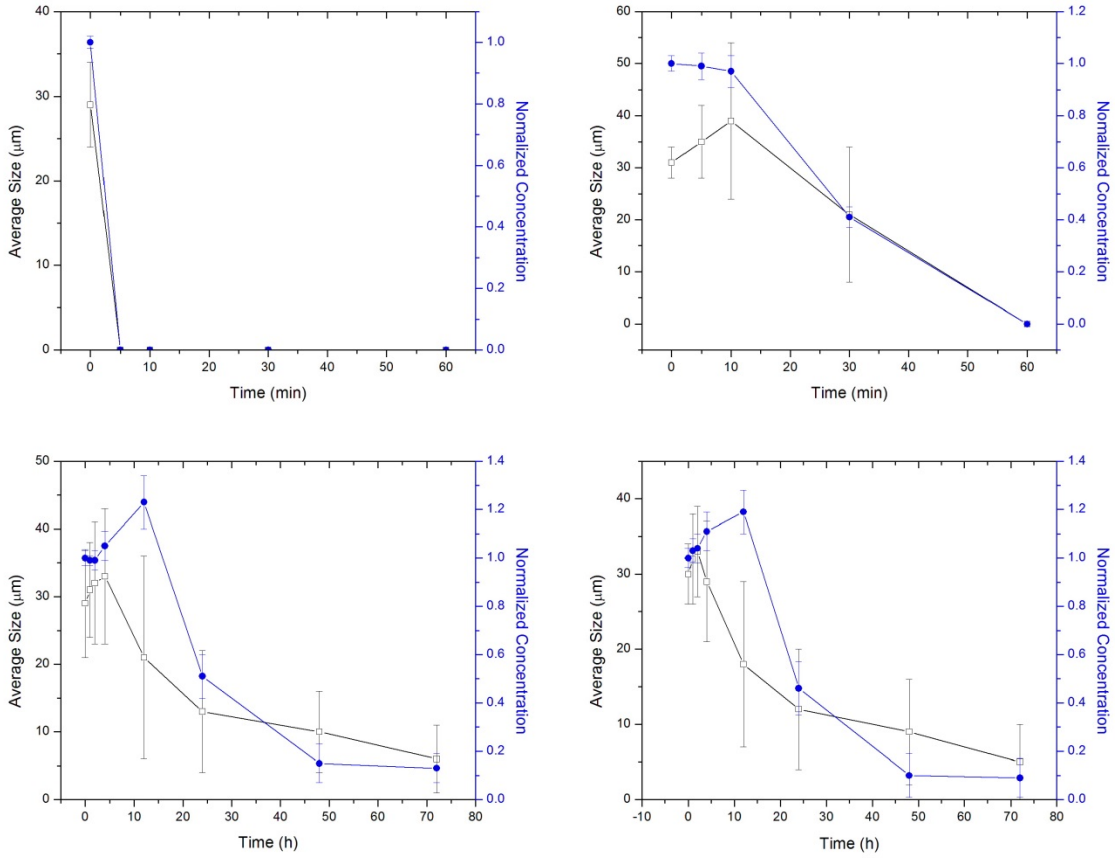

Fig 48 Porcine Plasma microsphere degradation studies for A: PGCD (50:50); B: PGCD (75:25); C: CHSg and D: CHSg-NOTA (n=3)

Equally to PGCD, CHSg (and CHSg-NOTA) *in vitro* degradation was faster than expected from the PBS buffer experiments. As can be seen in Fig 48, CHSg degradation undergoes a different process from that of PGCD. CHSg particles are first swollen in plasma (effect not observed in any PBS buffer degradation experiments) and then particle division into smaller pieces. The dramatic increase observed in particle concentration after 12 hours, together with the decrease in average particle size is due to the rupture of the original particles into smaller fractions. These fractions are later dissolved (degraded) disappearing gradually from the suspension. The observed half-life for both, CHSg and CHSg-NOTA, was found to be around 24 hours with no significant difference in their degradation profiles.

Particle degradation experiments performed *in vivo* show a similar degradation mechanism to that obtained *in vitro* (Fig 49).

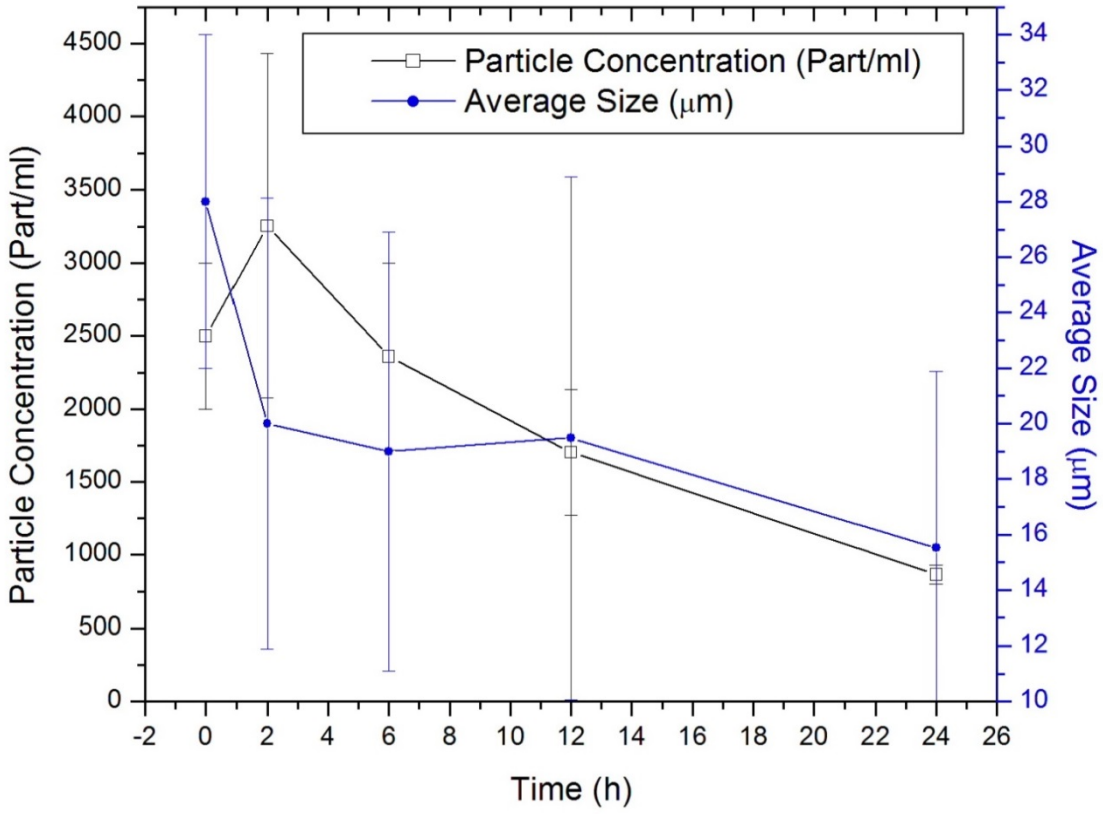

Fig 49 CHSg microspheres in vivo degradation studies (n=2 per time point)

Particle concentration is initially increased because of microsphere rupture. Smaller pieces are later slowly dissolved. This dissolution results in a steady decrease of the particles average diameter and also in particle concentration in the tissue (Fig 50). The in vivo half-life of the particles was determined to be 18-20 hours, since this the time when the particle concentration is reduced to half (50% of initial particle concentration).

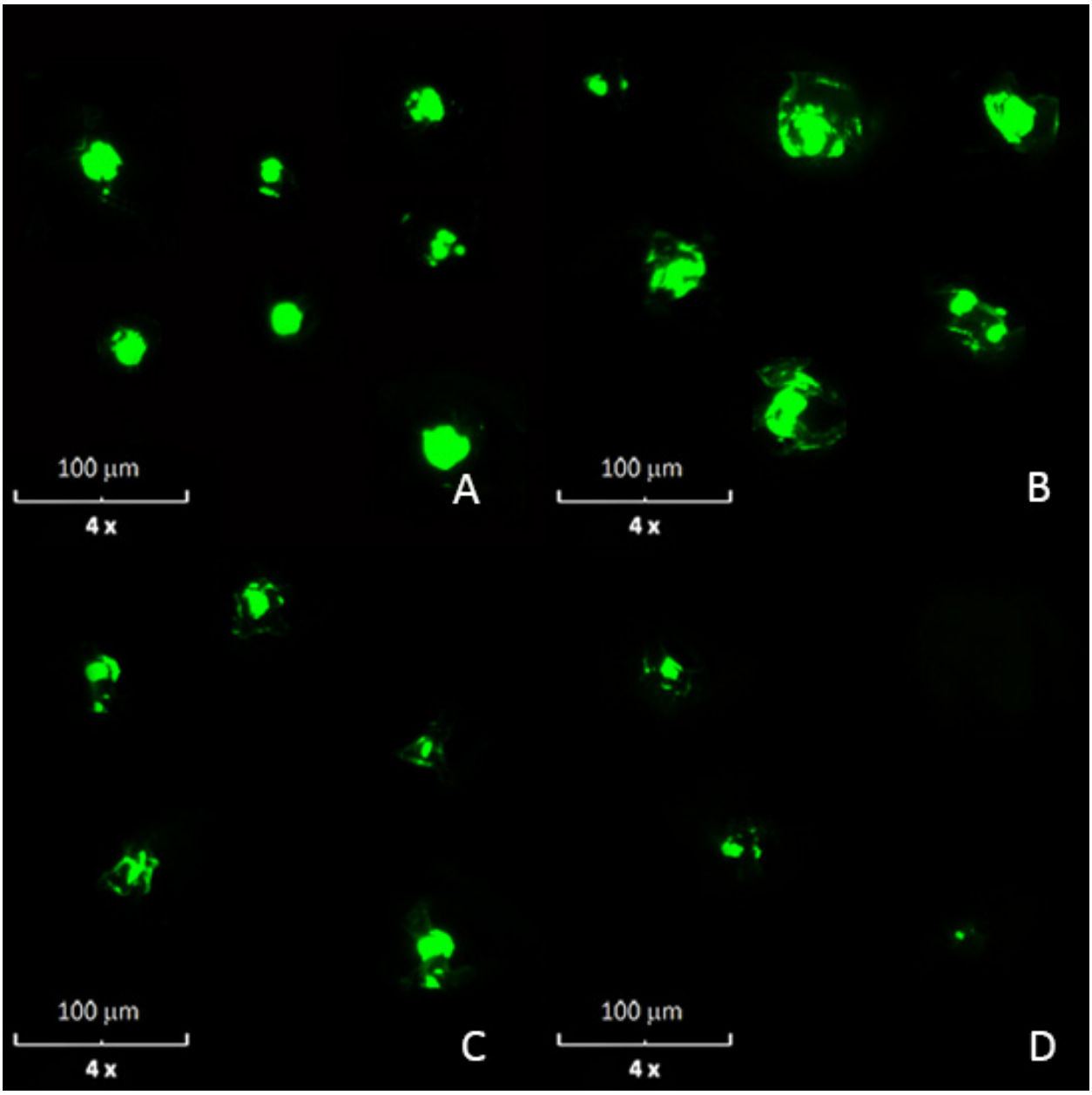

Fig 50 Representation of the in vivo CHSg microsphere degradation mechanism. Collage of representative microarticles found in the cryosections for different time points: A: 2 hours, B: 6 hours, C: 12 hours and D: 24 hours. Relative particle amount in the images is related to the real particle concentration found in the tissue sections.

Results obtained in the in vivo experiments are highly qualitative since many assumptions were made for the calculations of average size and concentration. Particles concentration was assumed to be homogeneous in the entire lung, and particles under 10 micrometers were not included in

the analysis since those should no longer occlude the vessels and therefore will not interfere with the later injection of the therapeutic particles in final the RMT phase.

Furthermore, the average size calculation is only an estimate due to the artifacts inherent to the sectioning method; there is no way to know if a particle that is sized represents the whole cross-section or only a part of the particle, the latter being more likely. Therefore, the particle size distribution is probably an underestimate of the true *in vivo* size distribution. Nevertheless, by 24 hours, comparatively few particles were observed in the sections. Also, no particle clumping was observed as the particles were found to be evenly distributed and thus a good estimation of particles half-life was obtained. The particle degradation half-life was found to be between 18 and 20 hours, which makes the CHSg microspheres a potential candidate for lung perfusion imaging and RMT planning.

6.4.3 Lung Perfusion Experiments

The first obtained image (10 minutes) after injection of ^{68}Ga-PGCD showed severe release of the radioisotope from the particles (compared to the 10 minutes image for ^{99m}Tc-PGCD, Fig 43). The ^{68}Ga-PGCD chelation was apparently weaker than that of the competing native transferrin (Fig 51).

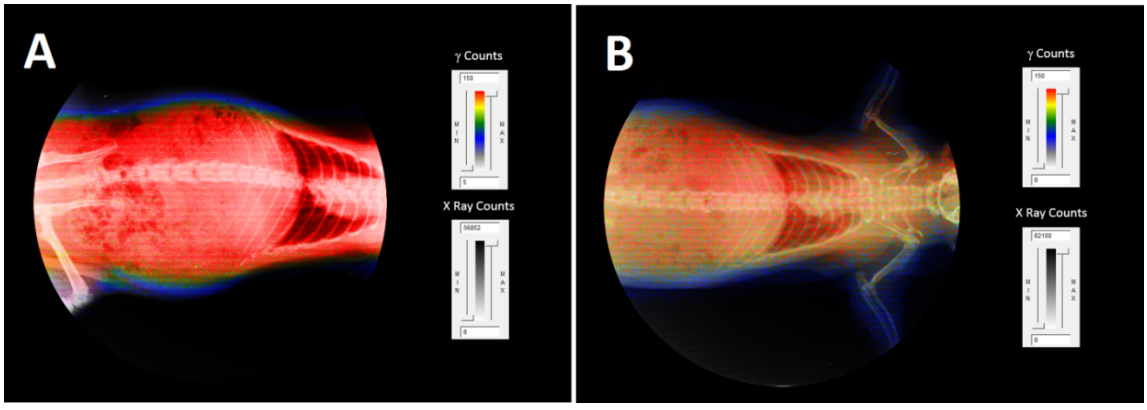

Fig 51 Comparison of images 10 minutes after injection for A: Free ^{68}Ga and B: ^{68}Ga-PGCD

However, despite the similarities organ collection at 2 hours showed a different picture (Fig 52). Only 49.0±3.3 % of the ^{68}Ga injected as ^{68}Ga-PGCD was found in the blood while 84.9±4.5 % was present in the blood for the free ^{68}Ga experiments. Equally different was the amount of tracer in the urine: 35.1±4.0 % for ^{68}Ga-PGCD versus 6.8±2.9 % for the free ^{68}Ga. These differences evidence a combination of trans-chelation (PGCD to native transferrin) and PGCD *in vivo* degradation. Small dissolved polar fragments with ^{68}Ga (probably some form of Gallium Citrate) are cleared quickly by the kidneys and moved to the bladder. Despite the evidence of some ^{68}Ga chelation strength by PGCD, it is not enough to perform lung perfusion imaging studies as shown in Fig 51. The fast released of ^{68}Ga to the blood significantly increases the body background and makes difficult to obtain lung perfusion images with diagnostic value.

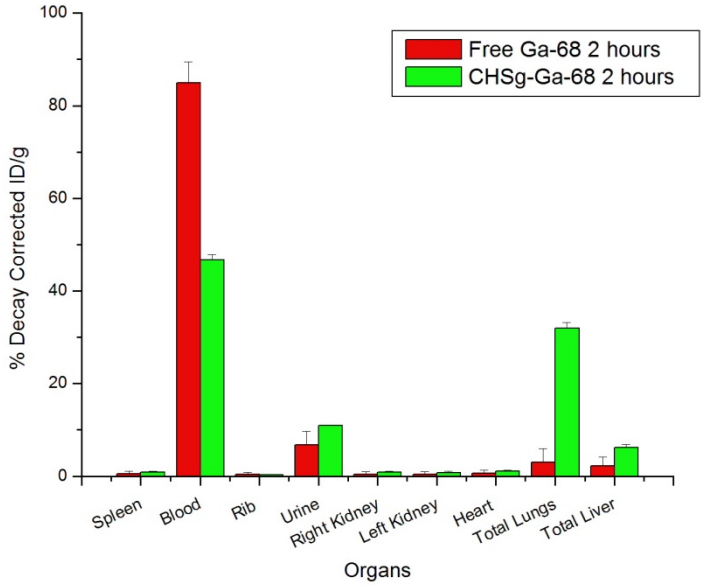

Fig 52 Decay corrected organ biodistribution after 2 hours for free ^{68}Ga and ^{68}Ga-PGCD.

Similar to ^{68}Ga-PGCD, and despite the excellent *in vitro* results obtained, ^{68}Ga-CHSg did not perform well as a lung perfusion imaging agent. Strong evidence of ^{68}Ga trans-chelation by native transferring was observed (Fig 53).

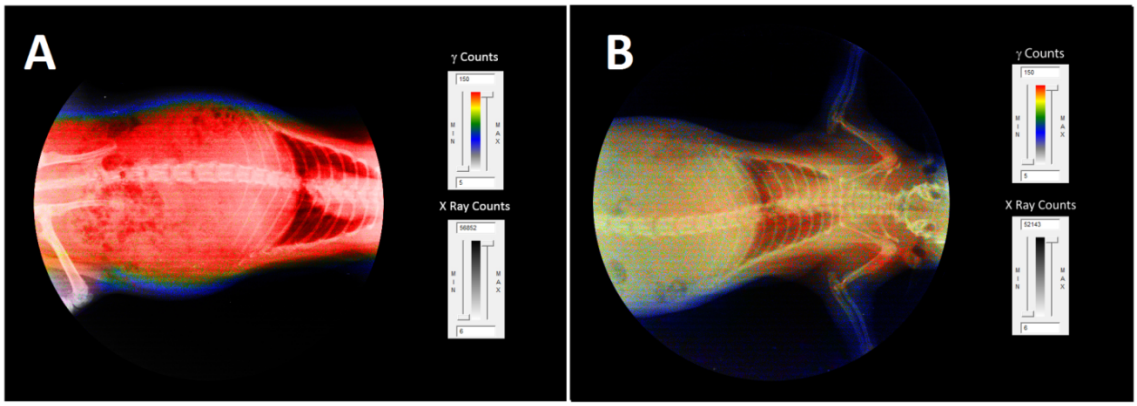

Fig 53 Comparison of images 10 minutes after injection for A: Free ^{68}Ga and B: ^{68}Ga-CHSg

Nevertheless, ^{68}Ga-CHSg *in vivo* behavior was notably different than that of free ^{68}Ga 2 hours post-injection (Fig 54).

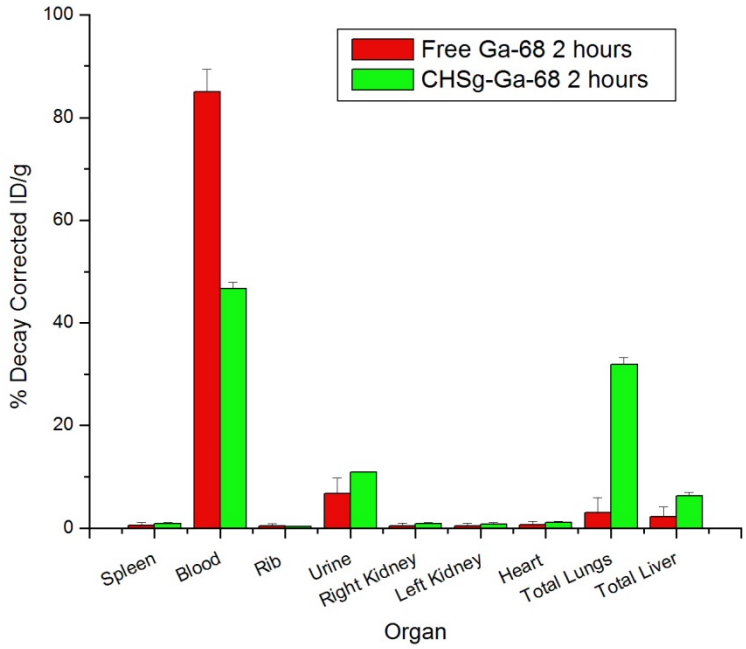

Fig 54 Organs biodistribution after 2 hours for free ^{68}Ga and ^{68}Ga-CHSg.

After 2 hours 31.9±1.3 % of the injected activity can be found in the lungs (compared to the 3.1±2.9 % found for the free ^{68}Ga) but 46.7±1.2 % was already released to the blood. The slow

degradation of CHSg (compared to PGCD) was expected. However the ^{68}Ga release to the blood was not expected since *in vitro* experiments were remarkable. Obtained result made necessary the surface decoration of the CHSg microspheres with a ^{68}Ga specific chelator (NOTA) to increase *in vivo* stability of the labeling.

Animal experiments performed with ^{68}Ga-NOTA-CHSg showed high lung allocation and stability during the 4 hour study (Fig 55).

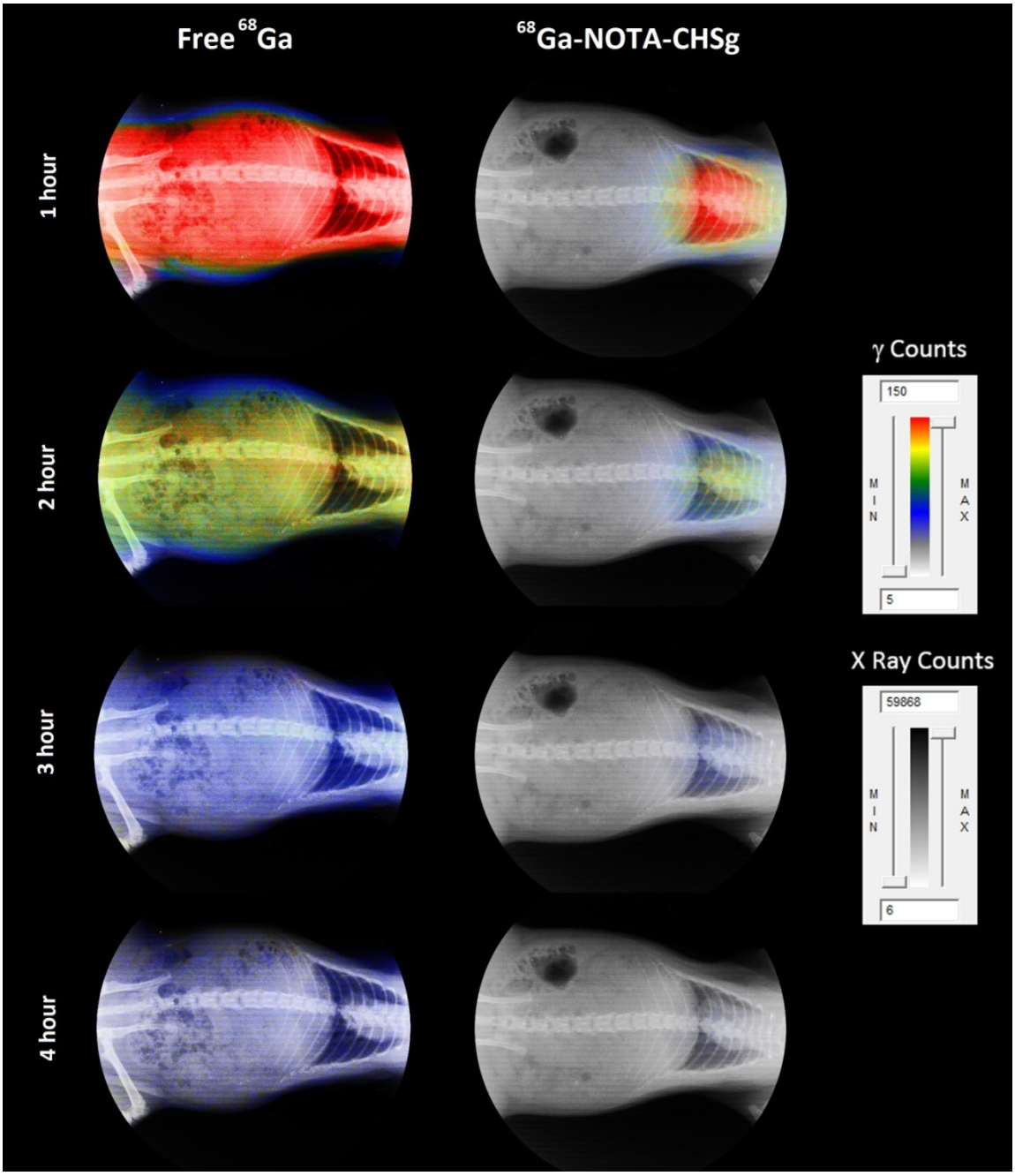

Fig 55 Non decay-corrected, un-collimated full body X-Ray/Autoradiography for free ^{68}Ga and ^{68}Ga-NOTA-CHSg at 1, 2, 3 and 4 hours.

From the images can be concluded that I vivo stability of the prepared ^{68}Ga-NOTA-CHSg is remarkable and the microspheres are a good candidate for lung perfusion imaging. However, organs were collected and measured for quantification at 2 and 4 hours (Fig 56).

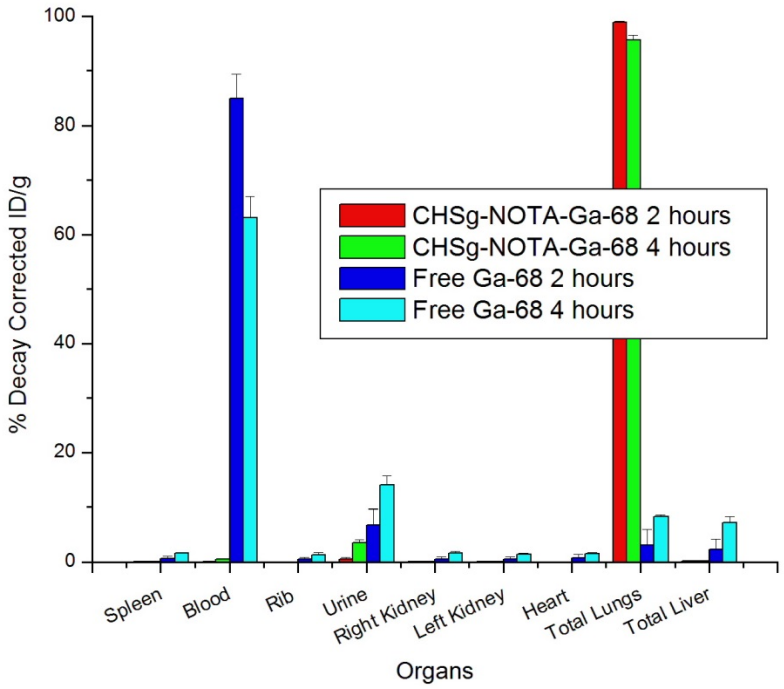

Fig 56 Decay Corrected Biodistribution of ^{68}Ga-NOTA-CHSg and Free ^{68}Ga at 2 and 4 hours.

After 2 hours 98.9±0.2 % of the injected activity of ^{68}Ga-NOTA-CHSg was found in the lungs, decreasing to 95.6±0.9 % after 4 hours. The activity released from the lungs moved directly to the bladder (3.5±0.6 % after 4 hours). The absence of activity in the blood (0.1±0.1 % at 2 hours and 0.5±0.1 % after 4 hours) evidenced the high radiochemical stability of the NOTA-^{68}Ga complex. The activity found in the urine must be due to early particle degradation releasing small polar fragments as frag-NOTA-^{68}Ga. The addition of the NOTA chelator to the surface of the particles also served as a radioprotectant to the rest of the organs, since less than one percent of the injected activity was found in the blood at any time. For the obtained perfusion agent imaging is recommended within the first hour post injection because of ^{68}Ga decay.

6.5 Conclusion

Microspheres within the desired 30±10 μm size range were successfully obtained for PGCD and CHSg. Surface modification of CHSg microspheres with NOTA for 12 hours did not affect the original size distribution or morphology. Addition of 260 micrograms of p-SCN-Bn-NOTA to the particles represents a theoretical loading capacity (assuming 95% labeling yield) of 12.8 μCi/particle. Labeling was performed for all compositions with >90% yield and *in vitro* radiochemical stability after 4 hours. Particle *in vitro* degradation half-life in porcine plasma showed a fast <30 minutes half-life for PGCD and approximately 24 hours for CHSg and CHSg-NOTA. *In vivo* studies with ^{68}Ga-PGCD labeled microspheres show fast release of ^{68}Ga. Similar results were found for the ^{68}Ga-CHSg labeled microparticles evidencing the need for surface decoration with p-SCN-Bn-NOTA. For the obtained ^{68}Ga-NOTA-CHSg lung allocation was very high with 98.9±0.2 % and 95.6±0.9 % after 2 and 4 hours respectively. Even when remarkable lung allocation was obtained another important result is that the addition of p-SCN-Bn-NOTA acts as a radioprotectant quickly eliminating the released activity from the lungs to the bladder.

CHAPTER 7 ^{90}Y Labeled Microspheres

7.1 Abstract

Chitosan (CHS) is used to prepare 30±10 µm size microspheres. Surface modification with p-SCN-Bn-DOTA was performed. A maximum ^{90}Y capacity was found to be 12.1 ± 4.4 µCi/particle. The best obtained labeling yield was 87.7±0.6 %. More than 90% *in vitro* stability was found. Particle *in vitro* degradation half-life in PBS was found to be greater than 21 days. *In vivo* studies with ^{90}Y-DOTA-CHS show more than 95 % of the injected activity (decay corrected) in the lungs after 24 hours. ^{90}Y-DOTA-CHS performance was superior to the commercially available SirTex microspheres. The addition of p-SCN-Bn-DOTA served as a radioprotectant for bone marrow. The 5 % ^{90}Y released from the lungs during the first 24 hours was quickly eliminated via urine.

7.2 Introduction

The available products in the market for Selective Internal Radiation Treatment (Fig 57) show several limitations. High specific gravity making injection challenging and null biodegradability are among them.

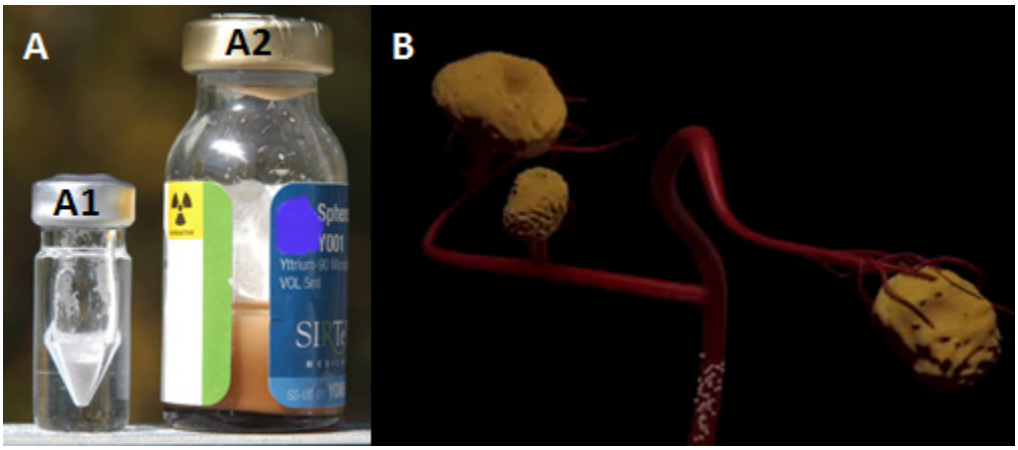

Fig 57 A: Commercially available products for RMT; A1: TheraSpheres, A2: SirSpheres and B: Representation of tumors being treated with ^{90}Y microspheres

For the TheraSpheres (also known as glass spheres), the relation between ^{90}Y activity and number of spheres can only be controlled by decay, since there is only one universal composition prepared. On the other side SirSpheres can be prepared with the desired ^{90}Y activity/number of spheres ratio, however the nature of ^{90}Y attachment is not specific (rather it is by ionic exchange absorption), increasing the risk of ^{90}Y release and bone marrow suppression.

RMT is almost always accompanied by chemotheraphy that is administered independently of the radiotherapeutic particles. Since these particles are non-biodegradable, chemotherapy entrapment and *in situ* release is not possible. Polymeric microparticles with high *in vivo* ^{90}Y radiochemical stability to protect bone marrow, and the capability to entrap chemotherapy drugs for simultaneous radio/chemotherapy are needed. The proper design of these particles will most likely improve the safety and effectiveness of the current RMT practice. Among the many materials available, a clear candidate for this application is Chitosan, a chitin derivate that has been extensively used for drug entrapment/release and has very low (if any) *in vitro* and *in vivo* toxicity (82).

7.3 Materials and Methods

7.3.1 Particle Preparation and Surface Modification

Chitosan (CHS, Sigma-Aldrich, USA) particles were prepared similar to the CHSg microspheres using a water in oil (w/o) emulsion technique. One ml of CHS solution (2.5 % w/v solution in 2% v/v acetic acid) was added drop wise to a round bottom flask and stirred (Corning-Cole Palmer, USA) at 1150 rpm. The flask contained 20 ml of Toluene (Acros Organics, USA) and 100 µl of Tween® 80 (surfactant, Sigma-Aldrich, USA). After 15 minutes 200 µl of glutaraldehyde (25 % in water, FisherSci, USA) was added and the emulsion was stirred for another 105 min. Toluene was finally decanted and particles were washed three times with 200-proof ethanol (Sigma-Aldrich, USA) and lyophilized (Lab-Conco, USA).

A 1 mg/ml solution of p-SCN-Bn-DOTA (Macrocyclics, USA, Fig 58) was prepared in Na_2HCO_3/NaH_2CO_3 buffer (Sigma-Aldrich, USA) with a pH 9.3-9.4. Particles were resuspended in 1 ml of the p-SCN-Bn-DOTA solution and stirred for 4, 12, 24 or 48 hours to form the DOTA-CHS particles. The reaction yield was evaluated using the p-SCN-Bn-DOTA absorption peak at 224 nm with a UV/Visible spectrophotometer (Varian/Agilent Technologies, Switzerland). All experiments were done in triplicate for all time points.

7.3.2 ^{90}Y Labeling and *in vitro* stability

A labeling study was performed at two different pH values: 5 and 7. The temperature influence on labeling was also studied using 25, 35 and 37 ºC. CHS microspheres and resin spheres (kindly provided by SirTEX, USA) were labeled for comparison in similar conditions. A 72 hours *in vitro* stability study using PBS buffer at pH 7 was performed to evaluate radiochemical purity. With ^{90}Y present to account for radiolytic effects CHS microspheres were studied for degradation over 21 days.

Using stable YCl_3 (Sigma-Aldrich, USA) as carrier for the radioactive $^{90}YCl_3$ (Perkin-Elmer, USA), a radioactive indicator experiment was performed to calculate the maximum ^{90}Y capacity of the prepared microspheres. Experiments were also performed with SirSpheres for comparison. For the *in vitro* work all activity measurements were made in an AtomLab 100 Dose Calibrator (Biodex, USA).

7.3.3 Lung Perfusion Experiments

Sprague Dawley rats (200-225 grams, 2 per time point, Harlan, USA) were anesthetized with an Ohmeda Isotec 3 isolfurane vaporizer (GE Healthcare, USA) after weighed. Once restrained in the supine position (completely anesthetized) and a torso X-Ray was obtained (Belmont Acuray 071A, USA). Immediately after, 100 µL (8,000-10,000 particles) of the labeled microspheres

(^{90}Y-DOTA-CHS and ^{90}Y-SirSpheres) with an activity ranging from 555-925 kBq (15 to 25 μCi) were injected through the lateral tail vein. Animals were imaged with non-collimated autoradiography (in the unaltered supine position the X-Ray was obtained) at 10 min, 12 and 24 hours post injection (Packard Phosphorimager, Perkin Elmer, USA). After the last image was obtained, animals were euthanized (24 hours post injection). For either time point their lungs, liver, spleen, heart, kidneys, ribs and 0.2 ml of blood and urine were collected, weighed and measured for activity using a Cobra 5000 well counter (Packard, USA). One group received free ^{90}Y as a control. The obtained X-Rays and the autoradiography images were superimposed to provide anatomical and functional data.

For the collected organs measurements, an activity vs. radiation counts linearity test (with known activity samples) was performed to the Cobra 5000 well counter (Packard, USA). A test tube (similar to the ones used in the organs) was filled with absorbent paper and soak in water to simulate auto absorption of the organs. Later, a known amount of ^{90}Y was deposited (ranging from 2 to 5 μCi, close to the activity range found in the organs) in the paper and measured (n=3 per activity point) in the well counter. Results were linear fitted and correlation coefficient was found. Spectra obtained for the lowest and highest activity points were also compared.

7.4 Results and Discussion

7.4.1 Particle Preparation and Surface Modification

The size distribution obtained for CHS particles was an average of 30.7±8.3 μm. After the preparation of the microspheres, the DOTA decoration reaction was performed (Fig 58).

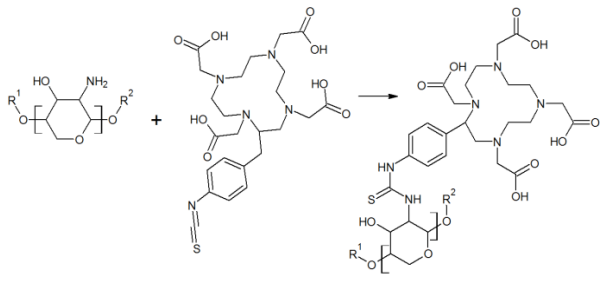

Fig 58 CHS - p-SCN-Bn-DOTA reaction.

The kinetic study for the reaction showed that saturation is reached at 12 hours (optimum reaction time), with no extra addition of p-SCN-Bn-DOTA in the subsequent time points. The total p-SCN-Bn-DOTA-CHS reaction yield is around 1% (with a maximum 250 μg of p-SCN-Bn-DOTA addition, similar to the result obtained for p-SCN-Bn-NOTA). The approximated 6.3 mg of CHS (total mass of 100,000 particles, 63 ng/particle) present in each preparation accounts for $2.33 \cdot 10^{19}$ available NH_2 groups in total. However, only a fraction of these groups are exposed to the microsphere surface and to further complicate the problem, the surface is not perfectly flat (Fig 63 A).

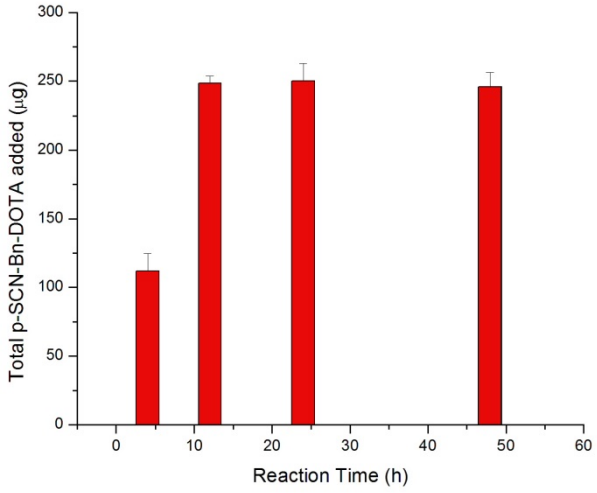

Fig 59 p-SCN-Bn-DOTA-CHS reaction kinetics

After the p-SCN-Bn-DOTA decoration a size distribution of 31.3±8.1 was obtained. As expected for CHS microspheres, there is no significant change in the distribution or particle morphology before and after the addition reaction (Fig 60). This is due to the high pH (9.4) in which the reaction is being held and the already low solubility and slow degradation rate of CHS.

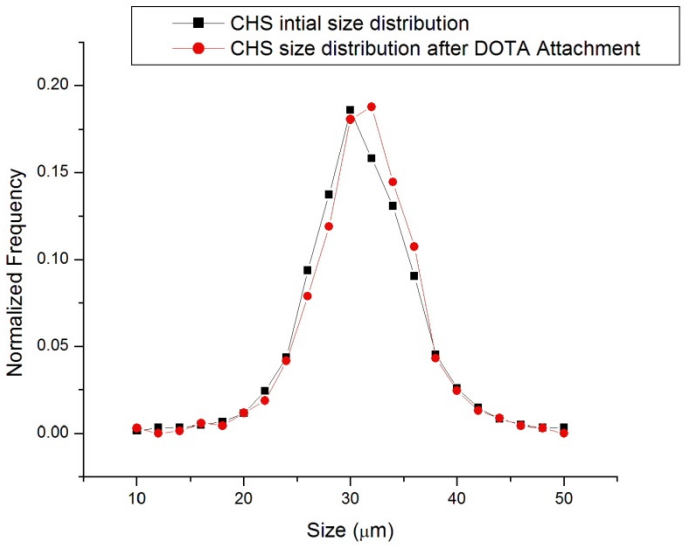

Fig 60 CHS microsphere size distribution before and after p-SCN-Bn-DOTA addition reaction.

7.4.2 ^{90}Y Labeling and *in vitro* stability

Maximum labeling yield for ^{90}Y-DOTA-CHS labeling was 87.7±0.6 %, obtained at pH=7 and 37 ºC (Fig 61) after 30 minutes. Yield was dependent on both pH and temperature (Fig 61). A rise in temperature might benefit the labeling, however CHS is a polysaccharide very sensitive to temperature and structural damages might occur. A longer labeling time did not increased the yield and 30 minutes was identified as the optimal labeling temperature. Labeling of resin spheres (SirTEX, USA) showed more than 98% yield in all conditions within 10 minutes of reaction. The

labeling was performed at pH=7 only since resin spheres are labeled and injected in water. Yield was not dependent on temperature for the studied range.

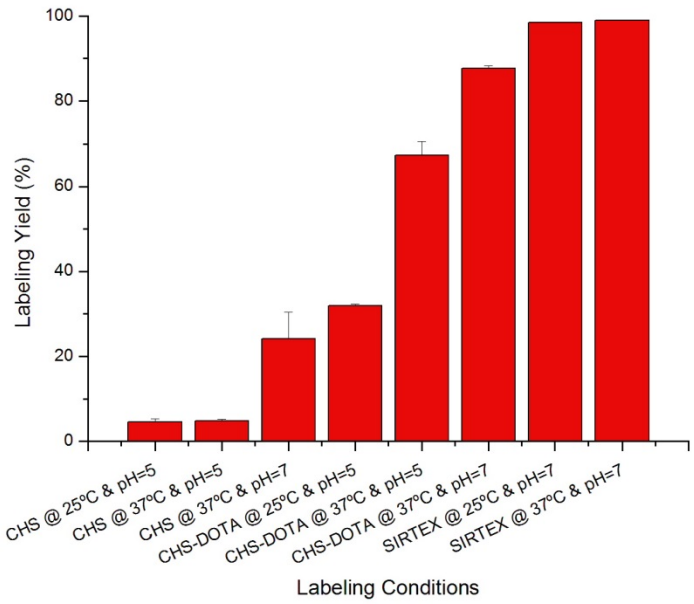

Fig 61 Labeling yields for ^{90}Y-CHS, ^{90}Y-DOTA-CHS and ^{90}Y-Resin at different pH values and temperatures.

Another interesting observation is that direct CHS labeling did not result in high yields. This result is in contradiction with a previously reported 99% yield (79). CHS used in these experiments (also 15 kDa molecular mass) was obtained from a different manufacturer (Polysciences, USA). Differences in results obtained with various chitosan batches and vendors have been reported in the past (83). This problem is solved by the addition of p-SCN-Bn-DOTA, rendering the labeling independent of the chitosan nature. However, differences in degradation and drug entrapment and release for other applications might be found and this problem needs to be investigated further.

The performed *in vitro* stability study showed over 90% radiochemical purity for ^{90}Y-DOTA-CHS after 72 hours compared to the 80% obtained for the resin spheres (Fig 62). Considering these positive result for ^{90}Y-DOTA-CHS, animal experiments were performed.

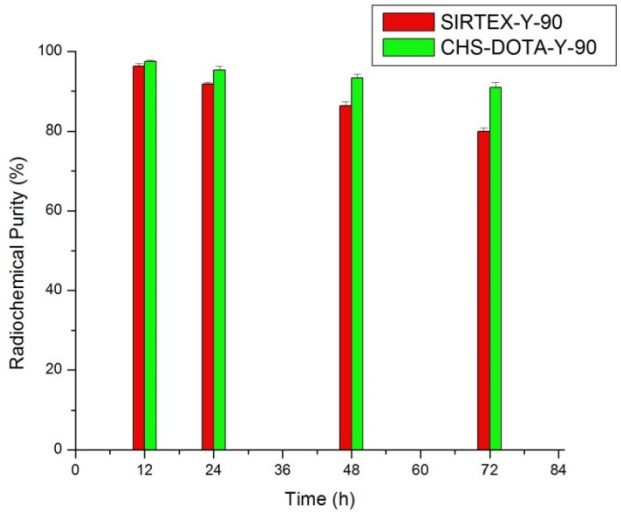

Fig 62 *in vitro* stability study for ^{90}Y-DOTA-CHS and ^{90}Y-SirSpheres.

The extended *in vitro* degradation of the particles showed that integrity was maintained, although with some surface degradation after 21 days (Fig 63). This timeframe was chosen since more than 95% of the ^{90}Y is physically decayed by 21 days. The obtained biodegradable microspheres demonstrated a long enough half-life to adequately perform RMT while allowing for ultimate clearance and blood flow restoration.

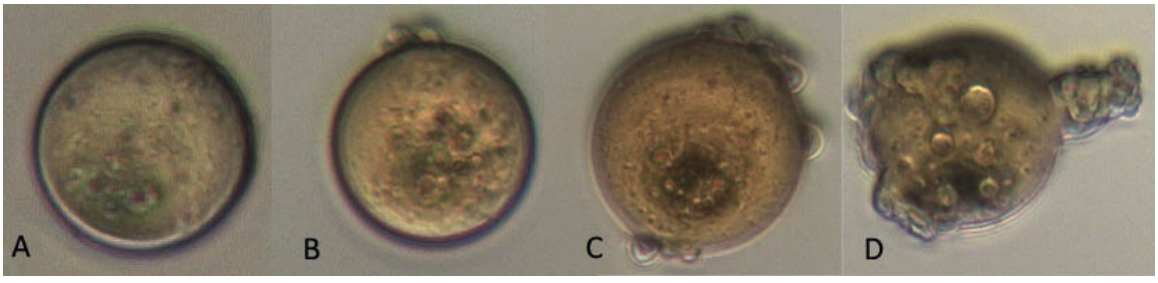

Fig 63 Degradation of CHS microspheres after A: 1 day, B: 7 days, C: 14 days and D: 21 days

Finally, the maximum labeling capacity for the CHS-p-SCN-Bn-DOTA microspheres was 12.1 ± 4.4 μCi/particle and for SirSpheres 111.7 ± 0.1 μCi /particle. Hence, in a regular treatment course using $3 \cdot 10^6$ to $30 \cdot 10^6$ particles, maximum possible activity load is 36-360 Ci and 335.1-3351 Ci for CHS-p-SCN-Bn-DOTA and SirSpheres respectively. These values are 3 orders of magnitude over the regular administered dose.

7.4.3 Lung Perfusion Experiments

Detector linearity response to activity and spectra distribution were performed as described. A high correlation coefficient was obtained in the studied range. Spectra comparison between the lowest and highest activity points revealed no difference.

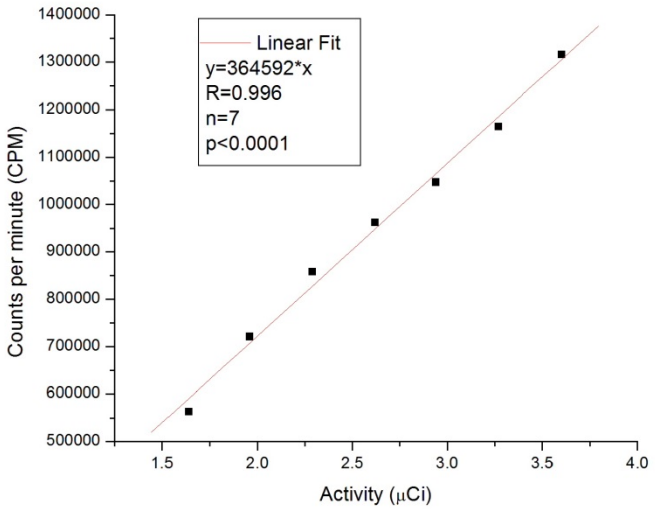

Fig 64 Cobra 5000 well counter (Packard, USA) efficiency and linearity calibration for ^{90}Y

The high specific gravity of the SirSpheres makes particles injection difficult since they deposit fast. An injection yield of only 15 % was reached (injected in water). The injection yield for the ^{90}Y-DOTA-CHS microspheres was over 50 % (injected in saline solution), very repeatable for all the other CHS and CHSg microspheres studied (Fig 65). The initial assessment of biodistribution

with a survey meter (Victoreen ASM-990, Fluke, USA) revealed a strong allocation in the lungs for the ^{90}Y-DOTA-CHS microspheres while the SirSpheres distribution did not differ from the free ^{90}Y.

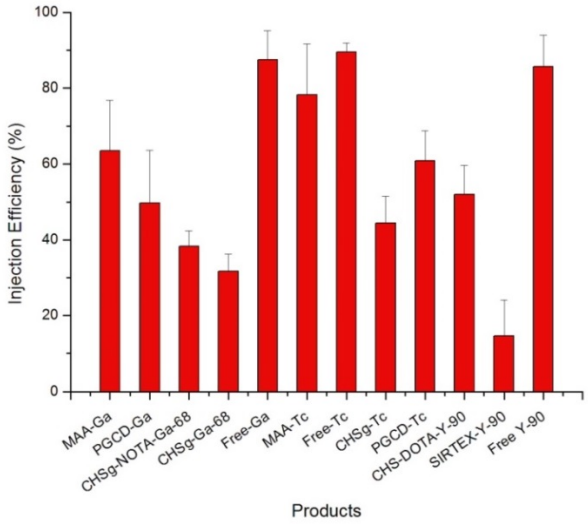

Fig 65 Injection efficiency for all the studied microparticles

Already in the 10 minutes strong ^{90}Y bone marrow allocation and similar distribution was observed in the autoradiography images for ^{90}Y-Resin and free ^{90}Y (Fig 67). However, collected organ quantification (Cobra 5000 well counter, Packard, USA) at 24 hours showed some lung allocation for ^{90}Y-Resin (Fig 66).

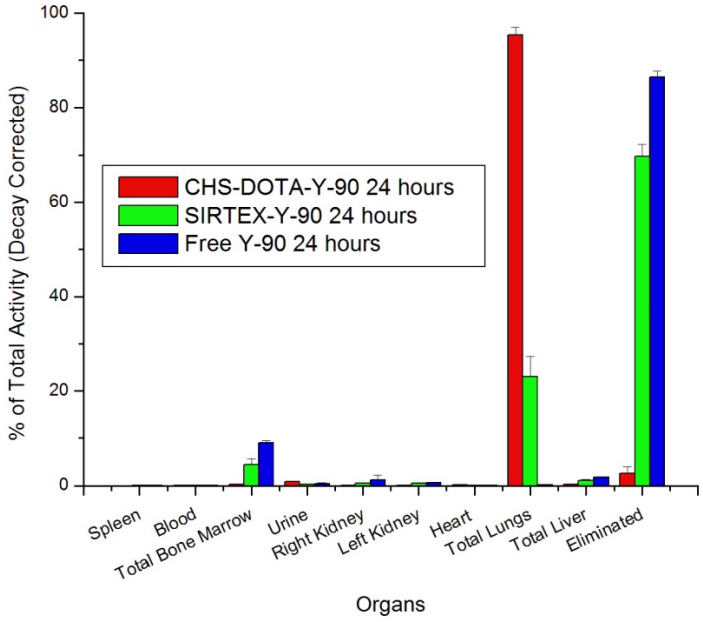

Fig 66 Decay Corrected Biodistribution of ^{90}Y-DOTA-CHS, ^{90}Y-Resin and free ^{90}Y

Lung allocation of more than 95 % (decay corrected) of the injected activity was detected for ^{90}Y-DOTA-CHS after 24 hours, showing a significant difference with the 23 % (decay corrected) found for the ^{90}Y-Resin. Free ^{90}Y was initially allocated in the bone marrow but only 9 % remained after 24 hours, the rest of the activity was eliminated via urine. Over 4% of the injected ^{90}Y-Resin activity was found in bone marrow after 24 hours and more than 70% was eliminated. In contrast to this result the activity released from the lungs in the ^{90}Y-DOTA-CHS experiments resulted in only a fraction of a percent being allocated to the bone marrow, and the remaining either in the urine or eliminated.

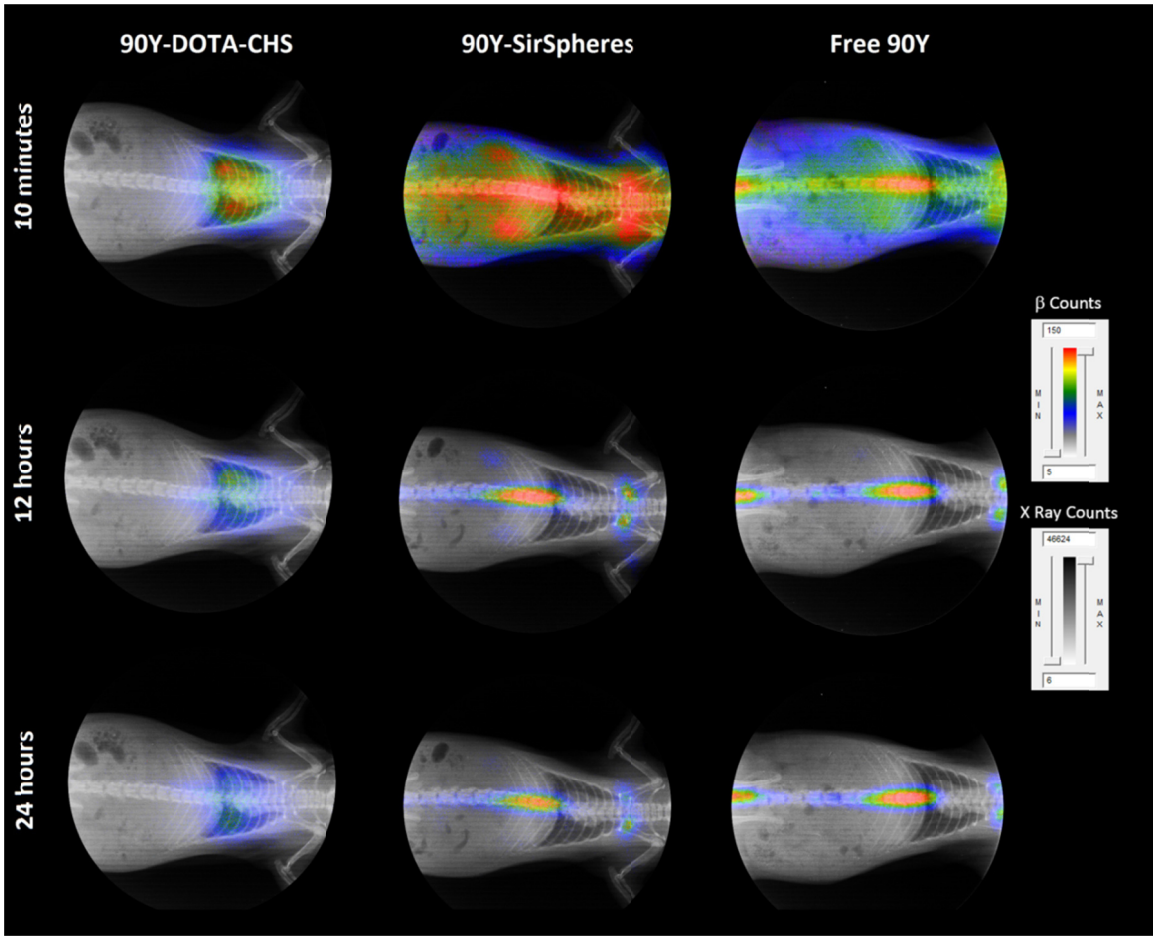

Fig 67 Non decay-corrected, un-collimated full body X-Ray/Autoradiography for ^{90}Y-DOTA-CHS, ^{90}Y-Resin and free ^{90}Y at 10 minutes, 12 and 24 hours.

The attachment of p-SCN-Bn-DOTA to CHS for the ^{90}Y-DOTA-CHS labeling dramatically improves the *in vivo* stability of the drug product. Furthermore the strong ^{90}Y-DOTA chelation did not release free ^{90}Y to the blood stream. The released particle degradation products (as ^{90}Y-DOTA-Fragments) acted as a radio-protector of the bone marrow and other organs by being quickly eliminated to the urine.

The collected organs for the ^{90}Y-Resin and free ^{90}Y showed a very similar picture. Great damage to the kidneys was observed with low urine output and significant swelling. In the case of ^{90}Y-Resin the lung were a bit discolored and swollen because of some radiation damage (due to the

allocation of 23% of the decay corrected injected activity at 24 hours). For the ^{90}Y-DOTA-CHS microspheres the radiation damage distribution was completely different. The lung were significantly discolored and fragile after 24 hours (due to the allocation of more than 95% of the decay corrected injected activity at 24 hours) while no visible damage was seen in the kidneys and normal urine output was observed. Note that venous injection of ^{90}Y microspheres so that they locate in the lungs would never be therapeutically indicated. This model was used only to investigate *in vivo* radiochemical stability and animals were not allowed to survive longer than 24 hours because of the organ damage that was expected to occur.

7.5 Conclusion

CHS microspheres within the 30±10 μm size range were successfully obtained. Surface modification of CHS microspheres with p-SCN-Bn-DOTA showed an optimal reaction time of 12 hours. The surface decoration did not affect the original size distribution or morphology. Maximum ^{90}Y capacity was found to be 12.1 ± 4.4 μCi/particle, which means that when using $3 \cdot 10^6$ to $30 \cdot 10^6$ particles (normal therapeutic range) maximum possible activity load is 36-360 Ci (orders of magnitude higher than real activities used). Maximum obtained labeling yield was 87.7±0.6 % when labeling at pH=7 and 37 ºC for 30 minutes. More than 90% *in vitro* stability was found in reconstituted 1% hemoglobin lysate after 72 hours. Particle *in vitro* degradation half-life in PBS was found to be greater than 21 days. *In vivo* studies with ^{90}Y-DOTA-CHS labeled microspheres show remarkable stability with more than 95 % of the injected activity (decay corrected) still in the lungs after 24 hours. ^{90}Y-DOTA-CHS performance was superior to the commercially available SirTex microspheres with only 23% (decay corrected) of the injected activity in the lungs after 24 hours. Autorradiography images obtained at 10 minutes showed strong release of ^{90}Y for the commercial particles. The addition of p-SCN-Bn-DOTA served to increase labeling yield and *in vivo* stability, but also to act as a radioprotectant for other organs

since less than 1% was found in bone marrow (regular ^{90}Y target organ). The 5 % ^{90}Y released from the lungs during the first 24 hours was quickly eliminated via urine.

CHAPTER 8 DOSIMETRY

8.1 Abstract

Monte Carlo particle transport code (MCNPX 2.7) and the rat whole body phantom (ROBY) were used to calculate animal's dose distribution for all the obtained experimental biodistributions. Maximum dose per decay to several target organs was calculated and visual dose distribution simulations are presented. Maximum dose to the lungs is delivered as expected when the successful perfusion and treatment agents are use. Other organ doses were also. The dosimetry study carried out complements the study of the designed microspheres allocating specific radiation fields to specific organs. The methods used have the potential to be extrapolated to humans as long as a proper phantom is used.

8.2 Introduction

Radiomicrosphere Therapy (RMT) as well as RMT planning are based on the utilization of the radiolabeled microspheres (and MAA microparticles) with the radioisotopes ^{68}Ga and ^{99m}Tc for imaging as well as ^{90}Y for therapy. Consequently, the emissions produced by the decay of the radioactive nuclei induce energy depositions (dose) in the tissues reached by the radiation fields.

Dosimetry (measurement of the deposited energy, dose) is an important factor to consider for both: the safety of the planning agents and the effectiveness of the planned treatment. Current FDA's "Guidance for Industry" only concerns about the safety of the overall treatment process (including planning). This means that the planning doses have to be under "reasonable limits" and the therapy dose biodistribution has to treat the damaged tissue with minimal (if any) damage to the surrounding organs (84). Concepts like "maximum feasible dose" and "maximum tolerated dose" are regularly used, which clearly target safety of administration. However low (if any) interest is paid to the therapeutic efficacy and the optimization of the administered dose.

The current status quo of radiotherapy was somehow justified by the complexity of the human tissue, organs size and distribution, changing from patient to patient. Also because the phantoms used to calculate deposited doses were far from a true human surrogate, making calculations unreliable and imprecise. However, with the advent and readily availability of CT and PET/CT systems, this approach is no longer justified. There is no need for anthropomorphic phantoms in dose calculations, since a CT will provide the real field of densities for the patient in question. Molecular imaging makes dose calculations even easier, since real PET quantification and biodistribution determination are possible. The afore mentioned advances, together with the readiness of powerful computers to calculate statistical energy distributions with the help of numerical (MCNP) methods renders the current medical practice outdated and inefficient.

8.3 Materials and Methods

This dosimetry assessment consisted of a numerical dosimetry approach based on the simulations of photon and electron transport utilizing the Monte Carlo particle transport code MCNPX 2.7 (85). The simulated numerical models considered specific aspects requirements related to case of study that can classified as: geometry, source, and detection.

8.3.1 Geometry

The modeled geometry is a numerical rat phantom voxelized with 0.5 mm resolution and 75 differentiated tissues/organs and generated by the ROBY (kindly provided by Michael G. Stabin, (86)) phantom (the main parameters used for building the phantom are showed in the ANNEX 1. Fig 68 and Fig 69 show 2D and 3D views respectively, of the visualization of the MCNPX ROBY model (visualization of the input).

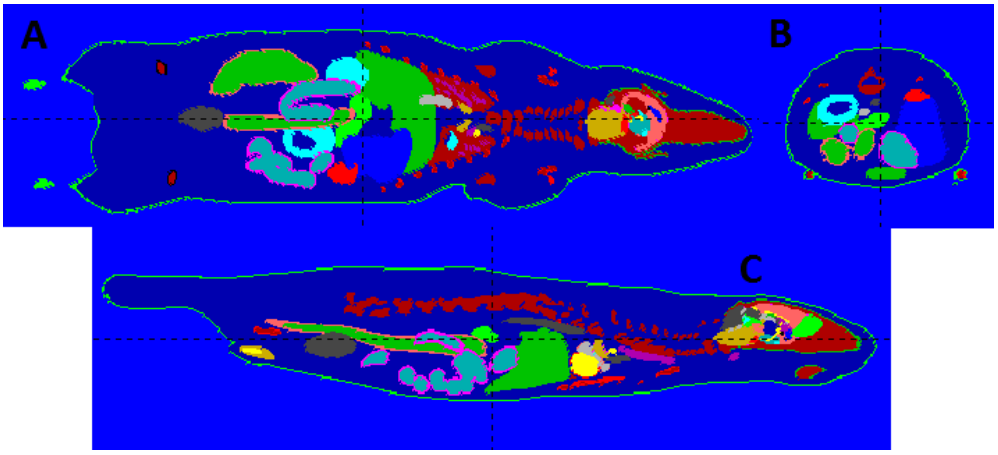

Fig 68 2D representations of the MCNPX ROBY model. The different views represent the following planes: A: Coronal; C: Sagittal; and B: Transverse.

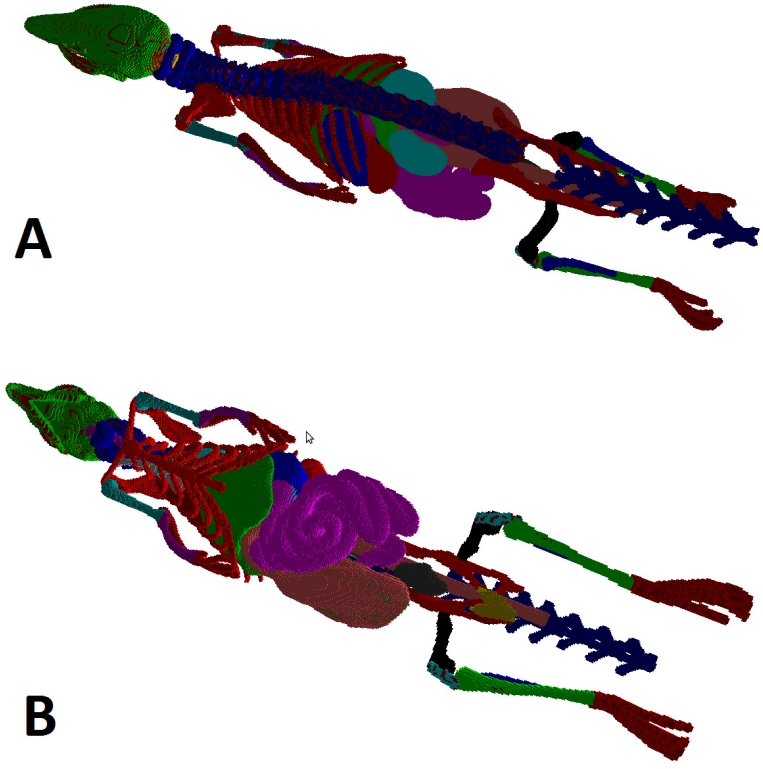

Fig 69 3D representations of the MCNPX ROBY model (visualization: MORITZ), back (above) and front (bottom) views. (Skin and muscles are removed from the image.)

In addition to the rat phantom, six 1 cm long water cylinders were located 1 cm away from the rat skin: around a middle-body transversal plane in the back, front, left, and right (1 cm diameter); and axially above the head and between the legs (0.5 cm diameter). Each detector has three detection regions along the axis of the cylinders with 1 mm (closest to the phantom) and 8 mm thicknesses (furthest away from the phantom). Fig 70 shows a 3D view of all the detectors surrounding the phantom and a 2D longitudinal view of one of the detectors near the phantom.

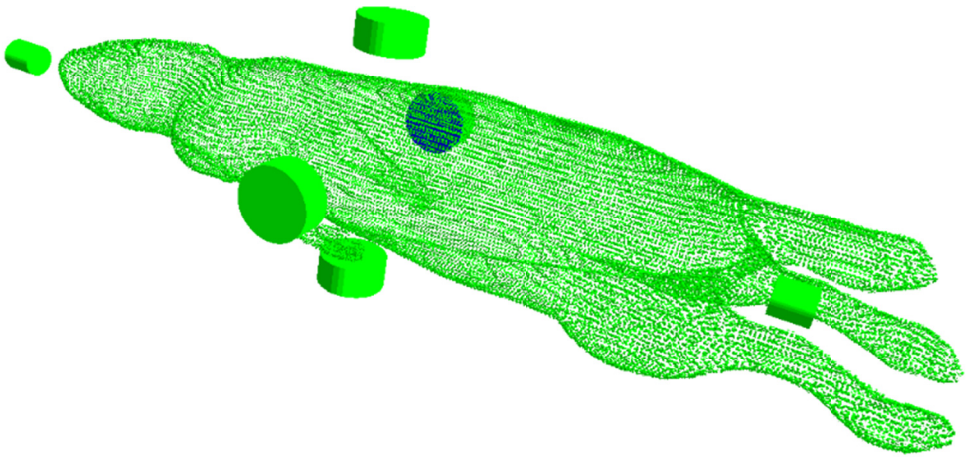

Fig 70 Visualizations of the water detectors for measuring doses in the surroundings of the rat phantom (visualization: MORITZ). 3D view (above): the detectors can be seen around the animal body

8.3.2 Source

The case of study considered three radioisotopes, ^{99m}Tc, ^{68}Ga, and ^{90}Y, with different biodistributions obtained from the afore described animal experiments (Chapters 4, 5, 6 and 7). Consequently, the simulations were performed using as sources each radioisotope biodistribution given by the experimental results. Every radioisotope emission was simulated according to evaluated nuclear data and the emissions were distributed uniformly within each organ with the intensity derived from the experiments. ANNEX 2 A shows the organ-by-organ emission

distributions obtained from the experiments. ANNEX 2 B shows re-casted distributions for the MCNPX ROBY model. This re-casting consists of obtaining the emission probability for each organ considering the whole body has emission probability equal to one and the compartmentalization of some organs/tissues. Scripts of three of the source files used for the simulations are shown in the ANNEX 1.

The experimental data was directly associated to the ROBY model in each of the measured organs. However, for other organs, ROBY has a multi-region definition and some assumptions were made to generate the simulation sources.

For calculations purposes in the geometric definition by ROBY software heart was considered as the combination of two ventricles (left: *myoLV*, and right: *myoRV*) and two atria (left: *myoLA*. The distribution in heart was assumed uniform and consequently each of the compartments was given an emission probability proportional to its volume adding all of them to the emission probability of the total heart. The activity of *blood* in the experimental data for the ^{68}Ga and ^{99m}Tc compounds was distributed among the blood in bone marrow, the blood in the cavities of the heart and their main vessels, and the blood distributed among the rest of the body (in the space not defined as any specific organs/tissues, mainly composed of muscle). It was assumed that blood occupies 7% of the volume of the body (87), that the whole marrow is red marrow and that the red marrow to blood activity concentration ratio (RMBLR) is 0.32 (88). Then, the blood in the cavities of the heart and their main vessels (100% blood) is distributed within *blood LV*, *blood RV*, *blood LA*, and *blood RA* source compartments (named *bldplLV*, *bldplRV*, *bldplLA*, and *bldplRA* in the geometric definition by ROBY software), which have volumes defined by ROBY. The activity concentration in *marrow* is 0.32 that of *blood LV* (or of the other 100%-blood pools). The volume of blood in the rest of the body was assumed to be the total blood volume minus the volume of *marrow*, *blood LV*, *blood RV*, *blood LA*, and *blood RA*. In the case of the compounds

with ^{90}Y, a similar procedure was performed for the values of *rest of the body*, *blood LV*, *blood RV*, *blood LA*, and *blood RA* but for *marrow*, which had an explicitly defined activity. The activity of *Urine* in the experimental data was assigned to the emission probability in the *bladder* of the numerical model.

8.3.3 Detection

The detection of the particles that provided the dose distributions was performed utilizing MCNPX and total mesh type 3 tallies (89). The first two types of tallies were used for assessing through two different methods, the average doses in each organ and in each of the detection regions of the detectors. Another mesh was included to calculate a voxelized 1 mm-resolution dosimetry along the phantom in order to visualize potential important dose distribution heterogeneities.

8.3.4 General Aspects

The composition of the materials that fill each of the regions of the phantom where extracted from the International Commission of Radiation Units and Measurements Report 46 that lists the elemental compositions for human tissues/organ (89). In the phantom appear tissues whose material composition are not explicitly described in the report and, for those cases, the values used were approximated to show organ/tissues composition according to its similarity. The file containing the definitions of the material compositions is shown in the ANNEX 1.

8.3.5 Other considerations of the particle transport.

In order to produce appropriate transport conditioning EFAC (see ANNEX 1, source files) and ESTEP (see ANNEX 1, material file), MCNPX parameters were adjusted considering a space resolution equal to or greater than 0.5 mm and Integrated Tiger Series option was chosen according to the suggestions given in (90).

8.4 Results and Discussion

The MCNPX /ROBY were simulated in collaboration with Dr. Manuel Sztejnberg in the Ezeiza Atomic Center, National Atomic Energy Comission, Buenos Aires, Argentina. Using 10^7 particles and CPU time of 57 days (*Intel Core i7 CPU 860 @ 2.80 GHz x 8* and OS *Ubuntu 12.04 (64-bits) [Linux kernel: 3.2.4-40-generic]*.

Complete dosimetry results can be found in ANNEX 3. It describes the absorbed dose per decay in each of the organs/tissues and the maximum dose among the detectors surrounding the phantom. Considering that the amount of decays per Becquerel is $5.86 \cdot 10^3$, $3.12 \cdot 10^4$, and 3.32×10^5 for ^{68}Ga, ^{99m}Tc, and ^{90}Y respectively, relative dose distributions are calculated and plotted for all ^{99m}Tc compounds in Fig 71, for all ^{68}Ga compounds in Fig 72 and for all ^{90}Y compounds in Fig 73.

In almost all of the cases the maximum dose per decay was delivered to lungs or bladder and the dose to the rest of the tissues is lower than 50% of the maximum. Maximum dose per decay is delivered to lungs in the following cases: ^{68}Ga-MAA (2h and 4h); ^{68}Ga-NOTA-CHSg (2h and 4h); ^{99m}Tc-MAA (2h and 4h); Free ^{99m}Tc (2h and 4h); ^{99m}Tc-CHSg (2h and 4h); ^{99m}Tc-PGCD 2h; ^{90}Y-DOTA-CHS 24h; and ^{90}Y-Resin 24h. For the case of ^{99m}Tc-PGCD 2h the dose to bladder is 67% of the maximum. Maximum dose per decay is delivered to bladder in the following cases: free ^{68}Ga (2h and 4h); ^{99m}Tc-PGCD 4h; ^{68}Ga-CHSg (confirming the need of the NOTA chelator); and ^{68}Ga-PGCD. For the cases of ^{99m}Tc-PGCD 4h and ^{68}Ga-CHSg the dose to lungs are 69% and 94%, respectively, of the maximum. Maximum dose per decay is delivered to kidneys in the case of free ^{90}Y 24h. In this case, the doses to bladder and marrow are 69% and 55% of the maximum. In the rest of the dose distributions marrow receives less than 10% of the maximum dose. Liver receives less than 12.5% of the maximum dose in all the cases but for free ^{90}Y 24h where it receives less than 33% of the maximum.

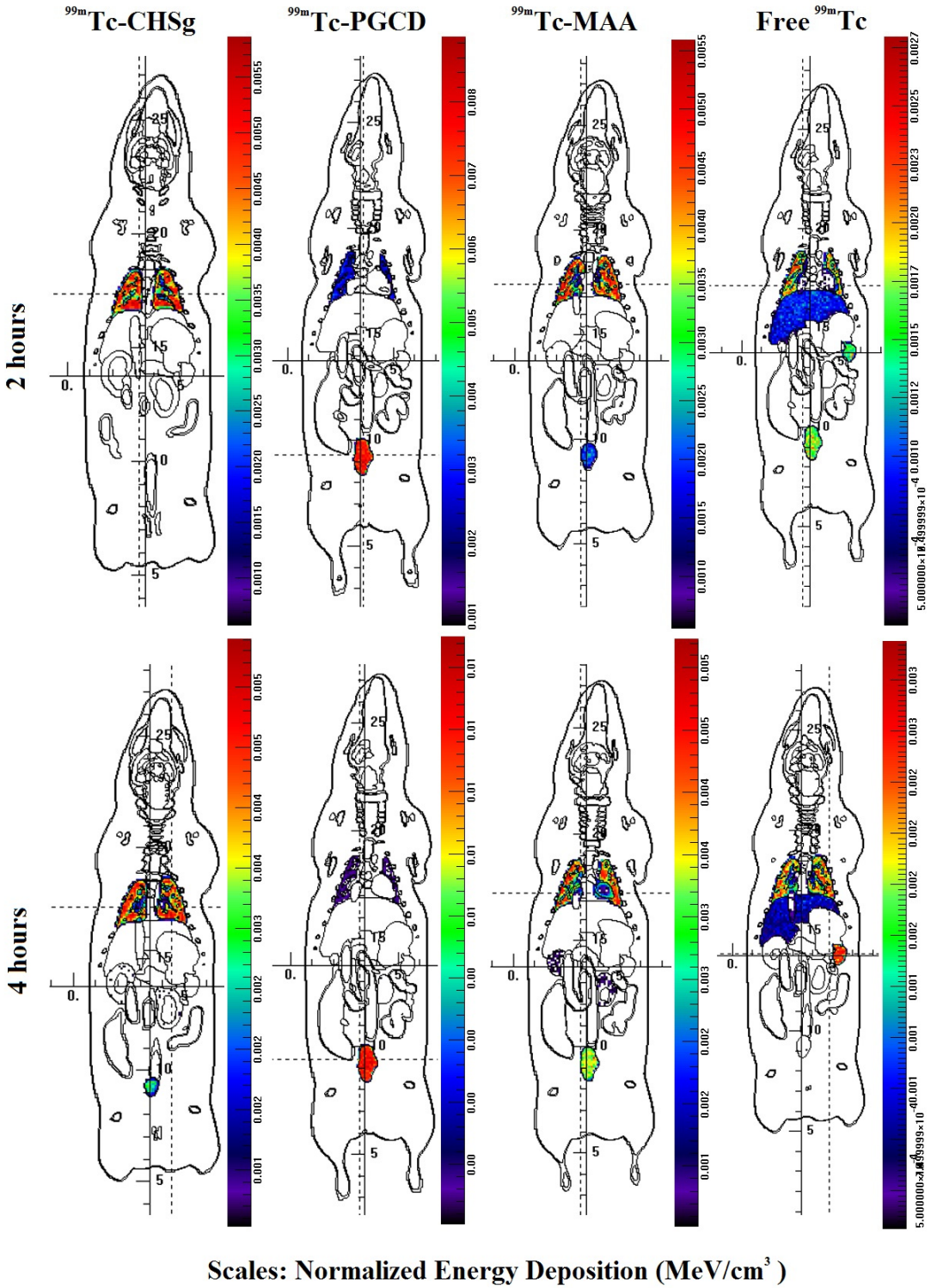

Fig 71 MCNP derived Dose Distribution in rats for all ^{99m}Tc labeled microparticles and free ^{99m}Tc at 2 and 4 hours post injection

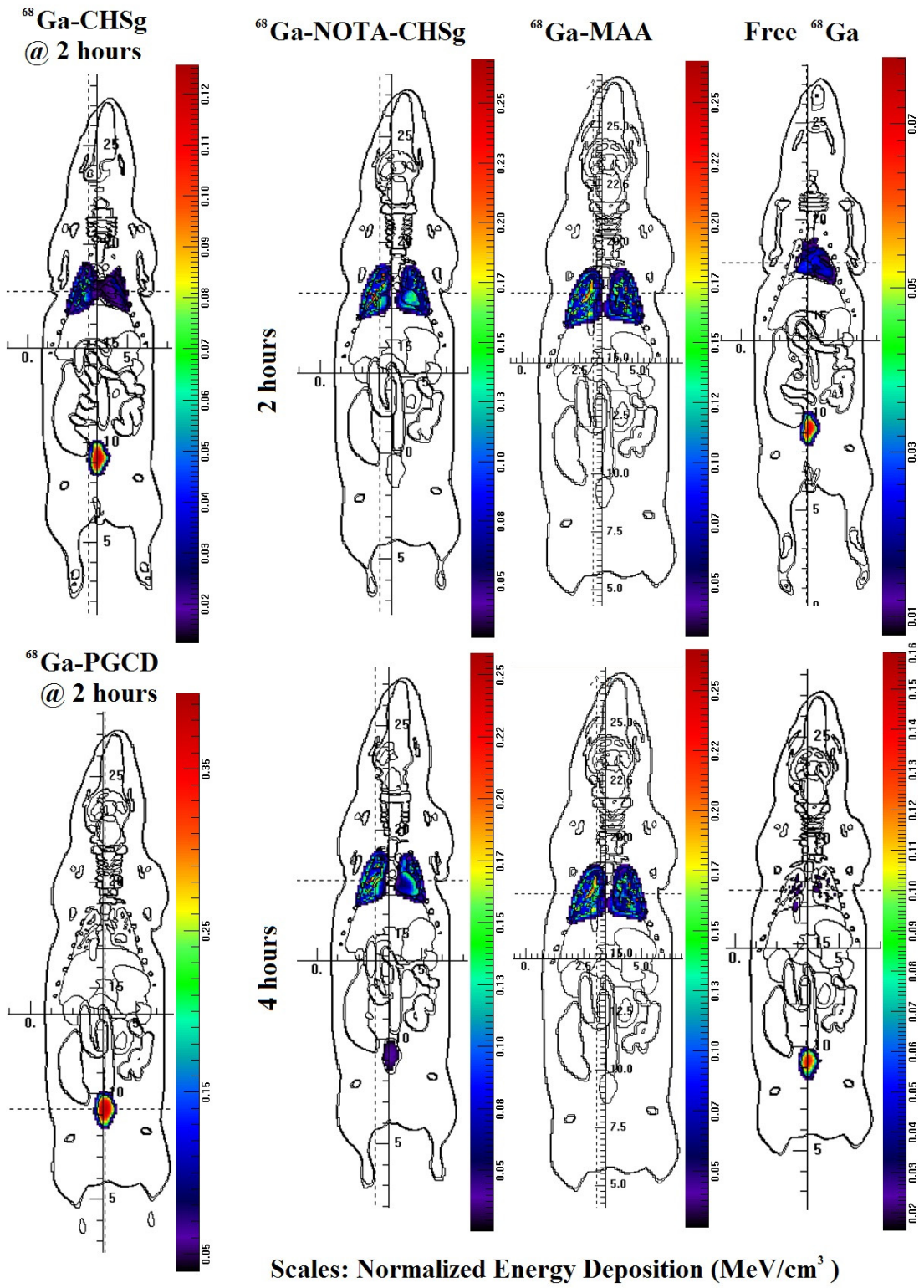

Fig 72 MCNP derived dose distribution in rats for all ^{68}Ga labeled microparticles and free ^{68}Ga at 2 hours post injections for ^{68}Ga-PGCD and ^{68}Ga-CHSg; 2 and 4 hours post injection for the rest

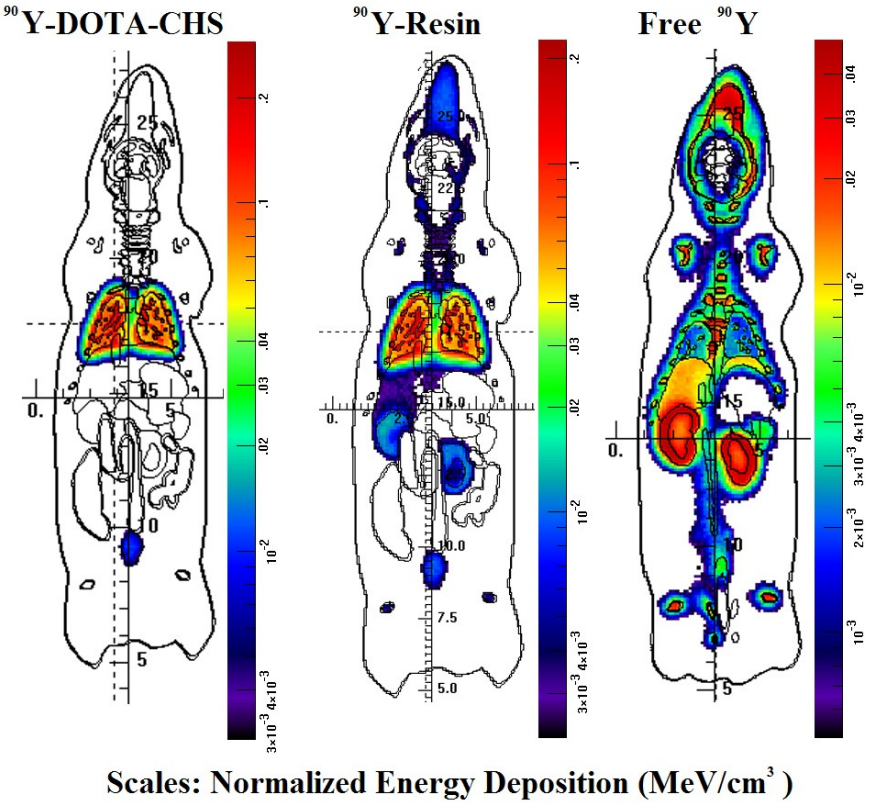

Fig 73 MCNP derived dose distribution in rats for all ^{90}Y labeled microparticles and free ^{90}Y at 24 hours post injection

The maximum doses in the surroundings of the phantom that could be determined as the maximum between the average skin dose and the maximum dose in the detectors was for all of the cases equal to or lower than 1.5% of the maximum dose to an organ/tissue.

The radiotolerance doses to the most affected organs (according to what was described in the previous paragraphs) are about 6.5, 20 (approximated through BED formalism), 7, 0.5 Gy (92). Comparing the relation of these doses to the relation between the maximum doses and organ doses one can determine the organs at the largest risk for each case: lungs for ^{68}Ga-MAA- (2h and 4h), ^{68}Ga-NOTA-CHSg (2h and 4h), ^{99m}Tc-MAA (2h and 4h), Free ^{99m}Tc (2h and 4h), ^{99m}Tc-CHSg (2h and 4h), ^{99m}Tc-PGCD (2h and 4h), ^{90}Y-DOTA-CHS 24h, and ^{90}Y-Resin 24h; bladder for ^{99m}Tc-PGCD 4h and ^{68}Ga-PGCD; and marrow for Free ^{68}Ga (2h and 4h), ^{68}Ga-CHSg, and free

^{90}Y 24h. Consequently, for each of the cases the doses to the corresponding above mentioned organ must be considered as maximum deliverable dose in order to avoid any type of normal tissue complication.

The utilization of the above mentioned tolerance doses would be a conservative approach since the effect of the reduction of the dose rate in the radioisotopes produces a less effective radiation damage induction.

8.5 Conclusion

The MCNPX/ROBY models for each of the compounds and sampling times were simulated with 10^7 particles and CPU time of 57 days. Maximum dose per decay is delivered to lungs in the following cases: ^{68}Ga-MAA, ^{68}Ga-NOTA-CHSg, ^{99m}Tc-MAA, free ^{99m}Tc, ^{99m}Tc-CHSg, ^{99m}Tc-PGCD; ^{90}Y-DOTA-CHS and ^{90}Y-Resin. The results are expected since most of these are the successful lung perfusion agents. For the case of ^{99m}Tc-PGCD the dose to bladder is 67% of the maximum after 2 hours. Maximum dose per decay is delivered to bladder for: free ^{68}Ga, ^{99m}Tc-PGCD, ^{68}Ga-CHSg, and ^{68}Ga-PGCD. Maximum dose per decay is delivered to kidneys in the case of free ^{90}Y. In this case, the doses to bladder and marrow are 69% and 55% of the maximum respectively. In the rest of the dose distributions marrow receives less than 10% of the maximum dose. Liver receives less than 12.5% of the maximum dose in all the cases except for free ^{90}Y where it receives less than 33% of the maximum. The dosimetry study carried out complements the study of the designed microspheres allocating specific radiation fields to specific organs.

LIMITATIONS AND FUTURE WORK

In the present study all of the microspheres were injected into the tail vein and deposited into the lungs, while the main intent of use is in liver tumor RMT, with the microspheres injected directly into the hepatic artery. The different vascular environments may result in different degradation rates and radiolabel stabilities. For example, intravascular injection results in the particles traveling through the heart with much longer exposure to flowing blood, which could impact stability. Different enzymes in the liver compared to the lungs could impact degradation. Even though large changes in stability are not to be expected, future experiments must be conducted injecting the radiolabeled particles in the hepatic artery and biodistribution assessed under conditions closer to those intended.

The emulsion method used to prepare the particles is time consuming, and the yield obtained for particles 30±10 μm vary from 20% to 95% depending on the material and method used. It is well known that microsphere synthesis is difficult to control with the precision required for commercialization. Automation and bulk manufacturing may be difficult to achieve. Therefore, new micro-fabrication methods should be developed to increase yield and consistency. Labeling, surface modification reactions and *in vivo* degradation are not expected to be affected by the change in the particle preparation method, since those depend on the intrinsic material characteristics. Tween®80 is known to be toxic and therefore it must be shown that no Tween® 80 remains at the end of the manufacturing process, or an alternative surfactant must be identified.

The ^{90}Y-DOTA-CHS *in vivo* experiments need to be extended to at least 21 days (corresponding to near total ^{90}Y decay), preferably with particle injection in the liver's hepatic artery. In the present study particles labeled with ^{90}Y were evaluated for only 24 hours because of their deposition in the lungs. Even when half-life should not be affected significantly for fast degrading particles (CHSg and CHSg-NOTA) in the liver, enzymes are likely to reduce the CHS-DOTA

microspheres degradation half-life. The combined effect of liver enzymes and ^{90}Y radiolysis for ^{90}Y-DOTA-CHS needs to be studied. In the future, tumor implantation in the liver and RMT planning/treatment effectiveness needs to be performed. Nevertheless, this preliminary study with the particles deposited in the lungs for 24 hours provided the necessary data to move forward with more complicated and costly experiments.

Finally, biodistribution of ^{90}Y-DOTA-CHS needs to be directly compared to ^{90}Y-Resin Spheres injected into the liver since the later particles are prescribed to be injected in water via the hepatic artery in the clinical RMT procedure. The injection of ^{90}Y-Resin into the tail vein might have decreased the in vivo stability of the ^{90}Y binding since the turbulence in the heart's chamber must have certainly exposed the particles to greater blood interaction than would occur when the particles are injected directly into the liver tumor vasculature. Having said this, the23% stability found 24 hours after injection into the tail vein is highly problematic from a safety standpoint. The very low in vivo stability of the ^{90}Y-Resin label in blood deserves closer scrutiny.

OVERALL CONCLUSIONS

Alternate labeling kits with 30±10 μm biodegradable microspheres were created and labeled with ^{68}Ga and/or ^{99m}Tc at >90% yield and radiochemical purity and 12 to 48 hours degradation half-life for its potential use in RMT planning. Appropriate emulsion and purification methods for the creation of 30±10 μm particles were designed and implemented to provide the necessary raw materials for the subsequent experiments. Radiolabeling of the particles was performed with more than 90% ^{68}Ga and/or ^{99m}Tc labeling yield and *in vitro* radiochemical purity for the studied periods. Surface modification of the particles with specific chelating agents to improve *in vitro* and *in vivo* stability was performed an optimized. *In vitro* stability studies of the particles in saline, PBS buffer and porcine plasma was performed and degradation half-lives determined. Several particles particle compositions were identified as treatment planning and treatment agents with variable degradation half-lifes. *In vivo* lung perfusion studies in Sprague Dawley were performed for the obtained particles. Stability and bio-distribution of the particles and the radioactive labels was determined. Three agents were identified for potential clinical translation: ^{99m}Tc-CHSg and ^{68}Ga-NOTA-CHSg for RMT planning and ^{90}Y-DOTA-CHS for treatment. Dosimetry calculations were also performed using the MCNPX-ROBY models and radiation dose distribution were found for all the studies compositions.

REFERENCES

1. SIRTeX. SIRTeX.com. [Online] SIRTeX. [Cited: 07 18, 2012.] http://www.sirtex.com/content.cfm?sec=world&MenuID=A040E9B4.

2. *Yttrium 90 Microsphere Selective Internal Radiation Treatment of Hepatic Colorectal Metastases.* Seza A. Gulec, MD and Yuman Fong, MD. 7, pp 675-682, s.l. : Arch Surg, 2007, Vol. 142.

3. *Randomised trial of SIR-Spheres® plus chemotherapy vs. chemotherapy alone for treating patients with liver metastases from primary large bowel cancer.* B. Gray, G. Van Hazel, M. Hope, M. Burton, P. Moroz, J. Anderson and V. Gebski. 1711-1720, s.l. : Ann Oncol, Vol. 12.

4. *Intraarterial Yttrium 90 in theTreatment of Hepatic Malignancy.* Rao V. P. Mantravadi, M.D. et al. 783-786, s.l. : Radiology, 1982, Vol. 142.

5. *Portal Hypertension Secondary to 90Yttrium Microspheres: An Unknown Complication.* Ahmet Ayav, Nagy Habib, and Long R. Jiao. 7820, s.l. : Journal of Clinical Oncology, 2005, Vol. 3.

6. *Radiation Pneumonitis After Selective Internal Radiation Treatment WithIntraarterial 90Yttrium-Microspheres For Inoperable Hepatic Tumors.* al, Thomas W et. 4, pp. 919-924, s.l. : Int. J. Radiation Oncology Biol. Phys, 1995, Vol. 33.

7. *Imaging of gamma emitters using scintillation cameras.* Ricard, Marcel. s.l. : Nuclear Instruments and Methods in Physics Research Section A: Accelerators, Spectrometers, Detectors and Associated Equipment, 2004.

8. Vallabhajosula, Shankar. *Molecular Imaging.* New York : Springer, 2009. 978-3-540-76734-3.

9. *Hybrid Imaging Technology: From Dreams and Vision to Clinical Devices.* James A. Patton, PhD,David W. Townsend, PhD, and Brian F. Hutton, PhD. 247-263, s.l. : Seminars in Nuclear Medicine, 2009, Vol. 39.

10. *Determination of Optimal Flood Source Radionuclide for Attenuation Correction of Single Photon Emission Computed Tomograms Using Simultaneous Transmission Computed Tomography.* Starr, Christopher Wilson. 07, s.l. : Dissertation Abstracts International, 1990, Vol. 51.

11. *SPECT scatter correction in non-homogeneous media.* S R Meikle, B F Hutton, D L Bailey, R R Fulton, K Schindhelm. s.l. : Information Processing in Medical Imaging: Lecture Notes in Computer Science, 1991, Vol. 511.

12. IAEA. *Clinical Applications of SPECT/CT: New Hybrid Nuclear Medicine Imaging System.* Vienna, Austria : Nuclear Medicine Section, International Atomic Energy Agency, 2008. 978-92-0-107108-8.

13. *Positron emission tomography/computed tomography.* Townsend, DW. 152-156, s.l. : Seminars in Nuclear Medicine, 2008, Vol. 38.

14. *The history of positron emission tomography.* R, Nutt. 1, s.l. : Molecular Imaging Biology, 2002, Vol. 4.

15. Craig Freudenrich, Ph.D. How Nuclear Medicine Works. *How Stuff Works.* [Online] 1998-2013 HowStuffWorks, Inc. [Cited: 04 18, 2013.] http://science.howstuffworks.com/nuclear-medicine1.htm.

16. *Positron Emission Tomography: A Review of Basic Principles, Scanner Design and Performance, and Current Systems.* Zanzonico, Pat. 2, s.l. : Seminars in Nuclear Medicine, 2004, Vol. 34.

17. Neutron Statistics. *Technical University of Munchen.* [Online] [Cited: 04 22, 2013.] http://www.frm2.tum.de/en/technik/reactor/neutron-statistics/index.html.

18. Department of Physics and Astronomy. *Georgia State University.* [Online] [Cited: 4 22, 2013.] http://hyperphysics.phy-astr.gsu.edu/hbase/nucene/fisfrag.html.

19. Troyer, GL. Medical Isotope Development And Supply Opportunities In The 21st Century. *http://medicalisotopes.org/.* [Online] RE Schenter, Advanced Medical Isotope Corp. [Cited: 4 22, 2013.] http://medicalisotopes.org/docs/poster_handoutcolor.pdf.

20. *Medical isotope shortage reaches crisis level.* Gould, Paula. 312-313, s.l. : Nature, 2009, Vol. 460.

21. *ACCELERATOR PRODUCTION OPTIONS FOR 99MO.* Bertsche, Kirk. Kyoto, Japan : Proceedings of IPAC'10, 2010.

22. Particles accelerators. *American Institu of Physics* . [Online] [Cited: 4 22, 2013.] http://www.aip.org/history/lawrence/epa.htm.

23. Eclipse Cyclotron. *World Molecular Imaging Society.* [Online] PlanClear. [Cited: 4 22, 2013.] http://www.wmis.org/2011/11/eclipse-cyclotron/.

24. Gregory Choppin, Jan-Olov Liljenzin, Jan Rydberg. *Radiochemistry and Nuclear Chemistry.* Woburn, MA : Elsevier, 2002. 978-0-7506-7463-8.

25. al, Michael Ernst Fassbender et. *Se-72/as-72 generator system based on se extraction/ as reextraction. US20130052133 A1* Los Alamos National Laboratory, USA, Feb 28, 2013. Application.

26. IAEA. Design principles of the 99Mo → 99mTc radionuclide generator. *IAEA.org.* [Online] [Cited: 4 22, 2013.] http://nucleus.iaea.org/HHW/Radiopharmacy/VirRad/Eluting_the_Generator/Generator_Module/Design_principles/index.html.

27. *Preparation of 90Y by the 90Sr-90Y generator for medical purpose.* S. Malja, K. Schomacker, E. Malja. 2, s.l. : Journal of Radioanalytical and Nuclear Chemistry, 2000, Vol. 245.

28. *A gallium-68 positron cow for medical use.* Yano Y, ANger HO. 484, s.l. : Journal of Nuclear Medicine, 1964, Vol. 5.

29. *68Ge/68Ga generators and 68Ga radiopharmaceutical chemistry on their way into a new century.* Roesch, Frank. 1, s.l. : Journal of Postgraduate Medicine, Education and Research, 2013, Vol. 47.

30. *68Ge-68Ga Generator with Alpha-Ferric Oxide Support.* AMBE, SHIZUKO. 1, s.l. : Applied Radiation and Isotopes, 1988, Vol. 39.

31. *The Application of Hydrous Tin(W) Oxide in Radiochemical Separations and, in Particular, for the 68Ge/68Ga and 82Sr/82Rb Generator Systems.* S. L. WATERS, P. L. HORLOCK and M. J. KENSETT. 7, s.l. : International journal of Applied Radiation and Isotopes, 1983, Vol. 34.

32. *The Renaissance of the 68Ge/68Ga Radionuclide Generator Initiates New Developments in 68Ga Radiopharmaceutical Chemistry.* Frank Roesch, Patrick Riss. 16, s.l. : Current Topics in Medicinal Chemistry, 2010, Vol. 10.

33. Riehle, Karolin. Eckert & Ziegler obtains manufacturing authorization for pharmaceutical Gallium-68 generators. *Reuters.* [Online] Thomson Reuters, 06 06, 2012. [Cited: 4 23, 2013.] http://www.reuters.com/article/2012/06/06/idUS80960+06-Jun-2012+BW20120606.

34. *Ventilation/perfusion lung scintigraphy: what is still needed? A review considering technetium-99m-labeled macro-aggregates of albumin.* Klaus Zöphel, Claudia Bacher-Stier, Jörg Pinkert, Joachim Kropp. 1-16, s.l. : Annals of NUclear Medicine, 2009, Vol. 23.

35. *Morphometry of the human lung.* ER, Weibel. s.l. : New York Academic Press, Heidelberg: Springer-Verlag, 1963.

36. *Pulmonary thromboembolism: epidemiology and techniques of nuclear medicine.* K, Weiss. 27-32, s.l. : Semin Thromb Hemost, 1996, Vol. 22.

37. *Validity of measuring regional pulmonary arterial blood fl ow with macroaggregates of human serum albumin.* Tow DE, Wagner HN Jr, Lopez-Majano V, Smith EM, Migita T. 76, s.l. : Am J Roentgenol Radium Ther Nucl Med, 1966, Vol. 96.

38. *Kinetics of technetium 99m labelled macroaggregated albumin in humans.* Malone LA, Malone JF, Ennis JT. 12, s.l. : British Journal of Radiology, 1983, Vol. 56.

39. *Quality control and testing of 99mTc-macroaggregated albumin.* Darte L, Persson BR, Soderbom L. 80-5, s.l. : Nuklearmedizin, 1976, Vol. 15.

40. *Evaluation and dosimetry of a 99mTc-Sn-MAA lung imaging agent in humans.* Robbins PJ, Feller PA, Nishiyama H. 173-8, s.l. : Health Physics, 1976, Vol. 30.

41. Doyle, Darragh. Bodies... *http://darraghdoyle.blogspot.com/.* [Online] 01 30, 2009. [Cited: 04 23, 2013.] http://darraghdoyle.blogspot.com/2009/01/bodies-exhibition-in-dublin-id-go-again.html.

42. *Enhancing Lung Scintigraphy With Single-Photon Emission Computed Tomography.* Paul J. Roach, Dale L. Bailey and Benjamin E. Harris. 441-449, s.l. : Seminars in Nuclear Medicine, 2008, Vol. 38.

43. Subramanian, Rhodes, Cooper and Sodd. *Radiopharmaceuticals.* s.l. : International Symposium on Radiopharmaceuticals, Society of Nuclear Medicine, 1975. 0-88416-041-6.

44. *99mTc-Human Albumin Microspheres (HAM) for Lung Imaging.* al, John A. Burdine et. 3, s.l. : Journal of Nuclear Medicine, 1970, Vol. 12.

45. *Adverse Reactions to Radiopharmaceuticals.* SNM, Pharmacopeia Committee of the. 3, s.l. : Journal of Nuclear Medicine, 1996, Vol. 12.

46. *Biologic determinants of absorbed dose estimates in Y-90 microsphere treatment of hepatic malignancies: Significance of tumor perfusion measured by Tc-99m MAA imaging.* Seza Gulec, Geraldine Mesoloras , William Dezarn, Patrick McNeillie and Andrew Kennedy. 396p, s.l. : Journal of Nuclear Medicine, 2007, Vol. 48.

47. *Cancer Statistics.* Ahmedin Jemal, DVM, PhD, et al., et al. 277-300, s.l. : CA CANCER J CLIN, 2010, Vol. 60.

48. *Hand-Assisted Laparoscopic Liver Surgery.* Mark C. Antonetti, MD, BrigidKillelea, MD and Rocco Orlando III, MD. APR, s.l. : ARCH SURG, 2002, Vol. 137.

49. *Minimally Invasive Catheter Implantation for Regional Chemotherapy of the Liver: A New Percutaneous Transsubclavian Approach,.* Frank K. Wacker, Jochen Boese-Landgraf, Armin Wagner, Dirk Albrecht, Karl-Jiirgen Wolf, Franz Fobbe. 128-132, s.l. : Cardiovasc Intervent Radiol, 1997, Vol. 20.

50. *Hepatic Arterial Chemoembolization in Patients with Liver Metastases of Endocrine Tumors.* al, Philippe Ruszniewski et. 8, pp 2624-2630, s.l. : Cancer, 1993, Vol. 71.

51. *Percutaneous cryoablation in combination with ethanol injection for unresectable hepatocellular carcinoma.* Ke-Cheng Xu, Li-ZhiNiu, Wei-Bin He, Zi-QianGuo, Yi-Ze Hu, Jian-Sheng Zuo. 12, 2686-2689, s.l. : World J Gastroenterol , 2003, Vol. 9.

52. *Radiofrequency Ablation of Malignant Liver Tumors.* Curley, Steven A. 14-23, s.l. : The Oncologist, 2001, Vol. 6.

53. *Preoperative Y-90 microsphere selective internal radiation treatment for tumor downsizing and future liver remnant recruitment: a novel approach to improving the safety of major hepatic resections.* Seza A Gulec, Kenneth Pennington, Michael Hall and Yuman Fong. 1(6), s.l. : World J. Surg Onc, 2009, Vol. 7.

54. *Safety and efficacy of Y-90 microsphere treatment in patients with primary and metastatic liver cancer: The tumor selectivity of the treatment as a function of tumor to liver flow ratio.* al, Seza A Gulec et. 15, s.l. : Journal of Translational Medicine, Vol. 5.

55. *Interactive Atlas of Human Anatomy.* Netter, Frank H. Fig 282A, s.l. : Icon Learning Systems LLC, 2003, Vols. Multimedia, 3rd Edition.

56. *Corrosion Cast of the Liver Circulatory System.* Viamonte, Manuel. s.l. : Teaching Files, 1973.

57. *A 3-D Liver Segmentation Method with Parallel Computing for Selective Internal Radiation Therapy.* Goryawala, M et al. 1, pp: 62-69, s.l. : Information Technology in Biomedicine, 2012, Vol. 16.

58. MD, Seza Gulec. Medical Practice Images. Goshen, Indiana - Miami, Florida : Unpublished, 2000-2012.

59. *Yttrium-90 Microsphere-selective Internal Radiation Therapy With Chemotherapy (Chemo-SIRT) for Colorectal Cancer Liver Metastases: An In Vivo Double-Arm-Controlled Phase II Trial.* Seza Gulec, MD et al. online, s.l. : American Journal of Clinical Oncology, 2012, Vol. not yet printed.

60. *The Significance of 99mTc-MAA SPECT/CT Liver Perfusion Imaging in Treatment Planning for 90Y-Microsphere Selective Internal Radiation Treatment.* al, Hojjat Ahmadzadehfar et. 8, s.l. : THE JOURNAL OF NUCLEAR MEDICINE, 2010, Vol. 51.

61. *Gallium-68-labeled Macroaggregated Human Serum Albumin, 68Ga-MAA.* Green, Gregory Even and Mark. 3, pp 319-321, s.l. : Nuc Med Biol, 1989, Vol. 16.

62. *68Ga PET/CT Ventilation–Perfusion Imaging for Pulmonary Embolism: A Pilot Study with Comparison to Conventional Scintigraphy.* al, Hofman et. 10, s.l. : The Journal of Nuclear Medicine, 2011, Vol. 52.

63. *Exclusion of extrahepatic shunt before SIRT by PET/CT with Gallium-68-labelled macroaggregated human serum albumin (68-Ga-MAA).* al, M. Gartenschlaeger et. 4, s.l. : Nuklearmedizin, 2011, Vol. 50.

64. *Positron emission tomography.* Hans Lundqvisty, Mark Lubberink and Vladimir Tolmachev. 537-552, s.l. : European Journal of Physics, 1998, Vol. 19.

65. *Improved column-based radiochemical processing of the generator produced 68Ga.* al, Loktionova et. 942-946, s.l. : Applied Radiation and Isotopes, 2011, Vol. 69.

66. *Rapid Separation of Gallium from Zinc Targets by Thermal Diffusion.* Lundqvist, Vladimir Tolmachev and Hans. 3, s.l. : Applied Radiation and Isotopes, 1996, Vol. 43.

67. *Inexpensive and cGMP capable Ga-68 purification system.* Amor Coarasa, A., S., Gulec and J., McGoron A. Miami : Journal of Nuclear Medicine, 2012. Vol. 53. SNM #1742.

68. *The Distribution, Metabolic Fate and Radiation Dosimetry of 131I Labeled Macroaggregated Albumin.* al, Eugene D. Furth et. 506-518, s.l. : Journal of Nuclear Medicine, 1971, Vol. 6.

69. *99mTc Sulfut Colloid Adsorbed on Ferric Hydroxide Macroaggregates for Lung Perfusion IMaging.* Huberty, J.P. 425, s.l. : International Journal of Applied Radiation and Isotopes, 1971, Vol. 22.

70. *PET Chemistry: The Driving Force in Molecular Imaging.* P.A. Schubiger, L. Lehmann, and M. Friebe. Berlin : Ernst Schering Foundation Symposium Proceedings, 2006. 978-3-540-32623-6.

71. *A convenient route to [68Ga]Ga-MAA for use as a particulate PET.* Carla J. Mathias, Mark A. Green. 1910-1912, s.l. : Applied Radiation and Isotopes, 2008, Vol. 66.

72. *Investigation forextrahepatic shunt before SIRT by PET/CT with 68Ga-MAA.* Gartenschlaeger M, Maus S, Buchholz H, Reber H, Pitton N, Schreckenberger M. N37-8, s.l. : Nuklearmedizin, 2011, Vol. 50(4).

73. *Clinical Evaluation of an Instant kit for Preparation of 99mTc-MAA for Lung Scaning.* Ramesh Charidra, Jack Shamoun, Philip Braunstein, and Oro L. DuHov. 702-705, s.l. : Journal of Nuclear Medicine, 1974, Vols. 14-9.

74. *Transactions of the 4th Annual Meeting American.* Tucker WD, Greene MW, Weiss AJ, et al. New York : Academic Press, 1958.

75. *Recent advances the use of biodegradable microparticles and nanoparticles in controlled drug delivery.* Brannon-Peppas, Lisa. 1-9, s.l. : International Journal of Pharmaceutics, 1995, Vol. 116.

76. *An innovative, quick and convenient labeling method for the investigation of pharmacological behavior and the metabolism of poly(DL-lactide-co-glycolide) nanospheres.* Magdalena Stevanovic, Tatjana Maksin, Jana Petkovic, Metka Filipic and Dragan Uskokovic. 335102, s.l. : Nanotechnology, 2009, Vol. 20.

77. *Evaluation of 99mTc labelled poly lactic acid microspheres for diagnostic radioembolization.* Ergün EL, Ercan MT, Selek H, Kaş HS, Ruacan S, Unsal IS, Mutlu M. 4, s.l. : Journal of Microencapsulation, 2000, Vol. 17.

78. *Molecular Nuclear Imaging for Targeting and Trafficking.* Bom, Hee-Seung. 5, s.l. : Nuclear Engineering and Technology, 2005, Vol. 38.

79. *Chitosan Microspheres: Therapeutic agent for liver-directed radiomicrosphere theray.* Amor Coarasa, A., et al., et al. Miami : Journal of Nuclear Medicine, 2012. Vol 53, Supplement 1, SNM# 1707.

80. *Chitosan and Chitosan Derivatives in Drug Delivery and Tissue Engineering.* Raphael Riva, Heloıse Ragelle, Anne des Rieux, Nicolas Duhem, Christine Jerome, and Veronique Preat. 19-44, s.l. : Advanced Polymer Sciences, 2011, Vol. 244.

81. *Preparation of a Promising Angiogenesis PET Imaging Agent: 68Ga-Labeled c(RGDyK)–Isothiocyanatobenzyl-1,4,7-Triazacyclononane-1,4,7-Triacetic Acid and Feasibility Studies in Mice.* al, Jae Min Jeong et. 830-836, s.l. : Journal of Nuclear Medicine, 2008, Vol. 49.

82. *Chitosan nanoparticles as new ocular drug delivery systems: in vitro stability, in vivo fate, and cellular toxicity.* de Campos AM, Diebold Y, Carvalho EL, Sánchez A, Alonso MJ. 6, s.l. : Pharm Res, 2005, Vol. 22.

83. *Functional characterization of chitin and chitosan.* al, Inmaculada Aranaz et. 203-230, s.l. : Current CHemical Biology, 2009, Vol. 3.

84. Administration, Food and Drug. *M3(R2) Nonclinical Safety Studies for the Conduct of Human Clinical Trials and Marketing Authorization for Pharmaceuticals.* s.l. : U.S. Department of Health and Human Services, 2010.

85. al, Denise B. Pelowitz et. MCNPX 2.7 A Extensions. *Los Alamos National Laboratory.* [Online] 11 06, 2008. [Cited: 04 23, 2013.] http://mcnpx.lanl.gov/opendocs/versions/v27a/v27a.pdf.

86. *Voxel-Based Mouse and Rat Models for Internal Dose Calculations.* al, Michael G. Stabin et. 655-659, s.l. : Journal of Nuclear Medicine, 2005, Vol. 47.

87. *PLGA–mPEG nanoparticles of cisplatin: in vitro nanoparticle degradation, in vitro drug release and in vivo drug residence in blood properties.* Avgoustakis, K et al. 123-135, s.l. : Journal of COntrolled Release, 2002, Vol. 79.

88. *Time Dependence of the Activity Concentration Ratio of Red Marrow to Blood and Implications for Red Marrow Dosimetry.* al, Cecilia Hindorf et. 4, s.l. : Cancer, 2001, Vol. 94.

89. *A CT-based Monte Carlo Dose Calculations for Proton Therapy Using a New Interface Program.* al, A. Esmaili Torshabi et. s.l. : World Academy of Science, Engineering and Technology, 2009, Vol. 29.

90. Measurements, International Commission of Radiation Units and. *Photon, Electron, Proton and Neutron Interaction Data for Body Tissues Report 46.* Bethesda, Maryland : ICRU Publications, 2000.

91. *ITS: The integrated TIGER Series of Electron/Photon Transport Codes - Version 3.0.* al, John A Halbleib et. s.l. : Nuclear Science Symposium and Medical Imaging Conference: Record of the 1991 IEEE, 1991.

92. *Extension of the biological effective dose to the MIRD schema and possible implications in radionuclide therapy dosimetry.* Sébastien Baechler, a) Robert F. Hobbs, Andrew R. Prideaux, Richard L. Wahl, and George Sgouros. 3 (1123-1134), s.l. : Med Phys, 2008 March, Vol. 35.

93. *Systematic Review of Randomized Trials for Unresectable Hepatocellular Carcinoma: Chemoembolization Improves Survival.* Bruix, Josep M. Llovet and Jordi. No. 2, Barcelona : HEPATOLOGY, February 2003, Vol. Vol. 37.

ANNEXES

ANNEX 1 MCNPX Simulation Parameters

ROBY parameter file, roby_140x140x550_50.par

```
mode = 0                    # program mode (0 = phantom, 1 = heart lesion, 2 = spherical lesion, 3 =
plaque, 4 = vectors, 5 = save anatomical variation) SEE NOTE 0
act_phan_each = 1           # activity_phantom_each_frame (1=save phantom to file, 0=don't save)
atten_phan_each = 1         # attenuation_coeff_phantom_each_frame (1=save phantom to file,
0=don't save)
act_phan_ave = 0            # activity_phantom_average    (1=save , 0=don't save) see NOTE 1
atten_phan_ave = 0          # attenuation_coeff_phantom_average  (1=save, 0=don't save) see NOTE
1

motion_option = 1           # motion_option  (0=beating heart only, 1=respiratory motion only,
2=both motions) see NOTE 2

out_period = 0.37                   # output_period (SECS) (if <= 0, then
output_period=time_per_frame*output_frames)
time_per_frame = 0          # time_per_frame (SECS) (**IGNORED unless output_period<=0**)
out_frames = 1              # output_frames (# of output time frames )

hrt_period = 0.171                          # hrt_period (SECS) (length of beating heart cycle;
normal = 1s) see NOTE 3
hrt_start_ph_index = 0.0            # hrt_start_phase_index (range=0 to 1; ED=0, ES=0.4) see
NOTE 3
heart_base = roby_heart.nrb                 # basename for heart files
heart_curve_file = heart_curve.txt          # name for file containing time curve for heart

resp_period = 0.37              # resp_period (SECS) (length of respiratory cycle; normal breathing
= 5s) see NOTE 3
resp_start_ph_index = 0.4           # resp_start_phase_index (range=0 to 1, full exhale= 0.0, full
inhale=0.4) see NOTE 3
max_diaphragm_motion = 1.0    # max_diaphragm_motion  (extent in mm's of diaphragm
motion; normal breathing = 1 mm) see NOTE 4
max_AP_exp = 0.7                    # max_AP_expansion  (extent in mm's of the AP expansion of
the chest; normal breathing = 0.7 mm) see NOTE 4

dia_filename = diaphragm_curve.dat      # name of curve defining diaphragm motion during
respiration
ap_filename = ap_curve.dat                  # name of curve defining chest anterior-posterior motion
during respiration

organ_file = roby.nrb                       # name of organ file that defines all organs

diaph_scale = 1.0                           # scales the diaphragm up or down

phantom_long_axis_scale = 1.0           # phantom_long_axis_scale (scales phantom laterally -
```

```
scales everything) SEE NOTE 5
phantom_short_axis_scale = 1.0          # phantom_short_axis_scale (scales phantom AP - scales
everything) SEE NOTE 5
phantom_height_scale = 1.0              # phantom_height_scale (scales phantom height - scales
everything) SEE NOTE 5

skin_long_axis_scale = 1.0              # skin_long_axis_scale (sets body transverse axis -
scales only body outline) SEE NOTE 5
skin_short_axis_scale = 1.0             # skin_short_axis_scale (sets body AP axis - scales only
body outline) SEE NOTE 5

bones_scale = 1.0                       # scales the bones about their center axes SEE NOTE 5

hrt_scale = 1.0                 # hrt_scale  (scales heart in 3D)

vol_liver = 0.0                 # sets liver volume (0 - do not change)
vol_pancreas = 0.0              # sets pancreas volume (0 - do not change)
vol_stomach = 0.0               # sets stomach volume (0 - do not change)
vol_spleen = 0.0                # sets spleen volume (0 - do not change)
vol_rkidney = 0.0               # sets right kidney volume (0 - do not change)
vol_lkidney = 0.0               # sets left kidney volume (0 - do not change)
vol_bladder = 0.0               # sets bladder volume (0 - do not change)
vol_testes = 0.0        # sets testes volume (0 - do not change)
vol_small_intest = 0.0          # sets small intestine volume (0 - do not change)
vol_large_intest = 0.0          # sets large intestine volume (0 - do not change)
vol_trachea = 0.0               # sets trachea volume (0 - do not change)
vol_thyroid = 0.0               # sets thyroid volume (0 - do not change)

vessel_flag = 1                 # vessel_flag (1 = include arteries and veins, 0 = do not include)
papillary_flag = 1              # papillary_flag (1 = include papillary muscles in heart, 0 = do
not include)

frac_H2O = 0.5          # fraction (by weight) of water in wet bone and wet spine (used to calc.
atten coeff)

marrow_flag = 1                         # render marrow (0 = no, 1 = yes)

thickness_skin = 0.5        # thickness skin (mm)

thickness_sternum = 0.4         # thickness sternum  (mm)
thickness_scapula = 0.4         # thickness scapulas (mm)
thickness_humerus = 0.45        # thickness humerus (mm)
thickness_radius = 0.45         # thickness radius (mm)
thickness_ulna = 0.45           # thickness ulna (mm)
thickness_hand = 0.2            # thickness hand bones (mm)
thickness_femur = 0.5           # thickness femur (mm)
thickness_tibia = 0.75          # thickness tibia (mm)
thickness_fibula = 0.45         # thickness fibula (mm)
thickness_patella = 0.3         # thickness patella (mm)
```

```
thickness_foot = 0.2              # thickness foot bones (mm)
thickness_ribs = 0.3              # thickness ribs     (mm)
thickness_backbone = 0.4          # thickness backbone (mm)
thickness_pelvis = 0.4            # thickness pelvis (mm)
thickness_skull = 0.4             # thickness skull (mm)
thickness_collar = 0.35           # thickness collarbones (mm)
thickness_si = 0.6        # thickness of small intestine wall (mm)
thickness_li = 0.6        # thickness of large intestine wall (mm)

pixel_width = 0.05        # pixel width (cm);  see NOTE 7
slice_width = 0.05        # slice width (cm);
array_size = 140          # array size
subvoxel_index = 1        # subvoxel_index (=1,2,3,4 -> 1,8,27,64 subvoxels/voxel, respectively)
startslice = 1            # start_slice;
endslice = 550            # end_slice;

d_ZY_rotation = 0         # change in zy_rotation (beta) in deg. (0); see NOTE 8
d_XZ_rotation = 0         # change in xz_rotation ( phi) in deg. (0);
d_YX_rotation = 0         # change in yx_rotation ( psi) in deg. (0);

X_tr = 0.0        # x translation in mm ;
Y_tr = 0.0        # y translation in mm ;
Z_tr = 0.0        # z translation in mm ;

activity_unit = 0         # activity units (1= scale by voxel volume; 0= don't scale)

skin_activity = 10                # skin_activity

hrt_myoLV_act = 12                # hrt_myoLV_act - activity in left ventricle myocardium
hrt_myoRV_act = 14                # hrt_myoRV_act - activity in right ventricle myocardium
hrt_myoLA_act = 16                # hrt_myoLA_act - activity in left atrium myocardium
hrt_myoRA_act = 18                # hrt_myoRA_act - activity in right atrium myocardium
hrt_bldplLV_act = 20              # hrt_bldplLV_act - activity in left ventricle chamber (blood
pool)
hrt_bldplRV_act = 22              # hrt_bldplRV_act - activity in right ventricle chamber (blood
pool)
hrt_bldplLA_act = 24              # hrt_bldplLA_act - activity in left atria chamber (blood pool)
hrt_bldplRA_act = 26              # hrt_bldplRA_act - activity in right atria chamber (blood pool)
body_activity = 28                # body_activity (background activity) ;
liver_activity = 30               # liver_activity;
gall_bladder_activity = 32        # gall_bladder_activity;
lung_activity = 34                # lung_activity;
airway_activity = 36              # airway activity;
st_wall_activity = 38             # st_wall_activity;  (stomach wall)
st_cnts_activity = 40             # st_cnts_activity;   (stomach contents)
pancreas_activity = 42            # pancreas_activity;
kidney_activity = 44              # kidney_activity;
spleen_activity = 46              # spleen_activity;
sm_intest_activity = 48           # small_intest_activity;
```

```
large_intest_activity = 50          # large_intest_activity;
bladder_activity = 52               # bladder_activity;
vas_def_activity = 54               # vas_def_activity;
testicular_activity = 56            # testicular_activity;
rib_activity = 58                   # rib_activity;
spine_activity = 60                 # spine_activity;
skull_activity = 62                 # skull_activity;

humerus_activity = 64               # humerus_activity
radius_activity = 66                # radius_activity
ulna_activity = 68                  # ulna_activity
femur_activity = 70                 # femur_activity
fibula_activity = 72                # fibula_activity
tibia_activity = 74                 # tibia_activity
patella_activity = 76               # patella_activity
bone_activity = 78                  # bone_activity (remaining bones)

brain_activity = 80                 # brain_activity;
cerebral_cortex_activity = 82       # cerebral_cortex_activity;
cerebellum_activity = 84                    # cerebellum_activity;
corpus_callosum_activity = 86       # corpus_callosum_activity;
brainstem_activity = 88             # brainstem_activity;
striatum_activity = 90              # striatum_activity;
thal_activity = 92                  # thal_activity;
hippo_activity = 94                 # hippo_activity;
hypothalamus_activity = 96          # hypothalamus_activity;
amygdala_activity = 98              # amygdala_activity;
lateral_septal_nuclei_activity = 100        # lateral_septal_nuclei_activity;
anterior_commissure_activity = 102          # anterior_commissure_activity;
anterior_pretectal_nucleus_activity = 104           # anterior_pretectal_nucleus_activity;
periaqueductal_gray_activity = 106          # periaqueductal_gray_activity;
aqueduct_activity = 108                     # aqueduct_activity;
cerebral_peduncle_activity = 110                    # cerebral_peduncle_activity;
cochlear_nuclei_activity = 112              # cochlear_nuclei_activity;
deep_mesencephalic_nuclei_activity = 114            # deep_mesencephalic_nuclei_activity;
fimbria_activity = 116                      # fimbria_activity;
fornix_activity = 118                       # fornix_activity;
globus_pallidus_activity = 120              # globus_pallidus_activity;
inferior_colliculus_activity = 122          # inferior_colliculus_activity;
internal_capsule_activity = 124             # internal_capsule_activity;
interpeduncular_nucleus_activity = 126      # interpeduncular_nucleus_activity;
lateral_dorsal_nucleus_of_thalamus_activity = 128           #
lateral_dorsal_nucleus_of_thalamus_activity;
lateral_geniculate_activity = 130                   # lateral_geniculate_activity;
lateral_lemniscus_activity = 132            # lateral_lemniscus_activity;
medial_geniculate_activity = 134                    # medial_geniculate_activity;
nucleus_accumbens_activity = 136                    # nucleus_accumbens_activity;
olfactory_areas_activity = 138              # olfactory_areas_activity;
optic_tract_activity = 140                  # optic_tract_activity;
```

```
pontine_gray_activity = 142              # pontine_gray_activity;
spinal_trigeminal_tract_activity = 144   # spinal_trigeminal_tract_activity;
substantia_nigra_activity = 146          # substantia_nigra_activity;
superior_colliculus_activity = 148       # superior_colliculus_activity;
pineal_gland_activity = 150              # pineal_gland_activity;
ventral_thalamic_nuclei_activity = 152   # ventral_thalamic_nuclei_activity;
ventricular_system_activity = 154                # ventricular_system_activity;


thyroid_activity = 156              # thyroid activity;

li_air_activity = 158      # large intestine air activity;
si_air_activity = 160      # small intestine air activity;

marrow_activity = 162   # bone marrow activity;

lesn_activity = 164                 # activity for heart lesion or plaque

energy  = 140    # radionuclide energy in keV (range 1-40MeV, increments of 0.5 keV) ; for attn.
map only

#----------------------Heart lesion parameters------------------------------SEE NOTE 9
ThetaCenter = 90.0                  # theta center in deg. (between 0 and 360)
ThetaWidth = 100.0                  # theta width in deg., total width (between 0 and 360 deg.)
XCenterIndex = .5                   # x center (0.0=base, 1.0=apex, other fractions=distances in
between)
XWidthIndex = 60                    # x width, total in mm's
Wall_fract = 1.0           # wall_fract, fraction of the outer wall transgressed by the lesion
#-------------------------------------------------------------------------

#----------------------Spherical lesion parameters--------------------------SEE NOTE 10
x_location = 80                     # x coordinate (pixels) to place lesion
y_location = 67                     # y coordinate (pixels) to place lesion
z_location = 85                     # z coordinate (pixels) to place lesion
lesn_diameter = 1.0                 # Diameter of lesion (mm)
#-------------------------------------------------------------------------

#----------------------Heart plaque parameters------------------------------SEE NOTE 11
p_center_v = 0.35                   # plaque center along the length of the artery (between 0 and 1)
p_center_u = 0.5                    # plaque center along the circumference of the artery (between 0
and 1)
p_height = 1.0                      # plaque thickness in mm.
p_width = 2.0                       # plaque width in mm.
p_length = 2.0                      # plaque length in mm.
p_id = 1462                         # vessel ID to place the plaque in
#-------------------------------------------------------------------------

#----------------------Vector parameters-----------------------------------SEE NOTE 12
vec_factor = 2         # higher number will increase the precision of the vector output
```

```
#-------------------------------------------------------------------------

#-------------------------------------------------------------------------
#-------------------------------------------------------------------------
#This is a general parameter file for the DYNAMIC MOBY phatom, version 1.0
#-------------------------------------------------------------------------
#THE PARAMETERS CAN BE IN ANY ORDER. THE PROGRAM WILL SORT THEM.
#-------------------------------------------------------------------------
#                       NOTES:
#-------------------------------------------------------------------------
#NOTE 0: The phantom program can be run in different modes as follows.
#  Mode 0: standard phantom generation mode that will generate phantoms of the
#         body.
#  Mode 1: heart lesion generator that will create phantoms of only the user
#         defined heart lesion. Subtract these phantoms from those of mode 0
#         to place the defect in the body.
#  Mode 2: spherical lesion generator that will create phantoms of only the
#         user defined lesion. Add these phantoms to those of mode 0 to place
#         the lesions in the body.
#  Mode 3: cardiac plaque generator that will create phantoms of only the
#         user defined plaque. Add these phantoms to those of mode 0 to place
#         the plaques in the body.
#  Mode 4: vector generator that will output motion vectors as determined from
#         the phantom surfaces. The vectors will be output as text files.
#  Mode 5: anatomy generator will save the phantom produced from the user-defined anatomy
#         parameters. The phantom is saved as two files, the organ file and the heart_base
#         file. The names of these files can then be specified in the parfile for later runs
#         with the program not having to take the time to generate the anatomy again. In using
#         a saved anatomy, be sure to set all scalings back to 1; otherwise, the anatomy will be
#         scaled again.
#
#NOTE 1: The average phantom is the average ONLY OF THOSE FRAMES GENERATED.
That is,
#  if you specify that only 2 frames be generated, then the average phantom is
#  just the average of those 2 frames.
#  ***************************************************************************
#  ** FOR A GOOD AVERAGE, generate at least 8-16 frames per 1 complete heart
#  ** cycle and/or per 1 complete respiratory cycle.
#  ***************************************************************************
#
#NOTE 2: Heart motion refers to heart BEATING or contraction, while resp.
#  motion refers to organ motion due to breathing. Note that the entire heart is
#  translated or rotated due to resp. motion, even if it is not contracting.
#  ** IF motion_option=1 , THE HEART WILL MOVE (TRANSLATE) BUT NOT BEAT.****
#
#NOTE 3:   Users sets the length and starting phase of both the heart
#         and respiratory cycles. NORMAL values for length of heart beat and
#         respiratory are cycles are 1 sec. and 5 secs., respectively,
#         BUT THESE CAN VARY AMONG PATIENTS and will increase if the patient
```

```
#         is under stress.
#
#         An index value between 0 and 1 is used the specify the starting phase
#         of the heart or resp cycles. IF NO MOTION IS SPECIFIED THEN THE STARTING
#         PHASE IS USED AS THE SINGLE PHASE AT WHICH THE PHANTOM IS
GENERATED.
#         (see documentation for more details).
#
#NOTE 3A:  These parameters control the LV volume curve of the heart. The user can specify the
LV
#             volume at 5 points in the cardiac cycle. Check the logfile to see what the default
volumes
#         are.  The end-diastolic volume can only be reduced. The way to increase it would be to
change
#         the overall heart scale.  The end-systolic volume can be increased or reduced. The other
volumes
#         need to have values between the end-diastolic and end-systolic volumes.  The time
durations for the
#         different portions of the cardiac cycle must add up to a total of 1.
#
#         Changing these parameters will alter the heart_curve.  The altered curve and heart files
can be output using
#         mode = 5.
#
#NOTE 4:  These NORMAL values are for normal tidal breathing.
#  ** Modeling a deep inhale may require higher values. **
#
#  The AP_expansion parameter controls the anteroposterior diameter of the ribcage, body,
#  and lungs. The ribs rotate upward to expand the chest cavity by the amount indicated by the
#  AP_expansion parameter. The lungs and body move with the expanding ribs. There is
maximum amount
#  by which the AP diameter can expand, due to the size of the ribs (some expansions are
impossible
#  geometrically.) If the user specifies too great an expansion, the program will terminate with an
#  error message.
#
#  The diaphragm motion controls the motion of the heart, liver, the left diaphragm, stomach,
spleen and
#  all organs downstream from them.
#
#
#NOTE 5: The phantom program outputs statistics on these anatomical parameters in the logfile it
generates.  The logfile is
#         named with the extension _log.  These statistics can be used to determine the amount of
scaling desired. Be aware
#             the phantom scaling parameters scale the entire phantom; therefore, any body, heart or
breast scalings  will
#         be additional to this base scaling.
#
```

```
#
#NOTE 7:
#       - The phantom dimensions do not necessarily have to be cubic. The array_size parameter
#         determines the x and y dimensions of the images.  The number of slices in the z dimension
#         is determined by the start_slice and end_slice parameters.  The total number of slices is
#         end_slice - start_slice + 1.
#
#NOTE 8:
#       - rotation parameters determine
#         initial orientation of beating (dynamic) heart LV long axis
#       - d_zy_rotation : +y-axis rotates toward +z-axis (about x-axis) by beta
#         d_xz_rotation : +z-axis rotates toward +x-axis (about y-axis) by phi
#         d_yx_rotation : +x-axis rotates toward +y-axis (about z-axis) by psi
#
#       - Based on patient data, the mean and SD heart orientations are:
#             zy_rot = -110 degrees (no patient data for this rotation)
#             xz_rot = 23 +- 10 deg.
#             yx_rot = -52 +- 11 deg.
#
#          Phantom will output total angles for the heart in the logfile
#
#NOTE 9: Creates lesion (defect) for the LEFT VENTRICLE ONLY.
#
#--------------------------------
#  theta_center: location of lesion center in circumferential dimension
#
#  theta center =    0.0  => anterior wall
#  theta center =  +90.0  => lateral   "
#  theta center = +180.0  => inferior  "
#  theta center = +270.0  => septal    "
#--------------------------------
#  theta_width : lesion width in circumferential dimension
#
#  TOTAL width of defect in degrees. So for example a width of 90 deg.
#  means that the width is 45 deg. on either side of theta center.
#--------------------------------
#  x center :   lesion center in long-axis dimension
#
#  x center = 0    -> base of LV
#  x center = 1.0  -> apex of LV
#--------------------------------
#  x width:  lesion width in long-axis dimension
#
#  total width. Defect extend half the total width on either side of the
#  x_center.
#
#  NOTE: if the specified width extends beyond the boundaries of the LV
#        then the defect is cut off and the effective width is less than the
#        specified width. So for example...
```

```
#
#--------------------------------
#  Wall_fract : fraction of the LV wall that the lesion transgresses
#  Wall_fract = 0.0 => transgresses none of the wall
#  Wall_fract = 0.5 => transgresses the inner half of the wall
#  Wall_fract = 1.0 => trangresses the entire wall
#--------------------------------
#
#
#NOTE 10: Creates a spherical lesion in the MOBY phantom. Depending on where the lesion is placed, it will move with
#        the respiratory motion. Location of the lesion is specified in pixel values.
#
#
#NOTE 11: Creates a plaque in the coronary vessel tree that will move with the cardiac/respiratory motion
#
#-------------------------------------------------------------------------------
#  plaque_center: location of plaque along the length of the specified artery
#    center = 0    -> base of artery
#    center = 1.0  -> apex of artery
#
#-------------------------------------------
#  plaque_thickness : plaque thickness in mm.
#
#-------------------------------------------
#  plaque_width :   plaque width in mm.
#
#-------------------------------------------
#  plaque_length :  plaque length in mm.
#
#-----------------------------------------------------
#  plaque_id  :  vessel to place the plaque in
#
#       AORTA = 423
#-----------------------------------------------------
#
#NOTE12:  Using mode = 4, vectors are output for each voxel of frame 1 to the current frame. The vectors show the motion
#        from the 1st frame to frame N. The vectors are output as text files with the format of
#        output_name_vec_frame1_frameN.txt.
#        The output vectors are a combination of known sampled points from the phantom objects and vectors interpolated
#        from these sampled points.  The known vectors are designated as such in the vector output. You can increase
#        the number of known points (and accuracy of the vector output) by increasing the parameter vec_factor.
```

ANNEX 2

ANNEX 2 A: Table 7 Experimental organ-by-organ emission distributions

Organ	^{68}Ga-MAA 2h	^{68}Ga-MAA 2h E	^{68}Ga-MAA 4h	^{68}Ga-MAA 4h E	^{68}Ga-CHSg-NOTA	^{68}Ga-CHSg-NOTA E	^{68}Ga-CHSg-NOTA 4h	^{68}Ga-CHSg-NOTA 4 h E	Free ^{68}Ga 2h	Free ^{68}Ga 2h E	Free ^{68}Ga 4h	Free ^{68}Ga 4h E
Spleen	0.1	0.0	0.1	0.0	0.1	0.0	0.1	0.0	0.6	0.5	1.6	0.1
Blood	0.8	0.8	0.8	0.0	0.1	0.1	0.5	0.1	84.9	4.5	63.1	3.9
Rib	0.0	0.0	0.0	0.0	0.0	0.0	0.0	0.0	0.5	0.4	1.3	0.4
Urine	0.1	0.0	0.1	0.0	0.5	0.4	3.5	0.6	6.8	2.9	14.0	1.7
Right Kidney	0.0	0.0	0.0	0.0	0.1	0.0	0.1	0.0	0.5	0.5	1.6	0.4
Left Kidney	0.0	0.0	0.0	0.0	0.1	0.0	0.1	0.0	0.5	0.5	1.4	0.2
Heart	0.0	0.0	0.0	0.0	0.0	0.0	0.0	0.0	0.7	0.7	1.5	0.2
Total Lungs	98.6	0.7	98.6	0.1	98.9	0.2	95.6	0.9	3.1	2.9	8.4	0.3
Total Liver	0.4	0.2	0.4	0.1	0.2	0.1	0.2	0.1	2.3	1.9	7.2	1.2
Organ	^{99m}Tc-MAA 2h	^{99m}Tc-MAA 2h E	^{99m}Tc-MAA 4h	^{99m}Tc-MAA 4h E	Free ^{99m}Tc 2h	Free ^{99m}Tc 2h E	Free ^{99m}Tc 4h	Free ^{99m}Tc 4h E	^{99m}Tc-CHSg 2h	^{99m}Tc-CHSg 2h E	^{99m}Tc-CHSg 4h	^{99m}Tc-CHSg 4h E
Spleen	0.1	0.0	0.1	0.0	7.2	1.1	11.8	0.7	0.0	0.0	0.1	0.0
Blood	0.9	0.2	0.9	0.0	1.3	1.2	0.4	0.0	0.7	0.5	0.8	0.1
Rib	0.0	0.0	0.0	0.0	0.0	0.0	0.0	0.1	0.0	0.0	0.0	0.0
Urine	7.6	1.3	12.3	1.2	6.1	4.0	0.6	0.2	4.9	2.5	10.0	2.1
Right Kidney	2.1	0.1	3.3	0.1	0.6	0.1	0.4	0.0	1.1	1.5	2.6	0.8
Left Kidney	2.2	0.2	3.4	0.2	0.6	0.1	0.4	0.0	1.2	1.6	2.6	0.8
Heart	0.0	0.0	0.1	0.0	0.2	0.0	0.2	0.0	0.0	0.0	0.0	0.0
Total Lungs	86.6	0.7	79.2	1.5	39.5	1.5	45.2	10.9	91.6	6.5	83.2	4.1

Total Liver	0.5	0.0	0.9	0.0	44.6	2.8	40.9	11.7	0.3	0.3	0.7	0.3

Organ	^{99m}Tc-PGCD 4h	^{99m}Tc-PGCD 4h E	^{68}Ga-CHSg 2h	^{68}Ga-CHSg 2h E	CHS-DOTA-^{90}Y 24h	CHS-DOTA-^{90}Y 24h E	RMTEX-^{90}Y 24h	RMTEX-^{90}Y 24h E	Free-^{90}Y 24h	Free-^{90}Y 24h E
Spleen	1.2	0.3	0.9	0.2	0.0	0.0	0.1	0.0	0.1	0.0
Blood	7.6	1.2	46.7	1.2	0.1	0.1	0.1	0.1	0.1	0.1
Rib	0.1	0.0	0.4	0.0	0.3	0.0	4.5	1.2	9.0	0.4
Urine	31.4	5.3	10.9	0.1	0.9	0.1	0.3	0.0	0.4	0.3
Right Kidney	3.8	0.3	0.9	0.2	0.1	0.0	0.6	0.1	1.3	1.0
Left Kidney	3.7	0.5	0.8	0.3	0.1	0.0	0.6	0.1	0.7	0.1
Heart	0.2	0.1	1.2	0.2	0.2	0.1	0.1	0.0	0.1	0.0
Total Lungs	29.9	1.1	31.9	1.3	95.4	1.6	23.0	4.3	0.2	0.0
Total Liver	19.8	1.9	6.3	0.7	0.3	0.0	1.1	0.3	1.8	0.1

ANNEX 2 B: Table 8 Re-casted distributions for the MCNPX ROBY model

	^{68}Ga-MAA 2h	^{68}Ga-MAA 4h	^{68}Ga-CHSg-NOTA 2h	^{68}Ga-CHSg-NOTA 4h	Free ^{68}Ga 2h	Free ^{68}Ga 4h	^{99m}Tc-MAA 2h	^{99m}Tc-MAA 4h	Free ^{99m}Tc 2h	Free ^{99m}Tc 4h
heart LV	1.4165E-4	1.7792E-4	2.5432E-4	3.5193E-4	5.5384E-3	1.2309E-2	3.0012E-4	4.5547E-4	1.4241E-3	1.6416E-3
heart RV	2.0553E-5	2.5816E-5	3.6900E-5	5.1063E-5	8.0360E-4	1.7860E-3	4.3545E-5	6.6086E-5	2.0663E-4	2.3819E-4
heart LA	3.7593E-6	4.7219E-6	6.7493E-6	9.3399E-6	1.4699E-4	3.2668E-4	7.9648E-6	1.2088E-5	3.7794E-5	4.3567E-5
heart RA	5.3000E-6	6.6571E-6	9.5154E-6	1.3168E-5	2.0722E-4	4.6056E-4	1.1229E-5	1.7042E-5	5.3284E-5	6.1423E-5
blood LV	2.8575E-4	2.9484E-4	3.1289E-5	1.8083E-4	3.1177E-2	2.3159E-2	3.4317E-4	3.1757E-4	4.5952E-4	1.5187E-4
blood RV	2.5285E-4	2.6088E-4	2.7686E-5	1.6001E-4	2.7587E-2	2.0492E-2	3.0365E-4	2.8100E-4	4.0660E-4	1.3438E-4
blood LA	8.3777E-5	8.6440E-5	9.1733E-6	5.3016E-5	9.1405E-3	6.7897E-3	1.0061E-4	9.3106E-5	1.3472E-4	4.4525E-5
blood RA	3.3027E-4	3.4077E-4	3.6163E-5	2.0900E-4	3.6034E-2	2.6766E-2	3.9663E-4	3.6705E-4	5.3111E-4	1.7553E-4
body rest	5.3385E-3	5.5082E-3	5.8455E-4	3.3783E-3	5.8246E-1	4.3266E-1	6.4112E-3	5.9330E-3	8.5849E-3	2.8373E-3
liver	4.1615E-3	4.1616E-3	2.4738E-3	1.5811E-3	2.3226E-2	7.2295E-2	4.5540E-3	8.8954E-3	4.4648E-1	4.0948E-1
lung	9.8559E-1	9.8519E-1	9.8847E-1	9.5574E-1	3.1361E-2	8.3633E-2	8.6566E-1	7.9180E-1	3.9480E-1	4.5185E-1
kidney	3.4462E-4	6.4526E-4	1.7168E-3	1.5842E-3	1.0718E-2	2.9883E-2	4.3414E-2	6.6444E-2	1.1586E-2	7.4213E-3
spleen	9.1440E-4	9.7711E-4	7.2734E-4	5.1691E-4	5.7897E-3	1.6148E-2	5.7300E-4	7.6736E-4	7.1775E-2	1.1838E-1
bladder	1.0375E-3	7.8540E-4	5.4485E-3	3.5174E-2	6.8173E-2	1.3975E-1	7.5964E-2	1.2274E-1	6.0699E-2	6.4290E-3
rib	0.0000E+0	0.0000E+0	0.0000E+0	5.0076E-	4.9928E-	1.2731E-2	1.2810E-4	1.5578E-4	4.2682E-	3.1113E-

				5	3				4	4
marrow	1.4907E-3	1.5381E-3	1.6323E-4	9.4337E-4	1.6265E-1	1.2082E-1	1.7903E-3	1.6567E-3	2.3973E-3	7.9229E-4
	^{99m}Tc-CHSg 2h	^{99m}Tc-CHSg 4h	^{99m}Tc-PGCD 2h	^{99m}Tc-PGCD 4h	^{68}Ga-CHSg	^{68}GaPGCD 2h	^{90}Y-CHS-DOTA 24h	^{90}Y-RMTEX 24h	Free ^{90}Y 24h	
heart LV	3.0155E-4	3.0609E-4	9.3994E-4	1.6211E-3	9.6185E-3	9.5181E-3	1.6175E-3	1.8834E-3	5.0518E-3	
heart RV	4.3753E-5	4.4412E-5	1.3638E-4	2.3522E-4	1.3956E-3	1.3810E-3	2.3469E-4	2.7326E-4	7.3299E-4	
heart LA	8.0027E-6	8.1234E-6	2.4945E-5	4.3024E-5	2.5526E-4	2.5260E-4	4.2927E-5	4.9982E-5	1.3407E-4	
heart RA	1.1283E-5	1.1453E-5	3.5168E-5	6.0656E-5	3.5988E-4	3.5613E-4	6.0519E-5	7.0467E-5	1.8902E-4	
blood LV	2.7229E-4	3.0800E-4	2.6679E-3	2.8651E-3	1.7147E-2	1.7980E-2	3.9397E-5	1.0943E-4	2.6426E-4	
blood RV	2.4094E-4	2.7253E-4	2.3607E-3	2.5352E-3	1.5172E-2	1.5910E-2	3.4861E-5	9.6833E-5	2.3383E-4	
blood LA	7.9832E-5	9.0299E-5	7.8219E-4	8.4001E-4	5.0271E-3	5.2715E-3	1.1551E-5	3.2084E-5	7.7476E-5	
blood RA	3.1472E-4	3.5598E-4	3.0836E-3	3.3115E-3	1.9818E-2	2.0782E-2	4.5535E-5	1.2648E-4	3.0543E-4	
body rest	5.0871E-3	5.7541E-3	4.9843E-2	5.3528E-2	3.2034E-1	3.3592E-1	7.3604E-4	2.0445E-3	4.9370E-3	
liver	2.9627E-3	6.6119E-3	2.7583E-2	2.0292E-1	6.3462E-2	4.9253E-2	2.8789E-3	3.7748E-2	1.3556E-1	
lung	9.1620E-1	8.3159E-1	5.6353E-1	3.0638E-1	3.1913E-1	5.6386E-2	9.7954E-1	7.5793E-1	1.1508E-2	
kidney	2.3517E-2	5.2606E-2	5.5335E-2	7.6429E-2	1.7184E-2	2.7100E-2	1.9219E-3	3.9834E-2	1.4701E-1	
spleen	4.5143E-4	7.5350E-4	8.0913E-3	1.1966E-2	9.0263E-3	7.6440E-3	2.5681E-4	1.8523E-3	5.4100E-3	
bladder	4.9037E-2	9.9534E-2	2.7106E-1	3.2175E-1	1.0856E-1	3.5116E-1	9.3067E-3	8.3853E-3	2.5702E-2	

rib	5.6434E-5	1.4234E-4	6.1325E-4	5.2629E-4	4.0457E-3	7.2820E-3	0.0000E+0	0.0000E+0	0.0000E+0
marrow	1.4205E-3	1.6068E-3	1.3918E-2	1.4947E-2	8.9454E-2	9.3803E-2	3.2743E-3	1.4956E-1	6.6289E-1

ANNEX 3: Table 9 Tabulated Dosimetry Calculations Results

			^{68}Ga-MAA 2h		**^{68}Ga-MAA 4h**		**CHSg-NOTA-^{68}Ga**		**CHSg-NOTA-^{68}Ga 4h**	
			MEAN	error	MEAN	error	MEAN	error	MEAN	error
Dose at @ 1 cm (mGy/decay)			3.39E-11	6E-13	3.39E-11	6E-13	3.35E-11	6E-13	3.29E-11	6E-13
Energy Dep (MeV)			8.228E-1	2E-4	8.228E-1	2E-4	8.231E-1	2E-4	8.230E-1	2E-4
Avg (mGy/decay)			4.134E-10	1E-13	4.133E-10	1E-13	4.135E-10	1E-13	4.135E-10	1E-13
Max D (mGy/decay)			3.87E-8		3.87E-8		3.89E-8		3.76E-8	
Min D (mGy/decay)			3.41E-12		3.41E-12		2.21E-12		4.56E-12	
	Vol (cm^3)	Mass (g)	Dose per tissue (mGy/decay)							
			MEAN	error	MEAN	error	MEAN	error	MEAN	error
skin	1.79E+1	1.95E+1	2.07E-11	6E-14	2.08E-11	6E-14	1.98E-11	6E-14	2.03E-11	6E-14
myoLV	5.75E-1	6.03E-1	5.66E-9	1E-11	5.66E-9	1E-11	5.68E-9	1E-11	5.51E-9	1E-11
myoRV	8.34E-2	8.75E-2	1.36E-9	8E-12	1.37E-9	8E-12	1.36E-9	8E-12	1.32E-9	8E-12
myoLA	1.53E-2	1.60E-2	4.74E-9	3E-11	4.74E-9	3E-11	4.74E-9	3E-11	4.59E-9	3E-11
myoRA	2.15E-2	2.26E-2	1.13E-8	4E-11	1.13E-8	4E-11	1.14E-8	4E-11	1.10E-8	4E-11

bldplLV	8.49E-1	9.00E-1	2.22E-9	5E-12	2.22E-9	5E-12	2.21E-9	5E-12	2.15E-9	5E-12
bldplRV	7.51E-1	7.96E-1	1.26E-9	4E-12	1.26E-9	4E-12	1.24E-9	4E-12	1.21E-9	4E-12
bldplLA	2.49E-1	2.64E-1	9.81E-9	2E-11	9.81E-9	2E-11	9.83E-9	2E-11	9.51E-9	2E-11
bldplRA	9.81E-1	1.04E+0	4.69E-9	7E-12	4.69E-9	7E-12	4.68E-9	7E-12	4.54E-9	7E-12
Rest of the body	2.27E+2	2.33E+2	1.94E-10	1E-13	1.94E-10	1E-13	1.93E-10	1E-13	1.94E-10	1E-13
Liver	1.04E+1	1.10E+1	1.07E-9	1E-12	1.07E-9	1E-12	1.06E-9	1E-12	1.02E-9	1E-12
Lung	2.88E+0	7.48E-1	3.87E-8	2E-11	3.87E-8	2E-11	3.89E-8	2E-11	3.76E-8	2E-11
Trachea	7.24E-1	7.46E-1	1.85E-8	1E-11	1.84E-8	1E-11	1.85E-8	1E-11	1.79E-8	1E-11
Stomach_Contents	4.65E+0	4.79E+0	9.08E-11	4E-13	9.09E-11	4E-13	8.93E-11	4E-13	8.62E-11	4E-13
Pancreas	5.08E-1	5.28E-1	3.70E-11	6E-13	3.81E-11	6E-13	3.94E-11	6E-13	3.90E-11	6E-13
Kidney	2.09E+0	2.19E+0	3.73E-11	4E-13	4.70E-11	4E-13	7.89E-11	6E-13	7.54E-11	6E-13
Spleen	8.13E-1	8.62E-1	1.09E-10	1E-12	1.16E-10	1E-12	9.17E-11	1E-12	7.34E-11	1E-12
Small_Intestine	4.23E+0	4.35E+0	2.04E-11	1E-13	2.07E-11	2E-13	1.99E-11	1E-13	2.12E-11	2E-13
Large_Intestine	1.95E+0	2.01E+0	1.72E-11	2E-13	1.71E-11	2E-13	2.36E-11	3E-13	7.25E-11	5E-13
Bladder	6.30E-1	6.49E-1	1.38E-10	2E-12	1.05E-10	2E-12	6.93E-10	4E-12	4.48E-9	1E-11
Vas_deferens	5.46E-2	5.63E-2	3.41E-12	5E-13	3.41E-12	5E-13	2.63E-12	4E-13	5.67E-12	7E-13
Testes	1.64E-1	1.70E-1	3.82E-12	3E-13	3.91E-12	3E-13	2.67E-12	2E-13	6.06E-12	4E-13
Wet_Rib_Bone	9.38E-1	1.32E+0	3.66E-9	4E-	3.66E-9	4E-	3.67E-9	4E-	3.55E-9	4E-12

				12		12		12		
Wet_Spine_Bone	4.14E+0	5.88E+0	5.00E-10	8E-13	5.00E-10	8E-13	4.98E-10	8E-13	4.84E-10	8E-13
Skull	1.24E+0	1.99E+0	1.00E-11	2E-13	1.01E-11	2E-13	6.52E-12	1E-13	8.52E-12	1E-13
humerus	2.42E-1	3.53E-1	5.60E-11	8E-13	5.61E-11	8E-13	5.26E-11	7E-13	5.28E-11	7E-13
radius	1.87E-1	2.73E-1	1.01E-10	1E-12	1.01E-10	1E-12	9.79E-11	1E-12	9.58E-11	1E-12
ulna	2.09E-1	3.06E-1	7.42E-11	9E-13	7.43E-11	9E-13	7.10E-11	9E-13	7.11E-11	9E-13
femur	4.44E-1	5.91E-1	7.26E-12	2E-13	7.44E-12	3E-13	3.74E-12	1E-13	7.68E-12	2E-13
fibula	1.41E-1	1.87E-1	5.34E-12	4E-13	5.52E-12	4E-13	2.36E-12	2E-13	4.94E-12	3E-13
tibia	5.17E-1	6.87E-1	4.82E-12	2E-13	4.87E-12	2E-13	2.21E-12	1E-13	4.56E-12	2E-13
patella	3.75E-2	4.99E-2	7.50E-12	8E-13	7.78E-12	8E-13	3.88E-12	5E-13	6.55E-12	7E-13
bone	1.96E+0	2.75E+0	2.95E-11	2E-13	2.97E-11	2E-13	2.69E-11	2E-13	2.95E-11	2E-13
brain_(backgrnd)	6.00E-2	6.24E-2	1.23E-11	8E-13	1.27E-11	8E-13	8.67E-12	6E-13	1.06E-11	7E-13
cerebral_cortex	1.58E+0	1.64E+0	9.49E-12	2E-13	9.54E-12	2E-13	7.84E-12	1E-13	8.58E-12	2E-13
cerebellum	5.41E-1	5.62E-1	1.44E-11	4E-13	1.44E-11	4E-13	1.32E-11	3E-13	1.36E-11	3E-13
corpus_callosum	1.20E-1	1.24E-1	8.62E-12	5E-13	8.62E-12	5E-13	8.17E-12	5E-13	8.25E-12	5E-13
brainstem	6.33E-1	6.59E-1	1.41E-11	3E-13	1.41E-11	3E-13	1.30E-11	3E-13	1.34E-11	3E-13
striatum	2.46E-1	2.56E-1	7.63E-12	4E-13	7.61E-12	4E-13	7.11E-12	3E-13	7.21E-12	3E-13
thal	1.09E-1	1.13E-1	8.00E-12	5E-13	8.04E-12	5E-13	7.79E-12	5E-13	7.83E-12	5E-13

hippo	3.01E-1	3.13E-1	9.88E-12	4E-13	9.87E-12	4E-13	9.43E-12	4E-13	9.41E-12	4E-13
hypothalamus	9.40E-2	9.78E-2	9.94E-12	7E-13	1.01E-11	7E-13	9.11E-12	6E-13	9.16E-12	6E-13
amygdala	1.48E-1	1.54E-1	1.00E-11	6E-13	1.00E-11	6E-13	8.66E-12	5E-13	9.32E-12	5E-13
lateral_septal_nuclei	4.69E-2	4.88E-2	6.73E-12	7E-13	6.73E-12	7E-13	6.69E-12	7E-13	6.54E-12	7E-13
anterior_commissure	1.19E-2	1.24E-2	1.23E-11	2E-12	1.23E-11	2E-12	1.19E-11	2E-12	1.17E-11	2E-12
anterior_pretectal_nucleus	1.36E-2	1.42E-2	9.08E-12	1E-12	9.08E-12	1E-12	9.14E-12	1E-12	8.89E-12	1E-12
periaqueductal_gray	3.66E-2	3.81E-2	9.73E-12	1E-12	9.73E-12	1E-12	9.75E-12	1E-12	9.43E-12	9E-13
aqueduct	4.38E-3	4.55E-3	1.14E-11	3E-12	1.14E-11	3E-12	1.04E-11	3E-12	1.14E-11	3E-12
cerebral_peduncle	1.86E-2	1.94E-2	8.87E-12	1E-12	8.87E-12	1E-12	8.80E-12	1E-12	8.59E-12	1E-12
cochlear_nuclei	2.23E-2	2.31E-2	1.56E-11	2E-12	1.56E-11	2E-12	1.44E-11	2E-12	1.51E-11	2E-12
deep_mesencephalic_nuclei	4.38E-2	4.55E-2	1.11E-11	1E-12	1.11E-11	1E-12	1.11E-11	1E-12	1.08E-11	1E-12
fimbria	2.21E-2	2.30E-2	7.36E-12	1E-12	7.36E-12	1E-12	7.22E-12	1E-12	7.10E-12	1E-12
fornix	1.56E-2	1.63E-2	8.34E-12	1E-12	8.61E-12	1E-12	8.08E-12	1E-12	8.08E-12	1E-12
globus_pallidus	2.70E-2	2.81E-2	8.56E-12	1E-12	8.56E-12	1E-12	7.63E-12	9E-13	7.89E-12	9E-13
inferior_colliculus	6.51E-2	6.77E-2	1.27E-11	9E-13	1.27E-11	9E-13	1.21E-11	8E-13	1.19E-11	8E-13
internal_capsule	4.13E-2	4.29E-2	7.70E-12	8E-13	7.72E-12	8E-13	7.63E-12	8E-13	7.47E-12	8E-13
interpeduncular_nucleus	4.75E-3	4.94E-3	1.31E-11	3E-12	1.31E-11	3E-12	1.24E-11	3E-12	1.23E-11	3E-12
lateral_dorsal_nucleus_of_thalamus	1.18E-2	1.22E-2	7.66E-	1E-	7.66E-	1E-	7.56E-	1E-	7.67E-	1E-12

			12	12	12	12	12	12	12	
lateral_geniculate	1.86E-2	1.94E-2	9.55E-12	1E-12	9.55E-12	1E-12	9.29E-12	1E-12	9.52E-12	1E-12
lateral_lemniscus	1.68E-2	1.74E-2	1.13E-11	1E-12	1.13E-11	1E-12	1.11E-11	1E-12	1.14E-11	1E-12
medial_geniculate	1.80E-2	1.87E-2	7.74E-12	1E-12	7.74E-12	1E-12	7.76E-12	1E-12	7.72E-12	1E-12
nucleus_accumbens	5.94E-2	6.18E-2	7.66E-12	7E-13	7.66E-12	7E-13	7.13E-12	7E-13	7.21E-12	7E-13
olfactory_areas	3.33E-1	3.46E-1	7.73E-12	4E-13	7.86E-12	4E-13	5.12E-12	3E-13	6.34E-12	3E-13
optic_tract	2.00E-2	2.08E-2	8.22E-12	1E-12	8.22E-12	1E-12	7.14E-12	1E-12	7.77E-12	1E-12
pontine_gray	2.44E-2	2.54E-2	1.17E-11	1E-12	1.20E-11	1E-12	9.51E-12	1E-12	1.06E-11	1E-12
spinal_trigeminal_tract	2.78E-2	2.89E-2	1.65E-11	1E-12	1.68E-11	1E-12	1.51E-11	1E-12	1.56E-11	1E-12
substantia_nigra	3.54E-2	3.68E-2	9.84E-12	1E-12	9.84E-12	1E-12	9.57E-12	1E-12	9.06E-12	1E-12
superior_colliculus	1.27E-1	1.32E-1	1.01E-11	5E-13	1.01E-11	5E-13	9.73E-12	5E-13	9.47E-12	5E-13
pineal_gland	3.00E-3	3.12E-3	1.26E-11	4E-12	1.21E-11	4E-12	1.20E-11	4E-12	1.20E-11	4E-12
ventral_thalamic_nuclei	5.75E-2	5.98E-2	8.85E-12	8E-13	8.85E-12	8E-13	8.76E-12	7E-13	8.35E-12	7E-13
ventricular_system	9.65E-2	1.00E-1	1.00E-11	6E-13	1.00E-11	6E-13	9.48E-12	6E-13	9.38E-12	6E-13
thyroid	2.62E-1	2.69E-1	2.12E-11	6E-13	2.12E-11	6E-13	2.05E-11	6E-13	1.99E-11	6E-13
Large_Int	8.76E+0	1.06E-2	1.52E-11	5E-13	1.51E-11	5E-13	1.80E-11	5E-13	4.49E-11	7E-13
Small_Int	1.00E+1	1.21E-2	1.92E-11	4E-13	1.95E-11	4E-13	1.85E-11	4E-13	2.01E-11	4E-13
marrow	1.38E+1	1.43E+1	5.83E-10	5E-13	5.83E-10	5E-13	5.78E-10	5E-13	5.63E-10	5E-13

			Free ^{68}Ga 2h		Free ^{68}Ga 4h		^{99m}Tc-MAA 2h		^{99m}Tc-MAA 4h	
			MEAN	error	MEAN	error	MEAN	error	MEAN	error
Dose at @ 1 cm (mGy/decay)			7.1E-11	1E-12	6.2E-11	1E-12	3.7E-12	1E-13	3.5E-12	1E-13
Energy Dep (MeV)			7.848E-1	2E-4	7.949E-1	2E-4	2.673E-2	2E-5	2.676E-2	2E-5
Avg (mGy/decay)			3.943E-10	1E-13	3.993E-10	1E-13	1.343E-11	1E-14	1.344E-11	1E-14
Max D (mGy/decay)			8.79E-9		1.79E-8		2.62E-9		2.39E-9	
Min D (mGy/decay)			2.40E-11		1.84E-11		4.55E-13		5.06E-13	

	Vol (cm^3)	Mass (g)	Dose per tissue (mGy/decay)							
			MEAN	error	MEAN	error	MEAN	error	MEAN	error
skin	1.79E+1	1.95E+1	1.30E-10	2E-13	1.02E-10	2E-13	2.33E-12	1E-14	2.32E-12	1E-14
myoLV	5.75E-1	6.03E-1	1.99E-9	6E-12	2.69E-9	7E-12	5.16E-11	4E-13	4.84E-11	4E-13
myoRV	8.34E-2	8.75E-2	1.91E-9	9E-12	1.85E-9	9E-12	2.30E-11	6E-13	2.19E-11	6E-13
myoLA	1.53E-2	1.60E-2	2.34E-9	2E-11	2.27E-9	2E-11	4.50E-11	2E-12	4.16E-11	2E-12
myoRA	2.15E-2	2.26E-2	2.39E-9	2E-11	2.71E-9	2E-11	1.31E-10	4E-12	1.22E-10	4E-12
bldplLV	8.49E-1	9.00E-1	2.60E-9	6E-12	2.27E-9	5E-12	3.04E-11	2E-13	2.81E-11	2E-13
bldplRV	7.51E-1	7.96E-1	3.17E-9	7E-12	2.63E-9	7E-12	2.78E-11	2E-13	2.55E-11	2E-13
bldplLA	2.49E-1	2.64E-1	2.94E-9	1E-11	2.89E-9	1E-11	8.63E-11	8E-13	7.90E-11	8E-13
bldplRA	9.81E-1	1.04E+0	2.73E-9	6E-12	2.42E-9	5E-12	4.20E-11	3E-13	3.89E-11	3E-13
Rest of the body	2.27E+2	2.33E+2	3.39E-10	1E-13	2.95E-10	1E-13	4.92E-12	6E-15	4.97E-12	6E-15

Liver	1.04E+1	1.10E+1	3.89E-10	7E-13	8.87E-10	1E-12	1.84E-11	5E-14	1.85E-11	6E-14
Lung	2.88E+0	7.48E-1	1.89E-9	4E-12	3.92E-9	6E-12	2.62E-9	3E-12	2.39E-9	3E-12
Trachea	7.24E-1	7.46E-1	1.17E-9	3E-12	2.06E-9	5E-12	1.93E-10	8E-13	1.77E-10	8E-13
Stomach_Contents	4.65E+0	4.79E+0	9.65E-11	5E-13	1.42E-10	6E-13	6.97E-12	4E-14	6.77E-12	4E-14
Pancreas	5.08E-1	5.28E-1	2.18E-10	2E-12	2.42E-10	2E-12	5.55E-12	1E-13	6.12E-12	1E-13
Kidney	2.09E+0	2.19E+0	4.97E-10	2E-12	1.11E-9	3E-12	5.58E-11	3E-13	8.47E-11	4E-13
Spleen	8.13E-1	8.62E-1	6.36E-10	3E-12	1.58E-9	5E-12	5.18E-12	1E-13	6.10E-12	1E-13
Small_Intestine	4.23E+0	4.35E+0	1.85E-10	6E-13	1.84E-10	6E-13	2.95E-12	3E-14	3.45E-12	3E-14
Large_Intestine	1.95E+0	2.01E+0	3.22E-10	1E-12	4.16E-10	1E-12	3.48E-12	5E-14	4.67E-12	6E-14
Bladder	6.30E-1	6.49E-1	8.79E-9	1E-11	1.79E-8	2E-11	3.21E-10	1E-12	5.16E-10	2E-12
Vas_deferens	5.46E-2	5.63E-2	1.43E-10	4E-12	1.14E-10	4E-12	8.77E-13	1E-13	1.18E-12	1E-13
Testes	1.64E-1	1.70E-1	1.51E-10	3E-12	1.21E-10	2E-12	8.59E-13	8E-14	1.31E-12	1E-13
Wet_Rib_Bone	9.38E-1	1.32E+0	5.96E-10	1E-12	8.67E-10	2E-12	3.89E-11	2E-13	3.60E-11	2E-13
Wet_Spine_Bone	4.14E+0	5.88E+0	3.66E-10	7E-13	3.09E-10	6E-13	1.02E-11	5E-14	9.75E-12	5E-14
Skull	1.24E+0	1.99E+0	4.43E-10	1E-12	3.30E-10	1E-12	8.55E-13	3E-14	7.88E-13	3E-14
humerus	2.42E-1	3.53E-1	4.42E-10	3E-12	3.34E-10	2E-12	8.16E-12	2E-13	7.50E-12	2E-13
radius	1.87E-1	2.73E-1	4.05E-10	3E-12	3.12E-10	3E-12	1.47E-11	3E-13	1.36E-11	3E-13
ulna	2.09E-1	3.06E-1	3.96E-	3E-	3.02E-	3E-	1.04E-	2E-	9.57E-	2E-13

			10	12	10	12	11	13	12	
femur	4.44E-1	5.91E-1	4.87E-10	2E-12	3.66E-10	2E-12	1.36E-12	6E-14	1.83E-12	7E-14
fibula	1.41E-1	1.87E-1	3.57E-10	3E-12	2.67E-10	3E-12	4.55E-13	6E-14	6.28E-13	7E-14
tibia	5.17E-1	6.87E-1	3.26E-10	2E-12	2.45E-10	2E-12	4.92E-13	4E-14	6.13E-13	4E-14
patella	3.75E-2	4.99E-2	4.00E-10	6E-12	2.98E-10	5E-12	5.26E-13	1E-13	8.18E-13	1E-13
bone	1.96E+0	2.75E+0	3.43E-10	9E-13	2.66E-10	8E-13	3.43E-12	4E-14	3.70E-12	5E-14
brain_(backgrnd)	6.00E-2	6.24E-2	4.46E-10	5E-12	3.31E-10	4E-12	8.16E-13	1E-13	8.27E-13	1E-13
cerebral_cortex	1.58E+0	1.64E+0	2.18E-10	1E-12	1.64E-10	1E-12	6.95E-13	2E-14	6.60E-13	2E-14
cerebellum	5.41E-1	5.62E-1	1.74E-10	2E-12	1.31E-10	2E-12	1.43E-12	6E-14	1.34E-12	6E-14
corpus_callosum	1.20E-1	1.24E-1	7.69E-11	2E-12	5.86E-11	1E-12	8.14E-13	8E-14	7.57E-13	8E-14
brainstem	6.33E-1	6.59E-1	1.59E-10	2E-12	1.21E-10	1E-12	1.31E-12	5E-14	1.24E-12	5E-14
striatum	2.46E-1	2.56E-1	5.80E-11	1E-12	4.43E-11	1E-12	6.61E-13	6E-14	6.13E-13	5E-14
thal	1.09E-1	1.13E-1	3.47E-11	1E-12	2.59E-11	1E-12	7.86E-13	1E-13	7.57E-13	9E-14
hippo	3.01E-1	3.13E-1	7.29E-11	1E-12	5.52E-11	1E-12	8.37E-13	6E-14	8.02E-13	6E-14
hypothalamus	9.40E-2	9.78E-2	2.09E-10	5E-12	1.60E-10	4E-12	8.10E-13	1E-13	7.85E-13	1E-13
amygdala	1.48E-1	1.54E-1	2.08E-10	4E-12	1.54E-10	3E-12	8.56E-13	9E-14	8.27E-13	9E-14
lateral_septal_nuclei	4.69E-2	4.88E-2	4.14E-11	2E-12	3.17E-11	2E-12	5.95E-13	1E-13	6.11E-13	1E-13
anterior_commissure	1.19E-2	1.24E-2	5.93E-11	4E-12	4.91E-11	4E-12	5.41E-13	2E-13	5.20E-13	2E-13

anterior_pretectal_nucleus	1.36E-2	1.42E-2	2.70E-11	3E-12	2.03E-11	2E-12	5.88E-13	2E-13	5.06E-13	2E-13
periaqueductal_gray	3.66E-2	3.81E-2	2.95E-11	2E-12	2.33E-11	2E-12	9.20E-13	2E-13	7.88E-13	1E-13
aqueduct	4.38E-3	4.55E-3	3.78E-11	6E-12	2.96E-11	6E-12	6.40E-13	4E-13	6.04E-13	4E-13
cerebral_peduncle	1.86E-2	1.94E-2	1.35E-10	6E-12	1.04E-10	5E-12	6.95E-13	2E-13	6.84E-13	2E-13
cochlear_nuclei	2.23E-2	2.31E-2	2.34E-10	8E-12	1.74E-10	7E-12	1.41E-12	3E-13	1.36E-12	3E-13
deep_mesencephalic_nuclei	4.38E-2	4.55E-2	2.82E-11	2E-12	2.19E-11	1E-12	1.32E-12	2E-13	1.25E-12	2E-13
fimbria	2.21E-2	2.30E-2	2.40E-11	2E-12	1.84E-11	2E-12	9.36E-13	2E-13	8.43E-13	2E-13
fornix	1.56E-2	1.63E-2	8.93E-11	5E-12	6.91E-11	4E-12	8.77E-13	2E-13	7.99E-13	2E-13
globus_pallidus	2.70E-2	2.81E-2	4.93E-11	3E-12	3.78E-11	3E-12	8.94E-13	2E-13	8.44E-13	2E-13
inferior_colliculus	6.51E-2	6.77E-2	1.16E-10	4E-12	8.58E-11	3E-12	1.18E-12	2E-13	1.15E-12	2E-13
internal_capsule	4.13E-2	4.29E-2	3.55E-11	2E-12	2.80E-11	2E-12	8.78E-13	2E-13	8.70E-13	2E-13
interpeduncular_nucleus	4.75E-3	4.94E-3	8.29E-11	1E-11	6.41E-11	8E-12	1.45E-12	6E-13	1.29E-12	5E-13
lateral_dorsal_nucleus_of_thalamus	1.18E-2	1.22E-2	2.40E-11	3E-12	1.93E-11	2E-12	8.17E-13	3E-13	6.91E-13	2E-13
lateral_geniculate	1.86E-2	1.94E-2	2.81E-11	2E-12	2.15E-11	2E-12	9.50E-13	3E-13	8.19E-13	2E-13
lateral_lemniscus	1.68E-2	1.74E-2	4.44E-11	3E-12	3.55E-11	3E-12	1.51E-12	3E-13	1.29E-12	3E-13
medial_geniculate	1.80E-2	1.87E-2	3.08E-11	3E-12	2.24E-11	2E-12	1.31E-12	3E-13	1.31E-12	3E-13
nucleus_accumbens	5.94E-2	6.18E-2	1.29E-10	4E-12	9.76E-11	4E-12	7.53E-13	1E-13	7.40E-13	1E-13
olfactory_areas	3.33E-1	3.46E-1	3.06E-	3E-	2.29E-	3E-	5.91E-	5E-	5.68E-	5E-14

			10	12	10	12	13	14	13	
optic_tract	2.00E-2	2.08E-2	1.75E-10	7E-12	1.35E-10	6E-12	1.01E-12	4E-13	1.01E-12	4E-13
pontine_gray	2.44E-2	2.54E-2	2.80E-10	1E-11	2.12E-10	8E-12	1.14E-12	2E-13	8.27E-13	2E-13
spinal_trigeminal_tract	2.78E-2	2.89E-2	2.64E-10	7E-12	2.01E-10	6E-12	1.49E-12	2E-13	1.32E-12	2E-13
substantia_nigra	3.54E-2	3.68E-2	8.98E-11	4E-12	6.85E-11	4E-12	7.70E-13	1E-13	7.56E-13	1E-13
superior_colliculus	1.27E-1	1.32E-1	6.58E-11	2E-12	5.02E-11	2E-12	1.09E-12	1E-13	1.04E-12	1E-13
pineal_gland	3.00E-3	3.12E-3	2.34E-10	2E-11	1.70E-10	2E-11				
ventral_thalamic_nuclei	5.75E-2	5.98E-2	2.44E-11	1E-12	1.94E-11	1E-12	8.34E-13	1E-13	7.75E-13	1E-13
ventricular_system	9.65E-2	1.00E-1	6.09E-11	2E-12	4.64E-11	2E-12	1.05E-12	1E-13	9.23E-13	1E-13
thyroid	2.62E-1	2.69E-1	1.26E-10	2E-12	9.45E-11	2E-12	2.24E-12	1E-13	1.99E-12	1E-13
Large_Int	8.76E+0	1.06E-2	2.63E-10	2E-12	2.98E-10	2E-12	3.11E-12	4E-13	3.73E-12	4E-13
Small_Int	1.00E+1	1.21E-2	1.79E-10	1E-12	1.78E-10	1E-12	2.73E-12	3E-13	2.95E-12	3E-13
marrow	1.38E+1	1.43E+1	8.03E-10	8E-13	6.49E-10	7E-13	7.13E-12	3E-14	6.75E-12	3E-14
			Free ^{99m}Tc 2h		Free ^{99m}Tc 4h		^{99m}Tc-CHSg 2h		^{99m}Tc-CHSg 4h	
			MEAN	error	MEAN	error	MEAN	error	MEAN	error
Dose at @ 1 cm (mGy/decay)			4.8E-12	1E-13	4.8E-12	1E-13	3.9E-12	1E-13	3.6E-12	1E-13
Energy Dep (MeV)			2.689E-2	2E-5	2.685E-2	2E-5	2.672E-2	2E-5	2.675E-2	2E-5
Avg (mGy/decay)			1.351E-11	1E-14	1.349E-11	1E-14	1.342E-11	1E-14	1.344E-11	1E-14
Max D (mGy/decay)			1.20E-9		1.38E-9		2.77E-9		2.51E-9	
Min D (mGy/decay)			3.21E-		2.91E-		3.55E-		4.67E-	

			13		13		13		13	
	Vol (cm^3)	Mass (g)	Dose per tissue (mGy/decay)							
			MEAN	error	MEAN	error	MEAN	error	MEAN	error
skin	1.79E+1	1.95E+1	2.43E-12	1E-14	2.42E-12	1E-14	2.33E-12	1E-14	2.32E-12	1E-14
myoLV	5.75E-1	6.03E-1	3.61E-11	3E-13	3.96E-11	4E-13	5.44E-11	4E-13	4.99E-11	4E-13
myoRV	8.34E-2	8.75E-2	2.41E-11	7E-13	2.61E-11	7E-13	2.41E-11	6E-13	2.23E-11	6E-13
myoLA	1.53E-2	1.60E-2	2.96E-11	2E-12	3.36E-11	2E-12	4.90E-11	2E-12	4.44E-11	2E-12
myoRA	2.15E-2	2.26E-2	6.63E-11	3E-12	7.50E-11	3E-12	1.38E-10	4E-12	1.27E-10	4E-12
bldplLV	8.49E-1	9.00E-1	2.17E-11	2E-13	2.23E-11	2E-13	3.17E-11	2E-13	2.93E-11	2E-13
bldplRV	7.51E-1	7.96E-1	2.16E-11	2E-13	2.16E-11	2E-13	2.89E-11	2E-13	2.67E-11	2E-13
bldplLA	2.49E-1	2.64E-1	4.55E-11	6E-13	4.97E-11	6E-13	9.06E-11	8E-13	8.29E-11	8E-13
bldplRA	9.81E-1	1.04E+0	3.04E-11	2E-13	3.14E-11	2E-13	4.37E-11	3E-13	4.04E-11	3E-13
Rest of the body	2.27E+2	2.33E+2	4.34E-12	5E-15	4.24E-12	6E-15	4.87E-12	6E-15	4.94E-12	6E-15
Liver	1.04E+1	1.10E+1	1.34E-10	2E-13	1.25E-10	2E-13	1.87E-11	5E-14	1.84E-11	5E-14
Lung	2.88E+0	7.48E-1	1.20E-9	2E-12	1.38E-9	2E-12	2.77E-9	3E-12	2.51E-9	3E-12
Trachea	7.24E-1	7.46E-1	9.10E-11	6E-13	1.04E-10	6E-13	2.04E-10	8E-13	1.85E-10	8E-13
Stomach_Contents	4.65E+0	4.79E+0	1.38E-11	6E-14	1.55E-11	7E-14	7.09E-12	4E-14	6.89E-12	4E-14
Pancreas	5.08E-1	5.28E-1	1.01E-11	2E-13	1.07E-11	2E-13	4.82E-12	1E-13	5.65E-12	1E-13

Kidney	2.09E+0	2.19E+0	2.16E-11	2E-13	1.69E-11	1E-13	3.21E-11	2E-13	6.71E-11	3E-13
Spleen	8.13E-1	8.62E-1	2.29E-10	9E-13	3.78E-10	1E-12	4.62E-12	1E-13	5.82E-12	1E-13
Small_Intestine	4.23E+0	4.35E+0	5.58E-12	4E-14	5.60E-12	4E-14	2.55E-12	3E-14	3.16E-12	3E-14
Large_Intestine	1.95E+0	2.01E+0	4.57E-12	5E-14	3.47E-12	5E-14	2.73E-12	4E-14	4.04E-12	5E-14
Bladder	6.30E-1	6.49E-1	2.57E-10	1E-12	2.76E-11	4E-13	2.08E-10	1E-12	4.21E-10	1E-12
Vas_deferens	5.46E-2	5.63E-2	9.06E-13	1E-13	5.07E-13	9E-14	7.15E-13	1E-13	1.07E-12	1E-13
Testes	1.64E-1	1.70E-1	9.09E-13	8E-14	4.16E-13	6E-14	7.10E-13	7E-14	1.06E-12	9E-14
Wet_Rib_Bone	9.38E-1	1.32E+0	2.90E-11	2E-13	3.06E-11	2E-13	4.07E-11	2E-13	3.75E-11	2E-13
Wet_Spine_Bone	4.14E+0	5.88E+0	7.04E-12	5E-14	7.32E-12	5E-14	1.05E-11	5E-14	1.00E-11	5E-14
Skull	1.24E+0	1.99E+0	6.56E-13	3E-14	6.26E-13	2E-14	8.87E-13	3E-14	8.19E-13	3E-14
humerus	2.42E-1	3.53E-1	5.27E-12	2E-13	5.63E-12	2E-13	8.49E-12	2E-13	7.90E-12	2E-13
radius	1.87E-1	2.73E-1	1.04E-11	3E-13	1.11E-11	3E-13	1.53E-11	3E-13	1.41E-11	3E-13
ulna	2.09E-1	3.06E-1	8.10E-12	2E-13	8.54E-12	2E-13	1.10E-11	2E-13	9.96E-12	2E-13
femur	4.44E-1	5.91E-1	1.23E-12	6E-14	5.98E-13	4E-14	9.29E-13	5E-14	1.57E-12	7E-14
fibula	1.41E-1	1.87E-1	3.88E-13	6E-14	3.00E-13	5E-14	3.55E-13	5E-14	4.67E-13	6E-14
tibia	5.17E-1	6.87E-1	5.10E-13	4E-14	3.68E-13	3E-14	3.97E-13	3E-14	5.16E-13	4E-14
patella	3.75E-2	4.99E-2	6.01E-13	1E-13	3.44E-13	9E-14	3.64E-13	9E-14	7.05E-13	1E-13
bone	1.96E+0	2.75E+0	3.07E-	4E-	2.66E-	4E-	3.29E-	4E-	3.56E-	5E-14

			12	14	12	14	12	14	12	
brain_(backgrnd)	6.00E-2	6.24E-2	6.04E-13	1E-13	6.12E-13	1E-13	7.79E-13	1E-13	7.87E-13	1E-13
cerebral_cortex	1.58E+0	1.64E+0	5.17E-13	2E-14	5.16E-13	2E-14	7.21E-13	2E-14	6.72E-13	2E-14
cerebellum	5.41E-1	5.62E-1	1.03E-12	5E-14	1.04E-12	5E-14	1.46E-12	6E-14	1.40E-12	6E-14
corpus_callosum	1.20E-1	1.24E-1	6.25E-13	8E-14	6.68E-13	8E-14	8.39E-13	9E-14	7.75E-13	8E-14
brainstem	6.33E-1	6.59E-1	9.46E-13	4E-14	9.52E-13	4E-14	1.37E-12	5E-14	1.28E-12	5E-14
striatum	2.46E-1	2.56E-1	5.54E-13	5E-14	5.85E-13	5E-14	7.17E-13	6E-14	6.24E-13	5E-14
thal	1.09E-1	1.13E-1	6.42E-13	8E-14	6.28E-13	8E-14	8.87E-13	1E-13	7.88E-13	1E-13
hippo	3.01E-1	3.13E-1	6.02E-13	5E-14	5.97E-13	5E-14	8.77E-13	6E-14	8.39E-13	6E-14
hypothalamus	9.40E-2	9.78E-2	6.75E-13	9E-14	7.17E-13	9E-14	8.16E-13	1E-13	8.28E-13	1E-13
amygdala	1.48E-1	1.54E-1	5.59E-13	6E-14	6.09E-13	7E-14	9.05E-13	9E-14	8.43E-13	9E-14
lateral_septal_nuclei	4.69E-2	4.88E-2	5.20E-13	1E-13	4.88E-13	1E-13	6.15E-13	1E-13	5.99E-13	1E-13
anterior_commissure	1.19E-2	1.24E-2	4.72E-13	2E-13	5.29E-13	2E-13	5.82E-13	2E-13	5.41E-13	2E-13
anterior_pretectal_nucleus	1.36E-2	1.42E-2	3.21E-13	2E-13	4.02E-13	2E-13	6.88E-13	2E-13	5.06E-13	2E-13
periaqueductal_gray	3.66E-2	3.81E-2	8.21E-13	2E-13	8.85E-13	2E-13	8.87E-13	2E-13	8.09E-13	2E-13
aqueduct	4.38E-3	4.55E-3	5.60E-13	3E-13	6.33E-13	3E-13	6.40E-13	4E-13	6.40E-13	4E-13
cerebral_peduncle	1.86E-2	1.94E-2	4.40E-13	1E-13	4.85E-13	1E-13	6.95E-13	2E-13	6.95E-13	2E-13
cochlear_nuclei	2.23E-2	2.31E-2	1.29E-12	3E-13	1.14E-12	3E-13	1.43E-12	3E-13	1.36E-12	3E-13

deep_mesencephalic_nuclei	4.38E-2	4.55E-2	8.15E-13	1E-13	8.55E-13	2E-13	1.35E-12	2E-13	1.32E-12	2E-13
fimbria	2.21E-2	2.30E-2	7.38E-13	2E-13	8.62E-13	2E-13	1.05E-12	2E-13	9.20E-13	2E-13
fornix	1.56E-2	1.63E-2	3.95E-13	1E-13	4.18E-13	2E-13	8.37E-13	2E-13	8.37E-13	2E-13
globus_pallidus	2.70E-2	2.81E-2	6.57E-13	1E-13	6.89E-13	2E-13	8.32E-13	2E-13	8.31E-13	2E-13
inferior_colliculus	6.51E-2	6.77E-2	8.76E-13	1E-13	9.21E-13	1E-13	1.29E-12	2E-13	1.15E-12	2E-13
internal_capsule	4.13E-2	4.29E-2	7.69E-13	1E-13	6.81E-13	1E-13	8.78E-13	2E-13	9.08E-13	2E-13
interpeduncular_nucleus	4.75E-3	4.94E-3	7.42E-13	4E-13	8.25E-13	4E-13	1.37E-12	5E-13	1.29E-12	5E-13
lateral_dorsal_nucleus_of_thalamus	1.18E-2	1.22E-2	3.25E-13	1E-13	2.91E-13	1E-13	8.33E-13	3E-13	6.91E-13	2E-13
lateral_geniculate	1.86E-2	1.94E-2	9.39E-13	3E-13	1.06E-12	3E-13	8.97E-13	2E-13	8.65E-13	2E-13
lateral_lemniscus	1.68E-2	1.74E-2	8.07E-13	2E-13	9.01E-13	2E-13	1.50E-12	3E-13	1.50E-12	3E-13
medial_geniculate	1.80E-2	1.87E-2	1.05E-12	3E-13	1.04E-12	3E-13	1.23E-12	3E-13	1.34E-12	3E-13
nucleus_accumbens	5.94E-2	6.18E-2	5.62E-13	1E-13	5.90E-13	1E-13	7.49E-13	1E-13	7.56E-13	1E-13
olfactory_areas	3.33E-1	3.46E-1	4.56E-13	4E-14	4.28E-13	4E-14	5.90E-13	5E-14	5.81E-13	5E-14
optic_tract	2.00E-2	2.08E-2	8.02E-13	3E-13	8.73E-13	3E-13	1.07E-12	4E-13	1.01E-12	4E-13
pontine_gray	2.44E-2	2.54E-2	8.21E-13	2E-13	8.54E-13	2E-13	1.28E-12	2E-13	1.05E-12	2E-13
spinal_trigeminal_tract	2.78E-2	2.89E-2	1.09E-12	2E-13	1.04E-12	2E-13	1.53E-12	2E-13	1.40E-12	2E-13
substantia_nigra	3.54E-2	3.68E-2	5.79E-13	1E-13	5.22E-13	1E-13	8.14E-13	2E-13	7.25E-13	1E-13
superior_colliculus	1.27E-1	1.32E-1	7.56E-	9E-	7.96E-	9E-	1.14E-	1E-	1.08E-	1E-13

			13	14	13	14	12	13	12	
pineal_gland	3.00E-3	3.12E-3					5.48E-13	5E-13		
ventral_thalamic_nuclei	5.75E-2	5.98E-2	7.15E-13	1E-13	7.35E-13	1E-13	8.86E-13	1E-13	7.86E-13	1E-13
ventricular_system	9.65E-2	1.00E-1	5.76E-13	9E-14	6.60E-13	1E-13	1.08E-12	1E-13	9.84E-13	1E-13
thyroid	2.62E-1	2.69E-1	1.49E-12	8E-14	1.58E-12	8E-14	2.31E-12	1E-13	2.15E-12	1E-13
Large_Int	8.76E+0	1.06E-2	3.61E-12	4E-13	2.49E-12	3E-13	2.54E-12	4E-13	3.60E-12	4E-13
Small_Int	1.00E+1	1.21E-2	5.08E-12	4E-13	5.32E-12	4E-13	2.63E-12	3E-13	3.02E-12	3E-13
marrow	1.38E+1	1.43E+1	5.43E-12	2E-14	5.34E-12	2E-14	7.30E-12	3E-14	6.93E-12	3E-14
			^{99m}Tc-PGCD 2h		^{99m}Tc-PGCD 4h		^{68}Ga-CHSg 2h		^{68}Ga-PGCD 2h	
			MEAN	error	MEAN	error	MEAN	error	MEAN	error
Dose at @ 1 cm (mGy/decay)			2.8E-12	1E-13	3.0E-12	1E-13	5.4E-11	1E-12	4.9E-11	1E-12
Energy Dep (MeV)			2.672E-2	2E-5	2.684E-2	2E-5	8.022E-1	2E-4	8.018E-1	2E-4
Avg (mGy/decay)			1.342E-11	1E-14	1.349E-11	1E-14	4.030E-10	1E-13	4.028E-10	1E-13
Max D (mGy/decay)			1.70E-9		1.35E-9		1.39E-8		4.48E-8	
Min D (mGy/decay)			3.76E-13		4.53E-13		1.41E-11		1.23E-11	

	Vol (cm^3)	Mass (g)	Dose per tissue (mGy/decay)							
			MEAN	error	MEAN	error	MEAN	error	MEAN	error
skin	1.79E+1	1.95E+1	2.39E-12	1E-14	2.41E-12	1E-14	8.08E-11	1E-13	8.35E-11	2E-13
myoLV	5.75E-1	6.03E-1	3.89E-11	4E-13	2.94E-11	3E-13	3.51E-9	8E-12	2.03E-9	6E-12
myoRV	8.34E-2	8.75E-2	2.11E-	6E-	2.02E-	7E-	1.74E-9	9E-	1.42E-9	8E-12

			11	13	11	13		12		
myoLA	1.53E-2	1.60E-2	3.50E-11	2E-12	2.53E-11	2E-12	2.92E-9	2E-11	1.72E-9	2E-11
myoRA	2.15E-2	2.26E-2	9.04E-11	3E-12	5.74E-11	2E-12	4.93E-9	3E-11	1.99E-9	2E-11
bldplLV	8.49E-1	9.00E-1	2.84E-11	3E-13	2.35E-11	2E-13	2.26E-9	5E-12	1.74E-9	5E-12
bldplRV	7.51E-1	7.96E-1	2.67E-11	3E-13	2.25E-11	2E-13	2.27E-9	6E-12	2.02E-9	6E-12
bldplLA	2.49E-1	2.64E-1	6.40E-11	7E-13	4.18E-11	6E-13	4.72E-9	1E-11	2.17E-9	9E-12
bldplRA	9.81E-1	1.04E+0	3.62E-11	3E-13	2.89E-11	2E-13	3.02E-9	6E-12	1.83E-9	5E-12
Rest of the body	2.27E+2	2.33E+2	5.58E-12	7E-15	5.47E-12	7E-15	2.67E-10	1E-13	2.73E-10	1E-13
Liver	1.04E+1	1.10E+1	1.98E-11	6E-14	6.48E-11	1E-13	1.01E-9	1E-12	6.16E-10	9E-13
Lung	2.88E+0	7.48E-1	1.70E-9	3E-12	9.30E-10	2E-12	1.30E-8	1E-11	2.70E-9	5E-12
Trachea	7.24E-1	7.46E-1	1.26E-10	7E-13	7.10E-11	5E-13	6.33E-9	8E-12	1.43E-9	4E-12
Stomach_Contents	4.65E+0	4.79E+0	6.08E-12	4E-14	7.63E-12	5E-14	1.23E-10	5E-13	9.56E-11	5E-13
Pancreas	5.08E-1	5.28E-1	6.27E-12	1E-13	8.31E-12	1E-13	1.79E-10	2E-12	1.99E-10	2E-12
Kidney	2.09E+0	2.19E+0	7.10E-11	3E-13	9.89E-11	4E-13	6.69E-10	2E-12	9.89E-10	2E-12
Spleen	8.13E-1	8.62E-1	2.87E-11	3E-13	4.15E-11	4E-13	9.04E-10	4E-12	7.79E-10	4E-12
Small_Intestine	4.23E+0	4.35E+0	4.14E-12	4E-14	5.68E-12	4E-14	1.38E-10	5E-13	1.53E-10	6E-13
Large_Intestine	1.95E+0	2.01E+0	7.58E-12	7E-14	9.61E-12	8E-14	3.16E-10	1E-12	7.20E-10	2E-12
Bladder	6.30E-1	6.49E-1	1.14E-9	2E-12	1.35E-9	3E-12	1.39E-8	2E-11	4.48E-8	3E-11

Vas_deferens	5.46E-2	5.63E-2	2.77E-12	2E-13	3.25E-12	3E-13	8.48E-11	3E-12	1.07E-10	3E-12
Testes	1.64E-1	1.70E-1	3.02E-12	2E-13	3.54E-12	2E-13	9.00E-11	2E-12	1.13E-10	2E-12
Wet_Rib_Bone	9.38E-1	1.32E+0	2.79E-11	2E-13	2.07E-11	2E-13	1.51E-9	2E-12	5.96E-10	2E-12
Wet_Spine_Bone	4.14E+0	5.88E+0	8.39E-12	5E-14	6.72E-12	4E-14	3.57E-10	7E-13	2.41E-10	6E-13
Skull	1.24E+0	1.99E+0	1.20E-12	3E-14	1.14E-12	3E-14	2.46E-10	9E-13	2.56E-10	9E-13
humerus	2.42E-1	3.53E-1	6.12E-12	2E-13	4.28E-12	1E-13	2.60E-10	2E-12	2.58E-10	2E-12
radius	1.87E-1	2.73E-1	1.07E-11	3E-13	8.10E-12	2E-13	2.57E-10	2E-12	2.43E-10	2E-12
ulna	2.09E-1	3.06E-1	7.83E-12	2E-13	6.37E-12	2E-13	2.45E-10	2E-12	2.36E-10	2E-12
femur	4.44E-1	5.91E-1	4.11E-12	1E-13	4.76E-12	1E-13	2.72E-10	2E-12	3.01E-10	2E-12
fibula	1.41E-1	1.87E-1	1.41E-12	1E-13	1.57E-12	1E-13	1.98E-10	3E-12	2.14E-10	3E-12
tibia	5.17E-1	6.87E-1	1.38E-12	6E-14	1.58E-12	7E-14	1.82E-10	1E-12	1.95E-10	2E-12
patella	3.75E-2	4.99E-2	2.23E-12	3E-13	2.51E-12	3E-13	2.24E-10	5E-12	2.42E-10	5E-12
bone	1.96E+0	2.75E+0	4.91E-12	5E-14	5.14E-12	5E-14	2.03E-10	7E-13	2.19E-10	7E-13
brain_(backgrnd)	6.00E-2	6.24E-2	1.15E-12	2E-13	1.05E-12	2E-13	2.47E-10	4E-12	2.57E-10	4E-12
cerebral_cortex	1.58E+0	1.64E+0	7.97E-13	3E-14	7.09E-13	2E-14	1.23E-10	9E-13	1.27E-10	1E-12
cerebellum	5.41E-1	5.62E-1	1.24E-12	6E-14	1.02E-12	5E-14	1.02E-10	1E-12	1.03E-10	1E-12
corpus_callosum	1.20E-1	1.24E-1	8.33E-13	9E-14	7.62E-13	9E-14	4.52E-11	1E-12	4.51E-11	1E-12
brainstem	6.33E-1	6.59E-1	1.23E-	5E-	1.03E-	5E-	9.22E-	1E-	9.30E-	1E-12

			12	14	12	14	11	12	11	
striatum	2.46E-1	2.56E-1	6.95E-13	6E-14	5.39E-13	5E-14	3.41E-11	1E-12	3.41E-11	1E-12
thal	1.09E-1	1.13E-1	8.59E-13	1E-13	7.85E-13	1E-13	2.12E-11	1E-12	2.04E-11	1E-12
hippo	3.01E-1	3.13E-1	8.74E-13	6E-14	7.04E-13	5E-14	4.28E-11	1E-12	4.22E-11	1E-12
hypothalamus	9.40E-2	9.78E-2	8.65E-13	1E-13	8.02E-13	1E-13	1.19E-10	4E-12	1.23E-10	4E-12
amygdala	1.48E-1	1.54E-1	8.87E-13	1E-13	8.72E-13	1E-13	1.19E-10	3E-12	1.22E-10	3E-12
lateral_septal_nuclei	4.69E-2	4.88E-2	5.52E-13	1E-13	4.53E-13	1E-13	2.45E-11	2E-12	2.37E-11	2E-12
anterior_commissure	1.19E-2	1.24E-2	4.89E-13	2E-13	5.86E-13	2E-13	3.55E-11	3E-12	3.44E-11	3E-12
anterior_pretectal_nucleus	1.36E-2	1.42E-2	8.20E-13	2E-13	5.71E-13	2E-13	1.59E-11	2E-12	1.41E-11	2E-12
periaqueductal_gray	3.66E-2	3.81E-2	1.01E-12	2E-13	9.09E-13	2E-13	1.94E-11	1E-12	1.65E-11	1E-12
aqueduct	4.38E-3	4.55E-3	3.76E-13	3E-13	5.16E-13	3E-13	2.81E-11	5E-12	2.63E-11	5E-12
cerebral_peduncle	1.86E-2	1.94E-2	8.45E-13	2E-13	6.50E-13	2E-13	7.62E-11	4E-12	7.60E-11	4E-12
cochlear_nuclei	2.23E-2	2.31E-2	1.53E-12	3E-13	1.28E-12	2E-13	1.31E-10	6E-12	1.35E-10	6E-12
deep_mesencephalic_nuclei	4.38E-2	4.55E-2	1.20E-12	2E-13	8.23E-13	1E-13	2.00E-11	1E-12	1.74E-11	1E-12
fimbria	2.21E-2	2.30E-2	6.58E-13	2E-13	4.78E-13	2E-13	1.50E-11	1E-12	1.43E-11	1E-12
fornix	1.56E-2	1.63E-2	8.34E-13	2E-13	6.62E-13	2E-13	5.24E-11	4E-12	5.19E-11	4E-12
globus_pallidus	2.70E-2	2.81E-2	8.82E-13	2E-13	7.86E-13	2E-13	3.00E-11	2E-12	2.85E-11	2E-12
inferior_colliculus	6.51E-2	6.77E-2	1.09E-12	1E-13	9.08E-13	1E-13	6.48E-11	3E-12	6.59E-11	3E-12

internal_capsule	4.13E-2	4.29E-2	8.29E-13	1E-13	6.86E-13	1E-13	2.21E-11	1E-12	2.18E-11	2E-12
interpeduncular_nucleus	4.75E-3	4.94E-3	7.32E-13	4E-13	9.52E-13	5E-13	5.82E-11	8E-12	5.82E-11	8E-12
lateral_dorsal_nucleus_of_thalamus	1.18E-2	1.22E-2	5.44E-13	2E-13	4.73E-13	2E-13	1.41E-11	2E-12	1.23E-11	2E-12
lateral_geniculate	1.86E-2	1.94E-2	9.29E-13	2E-13	9.37E-13	2E-13	1.78E-11	2E-12	1.62E-11	2E-12
lateral_lemniscus	1.68E-2	1.74E-2	1.26E-12	3E-13	9.79E-13	3E-13	2.81E-11	3E-12	2.86E-11	3E-12
medial_geniculate	1.80E-2	1.87E-2	9.90E-13	3E-13	6.40E-13	2E-13	1.67E-11	2E-12	1.59E-11	2E-12
nucleus_accumbens	5.94E-2	6.18E-2	7.59E-13	1E-13	6.40E-13	1E-13	7.49E-11	3E-12	7.60E-11	3E-12
olfactory_areas	3.33E-1	3.46E-1	8.09E-13	6E-14	7.02E-13	6E-14	1.72E-10	2E-12	1.79E-10	3E-12
optic_tract	2.00E-2	2.08E-2	8.10E-13	3E-13	5.59E-13	3E-13	9.99E-11	5E-12	1.03E-10	5E-12
pontine_gray	2.44E-2	2.54E-2	9.69E-13	2E-13	6.67E-13	2E-13	1.63E-10	7E-12	1.66E-10	7E-12
spinal_trigeminal_tract	2.78E-2	2.89E-2	1.51E-12	3E-13	1.07E-12	2E-13	1.50E-10	6E-12	1.55E-10	6E-12
substantia_nigra	3.54E-2	3.68E-2	7.80E-13	2E-13	6.11E-13	1E-13	5.36E-11	3E-12	5.30E-11	3E-12
superior_colliculus	1.27E-1	1.32E-1	1.05E-12	1E-13	9.06E-13	1E-13	4.01E-11	2E-12	3.95E-11	2E-12
pineal_gland	3.00E-3	3.12E-3			4.54E-13	5E-13	1.27E-10	2E-11	1.29E-10	2E-11
ventral_thalamic_nuclei	5.75E-2	5.98E-2	5.68E-13	1E-13	5.00E-13	9E-14	1.65E-11	1E-12	1.52E-11	1E-12
ventricular_system	9.65E-2	1.00E-1	8.14E-13	1E-13	6.65E-13	8E-14	3.71E-11	1E-12	3.61E-11	1E-12
thyroid	2.62E-1	2.69E-1	1.74E-12	9E-14	1.36E-12	8E-14	7.42E-11	2E-12	7.36E-11	2E-12
Large_Int	8.76E+0	1.06E-2	6.86E-	5E-	8.30E-	6E-	2.27E-	2E-	4.45E-	2E-12

			12	13	12	13	10	12	10	
Small_Int	1.00E+1	1.21E-2	3.62E-12	3E-13	4.64E-12	4E-13	1.35E-10	1E-12	1.47E-10	1E-12
marrow	1.38E+1	1.43E+1	7.90E-12	3E-14	7.06E-12	3E-14	6.26E-10	6E-13	5.00E-10	6E-13

			CHS-DOTA-^{90}Y 24h		RMTEX-^{90}Y 24h		Free ^{90}Y 24h	
			MEAN	error	MEAN	error	MEAN	error
Dose at @ 1 cm (mGy/decay)			2.70E-12	2E-13	1.62E-11	6E-13	6.1E-11	1E-12
Energy Dep (MeV)			9.315E-1	2E-4	9.275E-1	2E-4	9.139E-1	2E-4
Avg (mGy/decay)			4.680E-10	1E-13	4.660E-10	1E-13	4.591E-10	1E-13
Max D (mGy/decay)			4.22E-8		3.28E-8		5.44E-9	
Min D (mGy/decay)			1.26E-14		9.49E-13		2.47E-12	
	Vol (cm^3)	Mass (g)						
			MEAN	error	MEAN	error	MEAN	error
skin	1.79E+1	1.95E+1	1.09E-12	2E-14	1.62E-11	6E-14	6.87E-11	1E-13
myoLV	5.75E-1	6.03E-1	7.03E-9	1E-11	5.55E-9	1E-11	8.20E-10	4E-12
myoRV	8.34E-2	8.75E-2	1.57E-9	8E-12	1.34E-9	8E-12	6.49E-10	5E-12
myoLA	1.53E-2	1.60E-2	5.84E-9	3E-11	4.56E-9	3E-11	3.39E-10	8E-12
myoRA	2.15E-2	2.26E-2	1.32E-8	4E-11	1.02E-8	4E-11	4.44E-10	7E-12
bldplLV	8.49E-1	9.00E-1	2.84E-9	6E-12	2.29E-9	5E-12	5.09E-10	2E-12
bldplRV	7.51E-1	7.96E-1	1.47E-9	4E-12	1.21E-9	4E-12	3.48E-10	2E-12

bldplLA	2.49E-1	2.64E-1	1.16E-8	2E-11	9.03E-9	2E-11	4.23E-10	4E-12
bldplRA	9.81E-1	1.04E+0	5.75E-9	8E-12	4.55E-9	7E-12	4.72E-10	2E-12
Rest of the body	2.27E+2	2.33E+2	2.18E-10	9E-14	2.12E-10	8E-14	1.94E-10	1E-13
Liver	1.04E+1	1.10E+1	1.24E-9	1E-12	1.38E-9	1E-12	1.63E-9	1E-12
Lung	2.88E+0	7.48E-1	4.22E-8	1E-11	3.28E-8	1E-11	1.16E-9	3E-12
Trachea	7.24E-1	7.46E-1	2.03E-8	1E-11	1.58E-8	1E-11	7.46E-10	3E-12
Stomach_Contents	4.65E+0	4.79E+0	6.07E-11	4E-13	8.02E-11	5E-13	1.26E-10	6E-13
Pancreas	5.08E-1	5.28E-1	8.41E-12	4E-13	1.46E-10	2E-12	5.39E-10	3E-12
Kidney	2.09E+0	2.19E+0	7.25E-11	6E-13	1.47E-9	3E-12	5.44E-9	5E-12
Spleen	8.13E-1	8.62E-1	2.83E-11	7E-13	2.06E-10	2E-12	6.19E-10	3E-12
Small_Intestine	4.23E+0	4.35E+0	3.47E-12	8E-14	5.72E-11	3E-13	2.10E-10	7E-13
Large_Intestine	1.95E+0	2.01E+0	2.28E-11	3E-13	7.11E-11	5E-13	2.53E-10	9E-13
Bladder	6.30E-1	6.49E-1	1.36E-9	5E-12	1.22E-9	5E-12	3.74E-9	9E-12
Vas_deferens	5.46E-2	5.63E-2	3.15E-13	2E-13	9.49E-13	3E-13	2.47E-12	6E-13
Testes	1.64E-1	1.70E-1	2.91E-13	1E-13	1.35E-12	3E-13	4.60E-12	5E-13
Wet_Rib_Bone	9.38E-1	1.32E+0	4.26E-9	3E-12	3.47E-9	3E-12	8.13E-10	2E-12
Wet_Spine_Bone	4.14E+0	5.88E+0	6.19E-10	9E-13	6.83E-10	1E-12	9.28E-10	9E-13
Skull	1.24E+0	1.99E+0	7.95E-12	2E-13	3.51E-10	1E-12	1.55E-9	2E-12
humerus	2.42E-1	3.53E-1	1.37E-11	5E-13	2.94E-10	2E-12	1.28E-9	4E-12

radius	1.87E-1	2.73E-1	4.62E-11	9E-13	2.89E-10	2E-12	1.16E-9	5E-12
ulna	2.09E-1	3.06E-1	1.72E-11	5E-13	2.80E-10	2E-12	1.21E-9	5E-12
femur	4.44E-1	5.91E-1	7.56E-12	3E-13	3.43E-10	2E-12	1.52E-9	4E-12
fibula	1.41E-1	1.87E-1	3.82E-12	3E-13	1.74E-10	2E-12	7.62E-10	5E-12
tibia	5.17E-1	6.87E-1	4.74E-12	2E-13	2.11E-10	1E-12	9.31E-10	3E-12
patella	3.75E-2	4.99E-2	5.29E-12	6E-13	3.23E-10	5E-12	1.41E-9	1E-11
bone	1.96E+0	2.75E+0	1.63E-11	2E-13	2.00E-10	6E-13	8.44E-10	1E-12
brain_(backgrnd)	6.00E-2	6.24E-2	8.73E-12	6E-13	4.22E-10	5E-12	1.86E-9	1E-11
cerebral_cortex	1.58E+0	1.64E+0	4.25E-12	2E-13	2.06E-10	1E-12	9.03E-10	3E-12
cerebellum	5.41E-1	5.62E-1	3.23E-12	3E-13	1.43E-10	2E-12	6.30E-10	4E-12
corpus_callosum	1.20E-1	1.24E-1	1.46E-12	2E-13	7.09E-11	2E-12	3.16E-10	3E-12
brainstem	6.33E-1	6.59E-1	3.20E-12	2E-13	1.45E-10	2E-12	6.37E-10	4E-12
striatum	2.46E-1	2.56E-1	1.05E-12	2E-13	5.71E-11	1E-12	2.55E-10	3E-12
thal	1.09E-1	1.13E-1	6.78E-13	2E-13	1.85E-11	1E-12	8.61E-11	2E-12
hippo	3.01E-1	3.13E-1	1.69E-12	2E-13	7.11E-11	2E-12	3.17E-10	3E-12
hypothalamus	9.40E-2	9.78E-2	4.57E-12	7E-13	2.04E-10	5E-12	9.25E-10	1E-11
amygdala	1.48E-1	1.54E-1	4.75E-12	6E-13	2.06E-10	4E-12	9.30E-10	8E-12
lateral_septal_nuclei	4.69E-2	4.88E-2	5.30E-	3E-13	2.69E-	2E-12	1.35E-	5E-12

			13		11		10	
anterior_commissure	1.19E-2	1.24E-2	9.33E-13	5E-13	5.49E-11	4E-12	2.65E-10	1E-11
anterior_pretectal_nucleus	1.36E-2	1.42E-2	3.18E-13	3E-13	7.24E-12	2E-12	4.42E-11	4E-12
periaqueductal_gray	3.66E-2	3.81E-2	1.26E-14	7E-15	1.57E-11	2E-12	6.20E-11	3E-12
aqueduct	4.38E-3	4.55E-3			2.23E-11	5E-12	1.09E-10	1E-11
cerebral_peduncle	1.86E-2	1.94E-2	2.73E-12	8E-13	1.18E-10	5E-12	5.54E-10	1E-11
cochlear_nuclei	2.23E-2	2.31E-2	5.61E-12	1E-12	2.10E-10	7E-12	9.78E-10	2E-11
deep_mesencephalic_nuclei	4.38E-2	4.55E-2	2.55E-14	2E-14	1.59E-11	2E-12	7.80E-11	4E-12
fimbria	2.21E-2	2.30E-2	3.50E-13	2E-13	1.15E-11	1E-12	5.65E-11	3E-12
fornix	1.56E-2	1.63E-2	1.29E-12	5E-13	8.08E-11	4E-12	3.76E-10	1E-11
globus_pallidus	2.70E-2	2.81E-2	4.69E-13	2E-13	4.95E-11	3E-12	2.11E-10	7E-12
inferior_colliculus	6.51E-2	6.77E-2	1.64E-12	5E-13	1.15E-10	4E-12	4.91E-10	8E-12
internal_capsule	4.13E-2	4.29E-2	9.05E-13	4E-13	2.48E-11	2E-12	1.12E-10	4E-12
interpeduncular_nucleus	4.75E-3	4.94E-3	6.22E-13	6E-13	9.82E-11	1E-11	4.47E-10	2E-11
lateral_dorsal_nucleus_of_thalamus	1.18E-2	1.22E-2			5.21E-12	2E-12	2.73E-11	4E-12
lateral_geniculate	1.86E-2	1.94E-2	1.92E-12	8E-13	1.92E-11	2E-12	8.62E-11	5E-12
lateral_lemniscus	1.68E-2	1.74E-2	1.38E-12	6E-13	5.24E-11	4E-12	2.30E-10	9E-12
medial_geniculate	1.80E-2	1.87E-2	3.22E-13	2E-13	1.88E-11	3E-12	7.83E-11	5E-12

nucleus_accumbens	5.94E-2	6.18E-2	1.93E-12	5E-13	1.45E-10	4E-12	6.43E-10	9E-12
olfactory_areas	3.33E-1	3.46E-1	7.78E-12	5E-13	3.51E-10	4E-12	1.56E-9	8E-12
optic_tract	2.00E-2	2.08E-2	6.34E-12	1E-12	1.72E-10	7E-12	7.62E-10	1E-11
pontine_gray	2.44E-2	2.54E-2	4.40E-12	1E-12	2.77E-10	9E-12	1.24E-9	2E-11
spinal_trigeminal_tract	2.78E-2	2.89E-2	5.87E-12	1E-12	2.43E-10	7E-12	1.07E-9	1E-11
substantia_nigra	3.54E-2	3.68E-2	1.69E-12	6E-13	8.54E-11	4E-12	3.85E-10	9E-12
superior_colliculus	1.27E-1	1.32E-1	8.51E-13	2E-13	6.13E-11	2E-12	2.71E-10	5E-12
pineal_gland	3.00E-3	3.12E-3	6.19E-12	3E-12	2.31E-10	2E-11	9.58E-10	4E-11
ventral_thalamic_nuclei	5.75E-2	5.98E-2	8.26E-13	4E-13	1.22E-11	1E-12	5.38E-11	3E-12
ventricular_system	9.65E-2	1.00E-1	1.25E-12	2E-13	4.85E-11	2E-12	2.13E-10	3E-12
thyroid	2.62E-1	2.69E-1	3.41E-13	1E-13	1.17E-11	7E-13	4.99E-11	1E-12
Large_Int	8.76E+0	1.06E-2	1.32E-11	3E-13	4.85E-11	6E-13	1.77E-10	1E-12
Small_Int	1.00E+1	1.21E-2	3.63E-12	2E-13	5.56E-11	6E-13	2.05E-10	1E-12
marrow	1.38E+1	1.43E+1	6.83E-10	5E-13	1.19E-9	8E-13	3.01E-9	1E-12

VITA

Alejandro Amor Coarasa

Born, Havana, Cuba

2005	Radiochemistry Diploma (summa cum laude) Institute of Applied Science and Technology (InSTEC). Havana, Cuba.
2007	Master in Radiochemistry Institute of Applied Science and Technology (InSTEC). Havana, Cuba.
2005-2008	Associate Professor in the Radiochemistry Department, Institute of Applied Science and Technology, Havana, Cuba.
2008-2009	Research Lab Assistant, Nuclear Oncology Laboratories, FIU, Biomedical Engineering,.
2009	Adjunct Faculty, Chemistry Physics and Earth Science Department, Miami Dade College, Kendall Campus.
2009-Present	Doctoral Candidate, Teacher Assistant and Research Assistant, Florida International University, Biomedical Engineering Department.
2010-Present	Faculty Appointment at the Herbert Wertheim College of Medicine, Radiology Department, Florida International University, Miami, FL.
2008-Present	Radiochemistry, Radiopharmacy and Dosimetry Consultant Jackson North Medical Center/Herbert Wertheim College of Medicine for Clinical trials using ^{68}Ga, ^{124}I and ^{18}F, PET and investigational new drug applications.

PUBLICATIONS AND PRESENTATIONS

Several Authors, Trace experimental techniques for CFD Model Verification and Validation in sugar cane crystallizer. IAEA TEC-DOC-1412 Integration of tracing with computational fluid for industrial process investigation. Final Report of a coordinated research project 2001-2003. ISBN 92-0-114504-7, ISSN 1011¬4289. IAEA 2004

Amor-Coarasa, A. Xiquez-Castillo, J. Morín-Zorrilla; Positronic radionuclides generator produced. ^{68}Ge/^{68}Ga Generator. ISBN: 959-7136¬33-3, 2006.

Amor-Coarasa, J. Borroto-Portela, J. Griffith-Martínez; Construction of a $^{137}Cs/^{137m}Ba$ Radioisotopic Generador; ISBN: 959-7136-33-3, 2006.

Amor-Coarasa A, Borroto J, Griffith j, "Development of a New Type of $^{137}Cs/^{137m}Ba$ Radioisotope Generator", Tracers and Tracing Methods, Tracer 4, 3-5 octubre 2006, Aetrans/Grenoble France, IAEA, Meeting Report.

Alejandro Amor-Coarasa, Abmel Xiquez-Castillo, José Morín-Zorrilla, "Preliminary work for construction of a $^{68}Ge/^{68}Ga$ radioisotopic generator for medical use in positron emission tomography", CLAQ, Cuban Chemistry Magazine, ISBN: 959-282-27-X

Amor-Coarasa A., Borroto-Portela J., Grifith-Martínez J., "Development of a new type of $^{137}Cs/^{137m}Ba$ radioisotope generador", Nucleus, No. 41, 2007. ISSN 0864-084X, p. 15-19.

Alejandro Amor Coarasa; Riss, Patrick; Kroll, Carsten; Roesch, Frank; Comparative study of ^{68}Ga-NOTA-radiolabelling in water, citrate and HEPES-buffer as reaction media, Jahresbericht, August 2007, p:b-13, ISSN 0932-7622.

Riss, Patrick, Amor-Coarasa, Alejandro; Kroll, Carsten; Roesch, Frank; Radiolabelling of a novel NODAPA-tyrosine derivative; Jahresbericht, August 2007, p:b-16, ISSN 0932-7622.

Alejandro Amor Coarasa; Seza Gulec; Anthony McGoron; Inexpensive and cGMP capable Ga-68 purification system; J Nucl Med. 2012; 53 (Supplement 1):1742.

Alejandro Amor Coarasa; Romila Manchanda, Anthony McGoron; Seza Gulec; Chitosan microspheres: Therapeutic agent for liver-directed radiomicrosphere therapy; J Nucl Med. 2012; 53 (Supplement 1):1707.

André F. Martins, M. I. M. Prata, S. P. J. Rodriguese, Carlos F. G. C. Geraldes, P. J. Riss, A. Amor-Coarasa, C. Burchardt, C. Kroll and F. Roesch; Spectroscopic, radiochemical, and theoretical studies of the Ga3+-N-2-hydroxyethyl piperazine-N0-2-ethanesulfonic acid (HEPES buffer) system: evidence for the formation of Ga3+- HEPES complexes in ^{68}Ga labeling reactions; Contrast Media Mol. Imaging 2013, 8 265–273.

Alejandro Amor Coarasa, Andrew Milera, Denny A. Carvajal, Anthony McGoron; ^{99m}Tc-MAA vs. ^{68}Ga-MAA as Perfusion Agents: A Pharmacokinetic Approach, Accepted for publication as a 2 page extended abstract in the Engineering in Medicine & Biology Society Proceedings, 2013.

Alejandro Amor Coarasa, Andrew Milera, Denny A. Carvajal, Anthony McGoron; Lyophilized Kit for the Preparation of the PET Perfusion Agent [^{68}Ga]-MAA, Submitted to Molecular Imaging on March 2013.

Alejandro Amor Coarasa, Andrew Milera, Denny A. Carvajal, Anthony McGoron; "In Vivo" Evaluation of Chitosan Glycol-^{99m}Tc and Chitosan Glycol-NOTA-^{68}Ga labeled microspheres as new SPECT and PET perfusion agents , Submitted to Molecular Imaging on May 2013.

Alejandro Amor Coarasa, Andrew Milera, Denny A. Carvajal, Anthony McGoron; Chitosan-DOTA-^{90}Y Microspheres: A New Biodegradable Radiotherapy Agent for Liver Radiomicrosphere Therapy, Submitted to Molecular Imaging on May 2013.